Energy Transfer and Current Transport for Si Nanostructured Photovoltaic Cells

MOHAMMED AHMED ABDELHAMEED AHMED

February 2023

Energy Transfer and Current Transport for Si Nanostructured Photovoltaic Cells

MOHAMMED AHMED ABDELHAMEED AHMED
Doctoral Program in Materials Science and Engineering

Submitted to the Graduate School of
Pure and Applied Sciences
in Partial Fulfillment of the Requirements
for the Degree of Doctor of Philosophy in
Engineering

at the
University of Tsukuba

Abstract

Hybrid organic polymer-silicon solar cells have recently emerged to replace the silicon p-n junction, where an organic polymer semiconductor is deposited on top of silicon at low temperatures with less manufacturing costs. Poly (3,4-ethylene dioxythiophene):poly (styrene sulfonate) (PEDOT:PSS)/Si hybrid heterojunction solar cell has been investigated owing to the high transparency and conductivity of PEDOT:PSS and the appropriate passivation attributes of PEDOT:PSS on the Si surface which reduces interfacial recombination. The output efficiency of this promising hybrid device is boosted by nanostructuring the Si surface in the form of silicon nanowires (SiNWs) which provides an exceptionally wide spectrum of light absorption as well as enhanced carrier collection with a high surface-area-to-volume ratio which helps in the thickness reduction of the silicon substrate and increases the junction area.

The energy conversion efficiency of the hybrid solar cells has been enhanced through the downshifting of highly energetic photons in the ultraviolet region to photons with lower energy by silicon quantum dots (SiQDs). SiQDs deposited on Si substrate absorbs solar light in the UV region and transfer the energy to the Si substrate via the non-radiative energy transfer (NRET) and radiative energy transfer (RET) processes. The NRET effect can be enhanced by minimizing the distance between SiQDs and the solar cell surface. In hybrid heterojunction solar cells, SiQDs were introduced in-between Si nanostructures and PEDOT:PSS. Three different ligands of various lengths were examined in order to elucidate dependency on ligand length. The maximum solar cell efficiency was achieved using 1-octene, which has the shortest ligand length and hence the highest NRET improvement.

Dopant-free vanadium oxide (VO_x) semiconductor thin films were also investigated for their hole-injection workability. Solution-processable VO_x films were annealed at 450 °C in a variety of atmospheres. It was discovered using X-ray diffraction that annealing in oxygen, nitrogen, and vacuum each produced a distinct crystal structure of V_2O_5, VO_2(M), and VO_2(B), respectively. X-ray photoelectron spectroscopy indicated gap states that formed from oxygen deficiencies placed inside the band gap of the annealed VO_x. Because of their high work function, broad band gap, and oxygen deficiencies, these VO_x thin films perform admirably as transparent hole-injection layers. Various ambient annealed VO_x films were utilized in SiNW-based solar cells. The greatest hole-injection performance was seen in the vacuum-annealed film VO_{2-x}(B). Compared to their SiNWs/PEDOT:PSS hybrid device counterpart, SiNWs/VO_x solar cells exhibit markedly greater stability under ambient circumstances.

Pencil-shaped silicon nanowires (SiNPs) were fabricated and utilized in Schottky junction solar cells where it can better be passivated by VO_{2-x} film than SiNWs. The asymmetry of nanopencils is responsible

for their many useful properties, such as their ability to absorb and trap light throughout a wide spectrum. Dark current-voltage (*I*-*V*) curves for an Ag/VO_{2-x}/SiNPs/Ti/Ag Schottky junction device were measured and analyzed across a temperature range from 298 to 358 K. The junction parameters were calculated in terms of the thermionic emission theory at different temperatures from the (*I*-*V*) curves, including the ideality factor (*n*) and the barrier height (φ_b), and found to be 1.73 and 0.78 eV, respectively, at room temperature. In the forward bias regime, we find that thermionic emission dominates at low voltages ($V \leq 0.12$ V), space charge limited current controlled by a single trap state dominates at middle voltages ($0.12 < V < 0.3$ V), and space charge limited current regulated by a distribution of trap levels dominates at high voltages ($V \geq 0.3$ V). The (*C*-*V*) measurements were used to calculate the built-in potential, which was discovered to be 0.62 eV. Unless encapsulation is given, PEDOT:PSS/SiNPs hybrid solar cells rapidly degrade under ambient circumstances, whereas VO_{2-x}/SiNPs solar cells are far more stable.

Acknowledgement

I want to start by expressing my gratitude and exaltation to my God, "***ALLAH***," for educating and supporting me throughout my entire life.

My advisor, *Prof. Naoki Fukata*, deserves special recognition for his support and supervision throughout the duration of this thesis's study, as well as for his role in getting the necessary funding and a good portion of the equipment utilized in the tests. To conduct this study would not have been feasible without this help. Throughout my doctoral studies, he was an invaluable resource, providing me with scientific direction, stimulating conversation, insightful questions, and endless encouragement.

I want to express my gratitude to *Professors Yoshihika Takeda*, *Takahide Yamaguchi*, and *Kaoru Toko* for accepting the examination of my thesis and providing illuminating feedback.

In addition, I am grateful to *Drs. Wipakorn Jevasuwan, Ryo Matsumura,* and *Thiyagu Subramani*, who were instrumental in getting this research off the ground by offering training on the equipment used and insightful suggestions and recommendations.

I also appreciate the assistance and support given from my group fellow researchers, *Drs. Mohamed Esmat*, *Mostafa Abdelbar*, *Yongli Sun*, and *Xiaolong Zhang*.

I would like to convey my thanks to the Ministry of Higher Education of the Arab Republic of Egypt for financing my doctoral studies.

Special appreciation and thanks for my friend, *Dr. Youssef Mohammed*. I will never forget the assistance and motivation I received while pursuing my doctorate in Japan.

My sincere appreciation and loving goes to *Leen* and *Ayah* for their supporting and sacrifices during my study in Japan. Deepest thanks with gratitude to my *parents* and *siblings* in Egypt for providing the encouragement that I needed, to pursue and complete this degree.

Table of Contents

Chapter 1. Introduction

1.1 Changing to Renewable and Clean Energy

Fossil fuels including oil, coal, and gas have been relied upon heavily since the start of the Industrial Revolution in the 19th century. Over the period from 2011 to 2035, worldwide energy consumption per capita is expected to increase by another 30%, as reported by the International Energy Agency (IEA). [1,2] Electricity demand is expected to increase by a factor of four during that time.[3] A forecasted 80% rise in CO_2 emissions is possible if environmentally friendly energy generating options are not established to meet this anticipated increase in energy consumption.[3] According to the Intergovernmental Panel on Climate Change (IPCC) Fifth Assessment Report (2013), the atmospheric concentration of CO_2 has grown to an unprecedented level during the previous 800,000 years, and that human contribution toward this negative impact is quite strong.[4] The report explained that there is a causal link between the concentration of carbon dioxide in the atmosphere and the worldwide average temperature, and it provided a roadmap for stabilizing the global average temperature in the future by lowering CO_2 emissions. There will be a lot of negative consequences as a result of climate change, according to the IPCC's impact, adoption, and vulnerability report.[5] Food shortages, insufficient access to clean water, weather extremes, floods, and the destruction of marine and coastal ecosystems are all serious concerns. Although cutting down on CO_2 emissions is essential, progress has been modest thus far. However, the International Energy Agency (IEA) estimates that the long-term global temperature increase of 3.6 ˚ C is on track, but can increase even further if proper mechanisms are not put in place.[6] This is despite the fact that the international target for global temperature increase is 2˚ C.

One of the possible solutions to the emission of CO_2 and other hazardous gases is renewable energy. First among these is solar power. In contrast to other energy sources, solar power has no cost and may be used indefinitely. Photovoltaics, as the sole technology that converts our basic source of energy, the solar radiation, into electricity, play a significant part in the mix of renewable energy sources needed to meet the rise in energy demand. However, as shown in Figure 1.1[7], the greatest photocurrent that may be achieved by solar-powered photovoltaic (PV) systems is constrained by the overlap between the active layer's absorption spectrum and the solar photon flux. Material choices for solar cells (SCs) should take this into account, since the best active layer components should strive to provide the highest possible photocurrent. Although solar energy is cheap, abundant, and sustainable compared to the commercial energy supply based on fossil fuel, the upfront cost of equipment for gathering this radiant energy through the development of SCs, panels, and modules is prohibitive. On that point, there has been a lot of research done and is currently being done to lower the cost of manufacturing solar devices and increase the power conversion efficiency (PCE) of SCs.

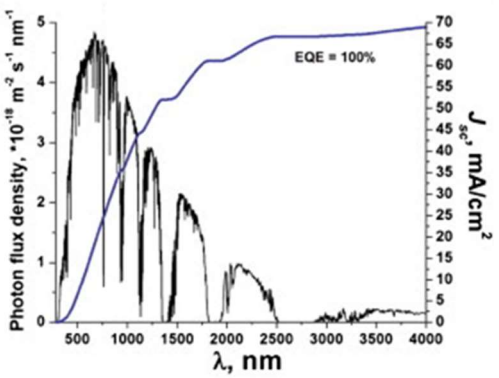

Figure 1.1 Maximum attainable integrated short-circuit current density (J_{sc}) and the total global photon flux from the sun, both with a 100% external quantum efficiency (EQE).

With its widespread use in nations like Europe, China, and the United States, solar energy now only meets less than 10% of the world's electrical needs.[8] Since the year 2000, the number of PVs installed globally has been rising quickly, and the cost of solar modules is continuing to fall, giving solid grounds for optimism that solar power generation will eventually become a significant source of low-carbon energy. By 2050, the IEA anticipated that solar energy will produce 22% of the world's power[3]; however, if low cost and large-scale PVs devices could be adopted as a consequence of new technologies, this proportion may be exceeded. While solar power has been heralded as the answer to the world's energy dilemma, it is not without its drawbacks. (i) The amount of solar radiation received on Earth varies according to latitude and time of day[9]; more energy is received from the sun during the day than at night. (ii) Solar photovoltaic (PV) devices need a lot of sunshine to produce power.[9] (iii) The quantity of radiant energy reaching the surface of the planet is governed by the seasons and weather conditions; for example, less sunlight reaches the earth's surface in the winter since the sun's radiation is weaker at that time of year.[10] Solar energy must be stored somewhere at night, and efficient SCs and modules must be created, to mitigate these drawbacks. While there has been little progress made in solar energy storage as of yet, several initiatives are under way to develop more efficient solar energy storage technologies and batteries.

1.2 The technology of photovoltaics (PV)

Photovoltaic is an electrical device that uses the photovoltaic effect, a chemical and physical phenomena, to directly convert solar radiation into electricity. The device's electrical properties shift in response to light, hence it may be classified as a photoelectric cell. Panels made up of solar cells are able to generate a certain quantity of energy due to their ordered, geometric arrangement.

Depending on the kind of semiconductor utilized, photovoltaic systems may be broken down into one of three categories: modules, modules with concentrators, and concentrators without concentrating

solar collectors. Crystalline Silicon (c-Si) cells were the basis for the first generation of solar panels. Si wafer technologies account for almost 93% of the PV market.[11] These methods rely on an indirect band gap absorber material, which necessitates a substantial layer thickness in order to capture more of the sun's rays. High-efficiency solar cells are also rather costly since they require flawless crystals.

Thin film solar cells, which are part of the second generation of solar cells and are made of inorganic materials, have gained popularity as a workaround for the shortcomings of c-Si technology in the early 2000s. Thinner layers absorb more incident solar radiation because they are made of direct band gap materials with a high optical absorption coefficient. As a result of their adaptability, they are useful in several contexts. These days, there are five main categories of inorganic solar cells distinguished by the absorber material they employ: amorphous silicon (a-Si), cadmium telluride (CdTe), copper indium gallium diselenide (CIGS), copper indium diselenide (CIS), and $Cu_2ZnSnSe_4$ (CZTSe).

Third-generation solar cells rely on organic components like polymers and tiny molecules. Expensive multi-junction solar cells, which have the best performance in the world, fall under this group as well. Because of the high cost of manufacture, its use in commercial settings is restricted. Perovskite solar cells, which are third-generation solar cells, show great promise with efficiencies above 20%. Since they are made of polymers, polymer solar cells can be mass-produced quickly and easily. They may be applied inexpensively to vast areas. Even if there are improvements in efficiency and durability with third-generation solar cells, they are not yet widely used.[12]

1.2.1 Crystalline silicon (c-Si)

Crystalline silicon (c-Si), which comprises materials like monocrystalline silicon (mono c-Si) and polycrystalline silicon (poly c-Si)[10,13], is the commercially dominant PV technology and is used to make first-generation SCs, also known as wafer-based SCs. Poly c-Si SCs are made up of multiple crystals formed by cooling and solidifying molten Si, which is then sliced into thin plates, whereas mono c-Si SCs are built up of very pure single c-Si. Extremely high PCE of 14%-18% [14] is typical of mono c-Si SCs. The high temperature and limited throughput manufacturing procedures used to create high grade Si need expensive purification methods. For this reason, poly c-Si SCs emerged as a viable alternative to mono c-Si SCs. As a result of poly c-Si SCs being easier to produce and fabricate at a lower cost, PCE dropped to 13%-15%.[14] The heavy Si wafer cells that are a hallmark of this PV generation are the result of their thick light-absorbing coatings. High-power applications typically call for larger solar panels, which in turn demand more room for shipping.

1.2.2 Cadmium telluride (CdTe)

In terms of its direct optical band gap (1.45 eV), cadmium telluride (CdTe), a p-type semiconductor. Because of its high absorption coefficient of 5.0×10^5 cm^{-1}, it can absorbs a lot of light without needing a lot of space. Through a process of refining copper, tellurium is produced. If CdTe solar cells were more popular, this would be a major issue because cadmium is more common than tellurium. The efficiency

of CdTe solar cells was officially announced to be 22.1% in 2015. However, due to their use of hazardous materials, CdTe based solar cells come with hefty price tags for both waste management and worker protection.[15]

1.2.3 Copper indium gallium diselenide (CIGS)

Thin film photovoltaic systems can also use copper indium gallium diselenide (CIGS) as an absorber layer because it is a p-type semiconductor. The high absorption coefficient of 10^5 cm^{-1} and direct band gap of 1.7 eV in a CIGS solar cell make it possible to absorb 90% of incident light. This material's electronic conductivity is diminished by its inherent defects.

Copper and indium vacancies provide p-type conductivity, whereas selenium vacancies produce n-type. The most significant defect affecting carrier recombination in at Cu is an antisite defect. The Centre for Solar Energy and Hydrogen Research Baden-Württemberg (ZSW) has certified a record-breaking efficiency of 22.6% for CIGS.[16] Nonetheless, its toxicity raises some issues for its use. Furthermore, the bulk manufacture of CIGS is extremely costly because to the presence of pricey constituent materials like In and Ga.

1.2.4 Organic solar cells (OSCs)

OSCs are photovoltaic cells that convert sunlight into energy by transferring photo-induced charge carriers from an organic substance to an external circuit. Depending on the application, SCs of this sort may employ a bilayer or bulk heterojunction (BHJ) device structure. The device, in any scenario, is made up of electron doner (D) and acceptor (A) materials, and two electrodes (an anode and a cathode electrode). Organic materials are popular because a thin sheet may absorb a lot of light despite the material's high optical absorption co-efficient.[17] Also, the low cost and ease of solution processing of organic molecules allow for the fabrication of large cells, which in turn increases the surface area available for light absorption.[18] Low efficiency and instability caused by exposure to moisture, oxygen, ultraviolet (UV) radiation, and thermal stressors are two of the technology's biggest drawbacks in the PV sector. However, OSCs are still utilized to power portable applications like camping gear, smart wearables, and smartphone chargers, rather than replacing Si SCs.

1.3 Physics of solar cells

1.3.1 Photovoltaic effect

In PV technology, each SC has two layers of semiconducting materials, one each of n-type and p-type semiconductors. P-type semiconductors, which use holes as the primary charge carrier, and n-type semiconductors, which use electrons, produce a p-n junction when brought near together. The uneven distribution of electrons and holes between the two zones is the root cause of the charge carrier movement (Figure 1.2 [19]). The photovoltaic effect describes what happens when light of sufficient

energy strikes a p-n junction, causing electrons attached to atoms in the valence band to be energized to a high energy level and become free to travel. When an electron is excited to a higher energy level, it leaves behind a "hole" in the valence band where it used to be. This hole can also move through the material, allowing for the flow of electrical current. The electric field that created by the p-n junction helps to direct the flow of the electrons and holes in a way that maximizes the generation of electrical power. In 1839, French physicist Edmund Becquerel reported the first instance of the photoelectric effect, which occurs when light strikes a silver-coated platinum electrode submerged in an electrolyte.[20] Einstein indicated that the photovoltaic effect is based on the same concept as the photoelectric effect in his explanation of the former from 1905. The existence of this effect in solids was later established by William Adams and Richard Day. For the first time, a silicon photovoltaic device was created in 1954 at Bell Laboratories.[21] Since then, researchers have used a wide variety of materials and SC technologies to try to boost PVs' PCE from its initial 6% to the theoretically expected 30%.[21]

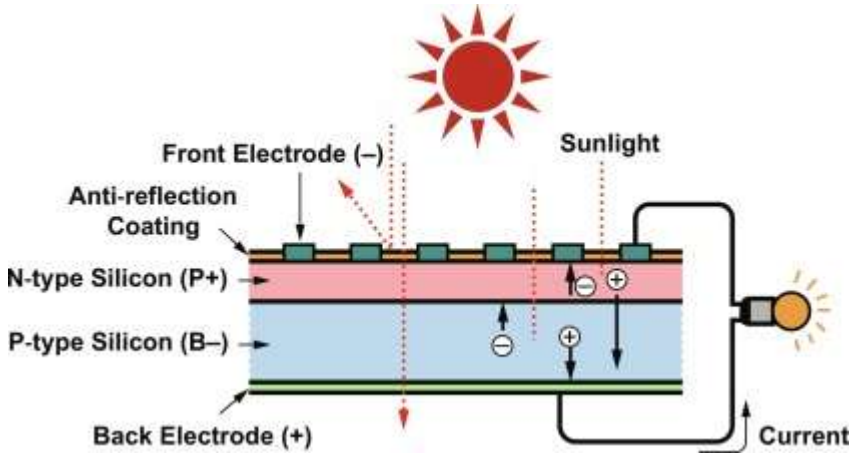

Figure 1.2 Photovoltaic effect.

1.3.2 Fundamental losses and Shockley-Queisser Limit

There is a wide range of wavelengths in the solar energy that reaches Earth, but only a small fraction of them may generate electron-hole pairs. There are a number of variables that can change the absolute minimum efficiency requirement for a particular solar spectrum. When a photon's energy is below the band gap, it is not absorbed, whereas photons with energies beyond the band gap would be absorbed, but the extra energy would be quickly dissipated as heat as the charge carriers thermalized to the band-edges through phonon emission. Reducing the bandgap of a cell will result in decreased absorption losses but will increase thermalization losses, and vice versa. Taking all of this into account, semiconductors with a band gap of 1.1-1.4 eV may retain around 45% of the solar power.[22] The efficiency of solar cells is measured by how much of the solar power they are able to convert into usable electricity.

The highest theoretical efficiency limit, the single most important factor in solar cell manufacture, was initially determined by Shockley and Queisser in 1961. The computation takes into account some

essential factors. They demonstrated that for a single p-n junction with a band gap of 1.34 eV, the greatest solar conversion efficiency can be obtained at roughly 33.7% when employing an AM1.5 sun spectrum.[23] For this reason, materials having a band gap of 1-2 eV (Figure 1.3 [23]) are preferable for generating electricity.

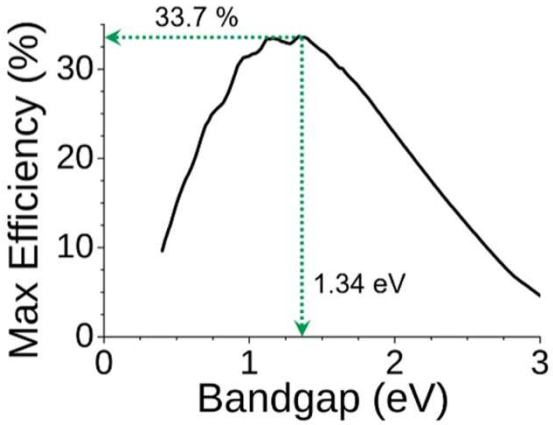

Figure 1.3 The relationship between a single junction device's maximal conversion efficiency and the semiconductor's energy bandgap.

To improve efficiency beyond the Shockley-Queisser limit, researchers are actively exploring a variety of cell architectures that mitigate thermalization and absorption losses in comparison to the single junction design.[24]

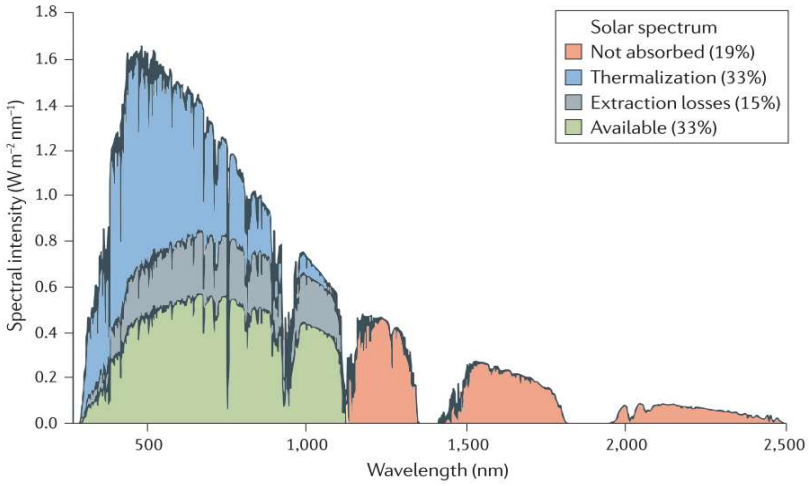

Figure 1.4 The Shockley-Queisser limit's losses in a perfect silicon cell.

Examples of such hypotheses include intermediate band solar cells[25] and upconverter/downconverter techniques.[26] However, extraction losses are inescapable because of the delicate balancing act required to collect carriers at a high electrical potential while also collecting them before they recombine. Figure 1.4[27] shows around 15% of the incident solar energy are lost due to

extraction losses in perfect c-Si solar cells. To overcome this problem, one strategy includes orthogonalizing the orientations of light absorption and charge-carrier collection, where vertically oriented array of high-aspect ratio nanorods might, in theory, offer adequate optical absorption along its axial dimension, while also permitting collection of carriers radially over a distance sufficiently short to compensate for a short minority carrier collecting length.[28]

1.4 Silicon nanowires (SiNWs)

The Silicon nanowire (SiNW) is one example of a Si nanostructure. In at least two dimensions, it is considered nanoscale, while in a third, it extends into macroscopic area. Since its length is still rather large in comparison to other nanoscale structures like nanoparticles, this essentially makes it a nanostructure with distinct attributes compared to bulk Si. The Si industry appreciates this design since the cross section is reduced while the device's thickness is increased by extending it away from the substrate. Multiple devices may be formed from a single nanowire, and numerous nanowires can be found on a Si base substrate. When combined with other substances, SiNW can function as a nanoscale substrate, much as it does in other Si-based technologies.[29]

As previously indicated, SiNWs undergo the same transformation in their bulk material characteristics as they move toward the nanoscale. Despite being made of crystalline Si, SiNWs have a reduced amount of Si atoms throughout the wire, which leads to energy quantization and conductance quantization.[30] Additionally, there are now more surface atoms than internal ones. As a result, its electrical characteristics may be easily modified by altering its surface.[31] The accumulation of charges rapidly within a wire due to charge trapping is another well-known occurrence.[32]

The ability of SiNWs to act as light-trapping structures is a key feature of this thesis. SiNWs can be used as a roughened surface that scatters light and improves its chances of absorption. Large surface-to-volume features produce this form of light dispersion naturally, and it is exploited to boost efficiency in photovoltaics.[33] The process of light trapping in SiNWs is not well understood and is rarely discussed in most papers,[34] although this does not diminish the widespread belief that SiNWs have very high light absorption. Non-oriented, randomly sized SiNWs have been shown to boost absorption uniformly over the visible spectrum.[35] Using SiNWs, this thesis demonstrates that such a structure and light absorption behavior is possible.

There are a variety of techniques for producing SiNWs. Top-down and bottom-up approaches are the two main types of manufacturing processes. By utilizing a catalyst to promote unidirectional growth of the SiNWs, bottom-up approaches are able to build the SiNWs. This includes techniques such as molecular beam epitaxy and laser ablation, as well as vapor-liquid-solid (VLS) development, in which silicon precursor vapors precipitate on a catalyst to produce a solid nanowire (Figure 1.5 (a)). Bottom-

up methods may mass-produce SiNWs on a huge scale, but they frequently yield wires with a disorganized, unpredictable layout, and catalysts can be problematic for VLS. By contrast, SiNW may be fabricated using top-down methods, which include selectively removing layers of a Si substrate until the desired nanowire structures are exposed. Metal catalyzed electroless etching (MCEE) uses catalysts to etch the substrate from below, whereas reactive ion etching (RIE) uses resists and masks to prevent etching from occurring at the substrate's surface. MCEE may also generate complicated rough structures or pits in place of well-defined wire forms (Figure 1.5 (b)[36]), in addition to producing random wires over wide regions. By carefully manipulating the resist or masks, RIE can generate significantly more precise structures (Figure 1.5 (c)[37]). From the substrate, SiNWs can be grown in a variety of orientations, including vertical, horizontal, and angled. In addition to being created on other substrates, they can be removed and transported to other substrates for device applications.

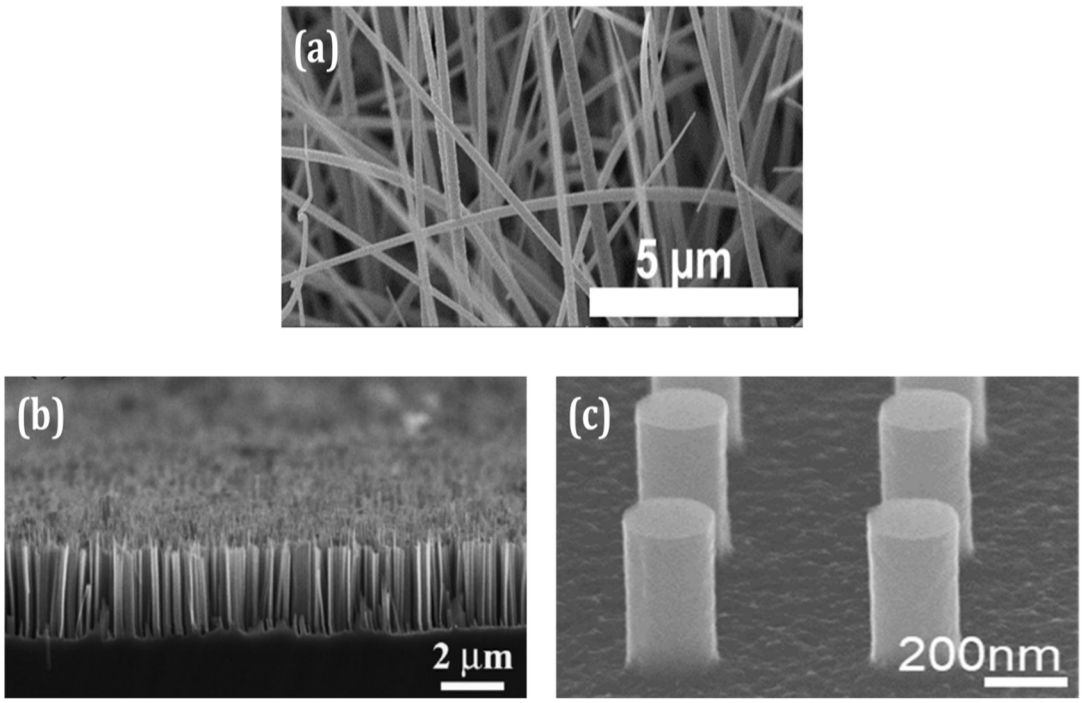

Figure 1.5 SEM image of SiNWs produced by (a) VLS technique, (b) MCEE method, (c) nanoimprint lithography technique.

1.5 Luminescent down-conversion

The main loss factor for all photovoltaic technology is the spectral mismatch between the response of a solar cell and the sun spectrum. High energy photons are absorbed by the semiconducting material, but their excess energy is dissipated as heat due to non-radiative relaxation of the carriers. For an ideal 1.34 eV bandgap, the theoretical maximum photon conversion efficiencies (PCE) efficiency is capped at 33.7% due to these basic losses. Approximately 30% conversion efficiencies are achieved by the best

experimental single junction solar cells when exposed to a single solar irradiation.[38] Advanced front surface optimization of the solar cells is often used to obtain these high experimental efficiencies, since it improves the efficiency with which high energy photons are collected at the surface of the devices. Mass-produced solar modules typically achieve conversion efficiencies of approximately 20%,[39] since such optimization approaches prove in many situations to be prohibitively costly for large-scale industrial manufacturing. Thus, commercial solar cells continue to face significant challenges from the inefficient use of high-energy photons. Solar luminescent down-converting (LDC) is a straightforward method for optimizing the use of high-energy photons. In this technique, a luminous material absorbs unfavorable short-wavelength (high-energy) photons and re-emits them at a more desirable longer-wavelength. LDC materials for various photovoltaic systems have included organic dyes [39] and colloidal quantum dots (QDs).[40] Colloidal QDs are promising candidates for LDC layers because to their high photoluminescence quantum yield,[41] strong absorption and emission tunability, [41] and high absorption cross-section.[41] Spray coating and other low-cost methods make it easy to deposit large-scale LDC films, which do not greatly increase the cost of the finished modules but keep them competitively priced.

1.5.1 Quantum dots (QDs)

These nanocrystals, known as quantum dots (QDs), are quasi-zero-dimensional nanocrystals formed of an inorganic core material and an organic outer layer of capping ligands, and their optical and electrical characteristics depend on their size. The band gap energy, or the difference in energy between the valence band (VB) and the conduction band (CB), is a defining characteristic of colloidal QDs with structures and energies lower than 4 eV. Since the band gap energy moves to higher energy (shorter wavelength) as size decreases, the electrical characteristics are distinct from those of bulk crystals. Solar cells, photocatalysis, biosensing, drug delivery, detection, and bioimaging are only some of the fields that have benefited greatly from developments in the quantum confinement area, which have been enabled by new synthesis methods and size-dependent optical characteristics. When the difference between CB and VB energies is less than the absorption energy, photons are absorbed by the QDs. There is currently a 'hole' in the VB because electrons have been stimulated to the CB. The exciton Bohr radius (α_B) is the average atomic distance between a conduction electron and a valence hole. When an electron is stimulated to the CB level, it quickly drops back across the band gap toward the VB. The energy contained in electromagnetic radiation is dissipated at this period, and the radiated wavelength is in phase with this loss. The band gap energy grows proportionally with the parameters of size, composition, and form of the quantum confinement. This will occur when the size of the QDs is on the order of the exciton Bohr radius, as a result of quantum confinement.[42] Reducing QD size and expanding the band gap are the two main characteristics that determine quantum confinement. Quantum effects provide a sharp cutoff in energy between the highest valence state and the lowest conduction state, and as the size of QDs lowers, the resulting energy band gap has a greater impact on

the characteristics. The size of QDs might change due to two key influences. To begin, the contribution to free energy and changes in thermodynamic characteristics is due to the ratio of surface atoms in QDs. Quantum size effects also have a profound impact on the optical and electrical characteristics of QDs, which vary greatly depending on the size of the particle. QDs' most appealing characteristics are their size-dependent tunability in optical and electrical properties (Figure 1.6 [43])

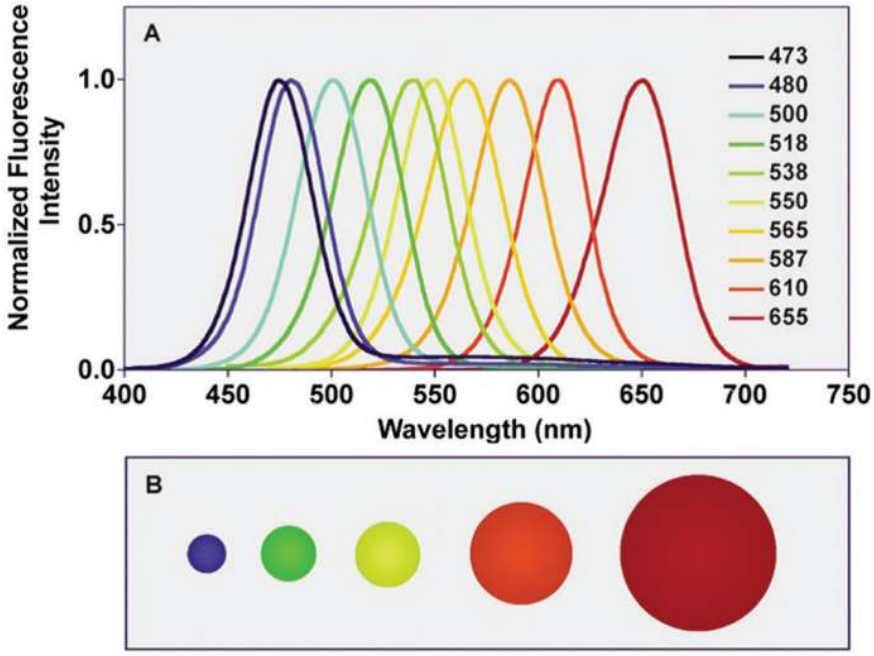

Figure 1.6 (a) Variation in quantum dot fluorescence spectra with size. (b) Sizes of particles ranging from 2.1 nm to 7.5 nm in diameter, which are relative to one another.

1.5.2 Non-radiative energy transfer (NRET)

In non-radiative energy transfer (NRET), also known as Förster resonance energy transfer (FRET), excitons are transferred from an excited donor to a ground-state acceptor via a non-radiative near-field electrodynamic process. In order for this resonant process to work, there must be substantial overlap between the donor's emission spectrum and the acceptor's absorption spectrum. NRET is a multi-stage procedure (Figure 1.7). When a photon is taken in by the donor, an exciton is created in the n^{th} excited state. This exciton transfers phonons to the crystal lattice in order to rapidly relax to the ground state. The thermalized exciton subsequently transfers its energy to the acceptor via a dipole-dipole interaction that causes the annihilation of the exciton in the donor while creating an exciton in the acceptor. The exciton produced by NRET can then be broken to electron-hole pair or thermalize in the acceptor and recombine through photon emission. Distance between molecules in biology and chemistry is commonly measured using NRET, which was pioneered by T. Förster.[44] Many NRET-optoelectronic devices have been proposed and proven, both for illumination[45] and light harvesting applications.[46,47] NRET naturally also applies to excitons in inorganic semiconductors.[48]

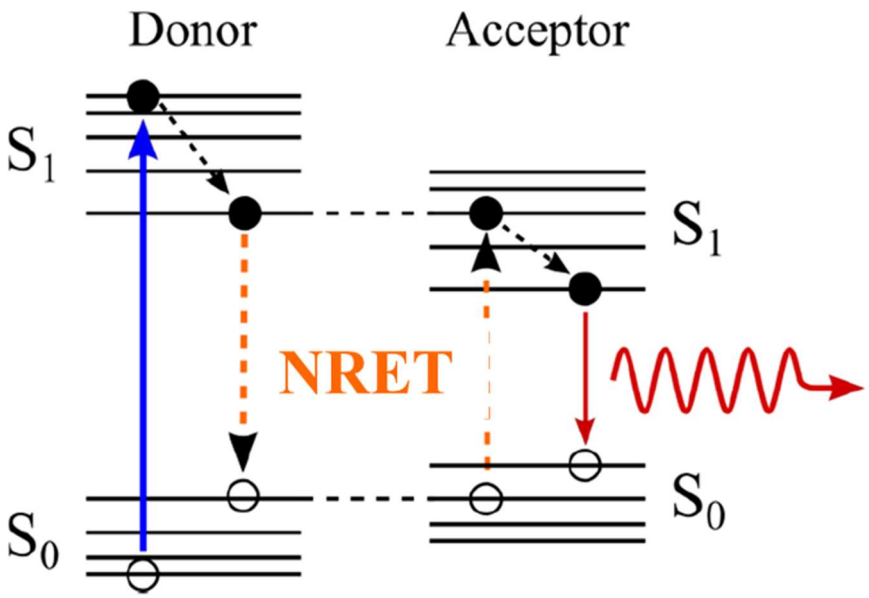

Figure 1.7 A simplified diagram of the NRET process.

1.5.3 SiQDs

Silicon is nontoxic, can be easily extracted from SiO_2, and is found in large quantities.[49] Si, like many materials, exhibits size-dependent characteristics when it is produced at the nanoscale.[50] For example, silicon nanocrystals (Si-NCs) with dimensions smaller than 5 nm emit redder light when exposed to UV light, in line with the principles of quantum confinement.[51,52] Consistent with this, Si-NCs with sizes larger than 5 nm emit light in the infrared. Si-NCs also exhibit reactivity and unique electrical features, such as a tunable optical response, that have not been reported in bigger Si particles or the bulk semiconductor. Because of their adaptability in optical and electrical characteristics and their bio/environmental friendliness,[53] Si-NCs show great potential in a variety of applications. In addition, they are a promising nontoxic replacement for the currently used CdSe quantum dots. There have been prototypes of sensors[54], solar cells[55], and LEDs[56] based on Si-NC since 2015.

There are a variety of documented ways for manufacturing Si-NCs, including both gas- and solid-phase protocols in addition to those that use solution-based techniques. In order to synthesize Si-NCs, Veinot's group came up with a simple and adaptable process involving heat treatment of a silicon-rich oxide resin generated from sol-gel that solely consists of Si, O, and H.[51] This high purity precursor allows for the inclusion of dopants while minimizing the risk of contaminants.[57] Setting a maximum processing temperature and/or time is a simple way to fine-tune the Si-NC size. Synthetic chemistry laboratories may create high purity Si-NCs with equipment and methods that are commonplace with only a small investment in a high temperature tube furnace. The whole method yields freestanding particles of sizes from a few to hundreds of nanometers, however the vast majority of research has been done on Si-NCs with a diameter of 15 nm or less.[51,58] In addition, highly luminous Si-NC/SiO_2 thin films are easily shaped or integrated into optical devices using a variation of this process that is outside

the scope of this thesis.[58] First described by Liu et al., Si-NCs are prepared by thermally annealing silicon suboxide powders (SiO_x, x = 0.4-1.8) in an inert environment at 900 °C.[59] Freestanding hydride terminated Si-NCs with a mean diameter of 4.2 nm were produced using HF etching. This set the stage for the creation of the technique presented in this thesis, which involves thermally processing commercially available hydrogen silsesquioxane (HSQ, $HSiO_{1.5}$) under a slightly reducing environment to generate Si-NCs in large numbers.[51] The tendency of elemental Si-NCs to oxidize in the presence of air and water is a major issue. The reactive hydride surface is reduced by oxidation, crystallinity is broken, and the intensity of photoluminescence can be affected. Dangling-bond type defects ($Si_3 \equiv Si\cdot$) are formed at the interface between the crystalline Si core and the surface oxide layer if the surface of Si were even partly oxidized.[60–63] P_b centers are the name given to these defects. Their primary function is to serve as recombination sites for carriers, which they do by inducing deep levels in the Si band gap's midsection. Covalent termination of ligands to the surface, however, can reduce oxidation.[64] Stronger stability of the particles against oxidation is provided by the covalent connection. Further, surface termination may be accomplished with a large number of different functional groups.

1.6 Metal-semiconductor (Schottky) junction

If a semiconductor and a conductor are brought into contact with each other, the junction formed can be either an ohmic or a Schottky junction.[65] An ohmic contact, seen in Figure 1.8 (a)[66], is formed when the conductor's work function is less than that of the semiconductor. Because they don't significantly restrict electron transport between the materials, ohmic contacts are frequently preferred for electrical connections. A Schottky contact, seen in Figure 1.8 (b)[66], can be created between a conductor and a semiconductor if the former's work function is greater than the latter's. This is sometimes avoided due to the fact that it might impede the flow of electrons between the two. Schottky junctions are occasionally manufactured on purpose for use in devices like diodes, sensors, and solar cells due to their rectifying properties. Most Schottky diodes are constructed with an n-type semiconductor and a high work function conductor. While the opposite configuration can provide a p-type Schottky diode, it is far less frequent than the n-type, which is why we'll be focusing on that here. Although silicon and silver (Ag) are the most common semiconductor and conductor, respectively, in this junction, many other semiconductor-conductor pairings are feasible.[67]

Due to the lower Fermi level in the conductor, electrons from the n-type semiconductor can tunnel to the vacant lower energy levels when the two materials are brought together. This results in a depletion of the semiconductor and a negative charge in the conductor, bringing about a state in which the Fermi levels are in equilibrium. Once the temperature reaches a stable value, thermal equilibrium sets in, and an electron depletion area with a width of W in the semiconductor forms at the junction.

Because the depletion zone causes an intrinsic electric field E_0 and intrinsic potential V_{bi} in the semiconductor, the conduction and valence bands of the semiconductor are displaced higher towards the junction. One of the most prominent features of the electrical characteristics of a Schottky junction is the formation of a barrier Φ_{B0} at the interface with the semiconductor conduction band.[68]

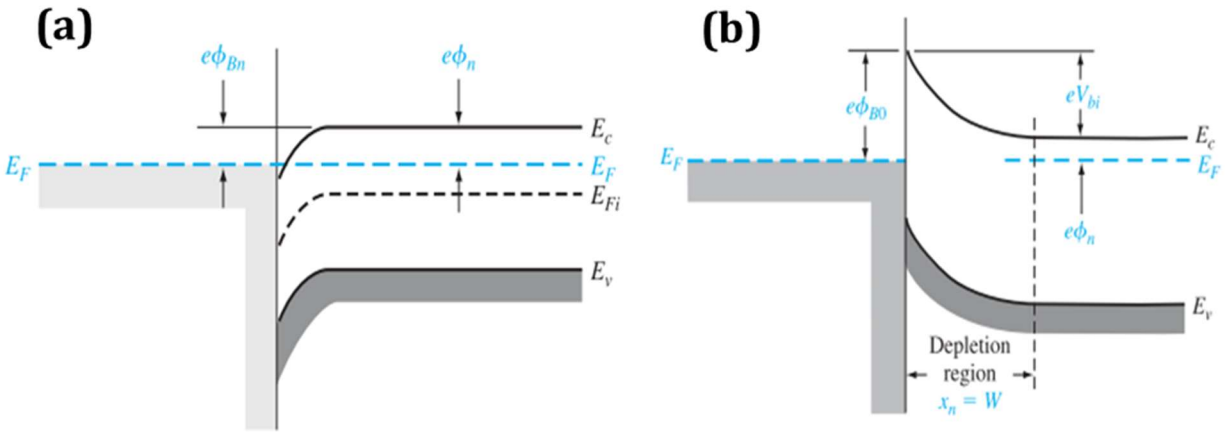

Figure 1.8 (a) Ohmic junction band diagram for a small work function conducting material and an n-type semiconductor. (b) Band diagram of an n-type semiconductor in a Schottky junction with a high work function conductor.

1.6.1 Schottky junction diode

Applying a modest voltage across the Schottky junction's conductor and semiconductor causes Φ_{B0} and eV_{bi} to behave as shunts, blocking the flow of electrons. Figure 1.9 (b) [66] illustrates the low current that results when a forward bias is given, causing electrons to flow from the semiconductor to the conductor. This current is due to the electrons' need to first overcome eV_{bi} through thermal emission. This barrier can easily identified by:

$$V_{bi} = \Phi_m - \Phi_n \qquad (1.1)$$

Increasing the voltage applied raises the conduction band and lowers the barrier to $e(V_{bi} - V_a)$. The forward current I_f under the forward voltage V_a rises dramatically as the barrier becomes less of a barrier for the electrons and may be found by using the formula:

$$I = I_0 \left[\exp\left(\frac{eV}{k_B T}\right) - 1\right] \qquad (1.2)$$

where I_0 represents the reverse saturation current for a certain material.

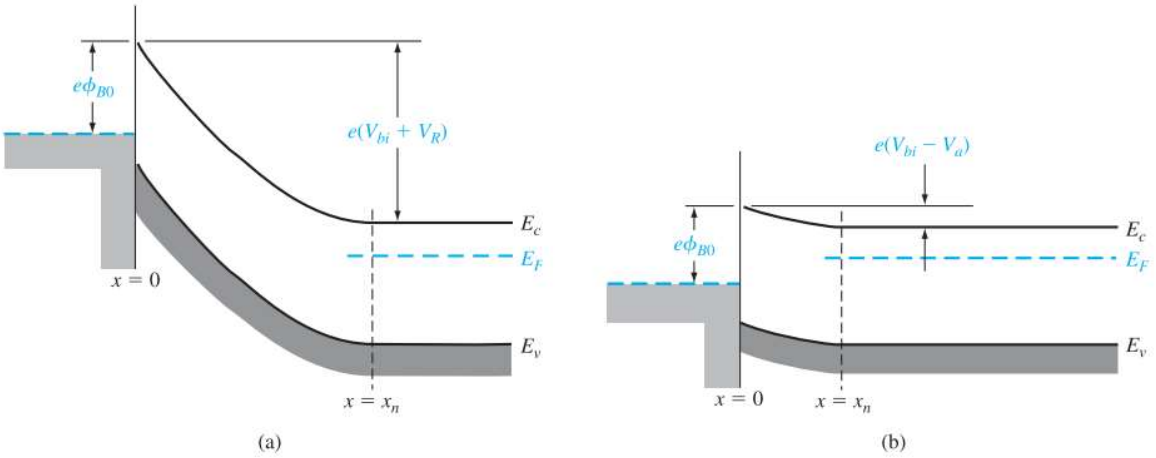

Figure 1.9 A n-type Schottky junction diode's band diagrams under (a) reverse and (b) forward voltage bias.

The electrons in the conductor must get through the barrier Φ_{B0} when a reverse bias is used and electrons try to flow from the conductor to the semiconductor, as shown in Figure 1.9 (a). The barrier is provided by:

$$\Phi_{B0} = \Phi_m - X \qquad (1.3)$$

where X is the electron affinity for semiconductor. When this barrier is high, relatively few electrons can cross it by thermal emission, which results in very little current flow. The semiconductor's conduction band is pushed down as the applied voltage rises. Because Φ_{B0} stays constant, the current does not vary appreciably when the voltage rises. This current maintains its reverse saturation value because of thermionic emission, as described by:

$$I_0 = AA^*T^2 \exp\left(\frac{-e\Phi_{B0}}{k_B T}\right) \qquad (1.4)$$

where A*is the semiconductor-dependent effective Richardson constant. As a result, current can flow via one direction but not the other and the forward and reverse biases behave differently. The junction may be scaled down to small proportions and is highly helpful as a diode thanks to its rectifying property.

1.6.2 Conduction mechanisms

Some of the conduction processes under study are reliant on the electrode-semiconductor contact's electrical characteristics. Electrode-limited and bulk-limited conduction processes are the terms used to describe these mechanisms.[69] There are several conduction processes, and they can all contribute to the conduction current across the semiconductor layer, making it crucial to have means to differentiate between them. We may be able to learn more about the make-up of the conduction currents by measuring the temperature-dependent conduction currents, as numerous conduction processes depend on temperature in different ways. Schottky or thermionic emission, and Fowler-Nordheim tunneling are examples of the conduction processes that are constrained by the electrodes. Poole-

Frenkel (P-F) conduction, ohmic conduction, and space-charge-limited conduction are all examples of bulk-limited conduction processes. The most important parameter in the electrode-limited conduction mechanisms is the barrier height at the electrode-semiconductor interface.

1.6.2.1 Thermionic emission

Thermionic emission, also known as Schottky emission, is a conduction process in which the electrons in the semiconductor overcome the energy barrier at the metal semiconductor interface and flow into the metal if they are able to receive enough energy via thermal activation. It is important to keep in mind that the barrier's height, and not its form, is the most important determining factor. Thermionic emission causes a current that is very sensitive to temperature. The Schottky-barrier diode, or metal-semiconductor junction, is the most widely used semiconductor barrier diode. To ensure that thermionic emission is the dominant mechanism, as shown in Figure 1.10, the barrier layer's internal collision and drift-diffusion processes must be small.

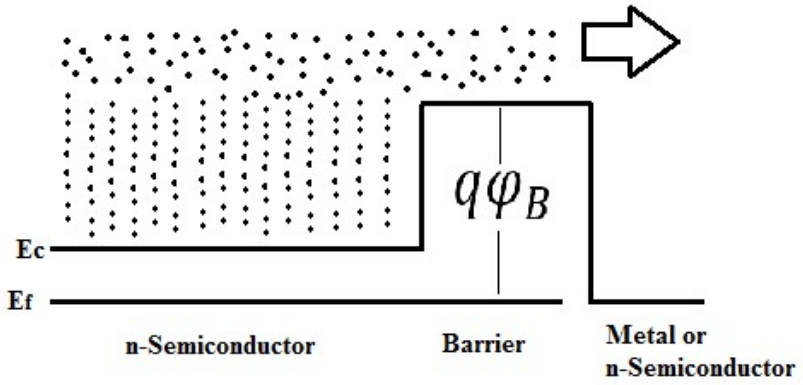

Figure 1.10 Energy-band diagram showing thermionic emission of electrons over the barrier.

As a function of energy above the conduction band edge, the density of electrons (for n-type substrate) falls exponentially according to Fermi-Dirac statistics. The carrier density does not equal zero at any nonzero temperature. The sum of carriers exceeding the barrier height is of particular significance. This fraction of the thermally produced carriers contribute to the thermionic-emission current because they are no longer trapped by the barrier. Over the barrier, the total electron current is calculated as:[66]

$$J = A^{*}T^{2}\exp\left(\frac{-e\Phi_{B}}{k_{B}T}\right) \qquad (1.5)$$

A* is the effective Richardson constant, which depends on the effective mass.

The image force may reduce the height of the energy barrier between metal and semiconductors. Schottky effect refers to the reduction of a barrier that occurs as a result of an image force.

1.6.2.2 Fowler-Nordheim tunneling

The thermionic emission model described above may account for most of the observed electrical characteristics of the metal-semiconductor contact at elevated temperatures. This does not, however,

fully account for the saturation tendency that becomes apparent at low temperatures. Other transport processes must be included in order to provide a full explanation of the temperature dependency of conductivity.

When the incoming electrons' energy is less than the potential barrier, the electrons are reflected as predicted by classical physics. Although the electron wave function cannot pass through a potential barrier thicker than a hundred Angstroms, the quantum process predicts that it will do so when the barrier is sufficiently thin. Accordingly, due to the tunneling effect, the likelihood of electrons existing on the other side of the potential barrier is not zero.

When the electric field is strong enough, the electron wave function can tunnel through the triangle-shaped potential barrier and enter the conduction band of semiconductor, a phenomenon known as tunneling. The equation for the tunneling current is:[70]

$$J = \frac{q^3 E^2}{8\pi h q \varphi_B} exp\left[\frac{-8\pi(2qm_T^*)^{1/2}}{3h}\varphi_B^{3/2}\right] \qquad (1.6)$$

where m_T^* is the tunneling effective mass in semiconductor, E is the electric field across the barrier.

The current-voltage (*I-V*) characteristics of the device may be measured at extremely low temperatures, allowing the tunneling current to be extracted. With the temperature so low, the tunneling current dominates over the thermionic emission, and this current is practically temperature independent.

1.6.2.3 Poole-Frenkel

It is possible for electrons to be thermally excited in traps and then to emit into the conduction band of the semiconductor, a process known as Poole-Frenkel (P-F) emission. Therefore, P-F emission is also known as the internal Schottky emission. The Coulomb potential energy of an electron trapped in a trapping center can be decreased by applying an electric field across the semiconductor layer. As the potential energy drops, there may be a greater chance that an electron may be thermally stimulated out of the trap and into the dielectric's conduction band. Figure 1.11[71] depicts a simplified version of the energy band diagram for P-F emission. In the case of a Coulombic attraction potential between electrons and traps, the current density caused by the P-F emission is: [69]

$$\boldsymbol{J = q\mu N_c E exp\left[\frac{-q\left(\phi_T - \sqrt{\frac{qE}{\pi\varepsilon_r\varepsilon_0}}\right)}{kT}\varphi_B^{3/2}\right]} \qquad (1.7)$$

where ϕ_T is the trap energy level, μ is the electronic drift mobility, and N_c is the density of states in the conduction band.

Given that P-F emission results from thermal activation in an electric field, this conduction mechanism is often observed at extreme conditions (high temperature and electric field).

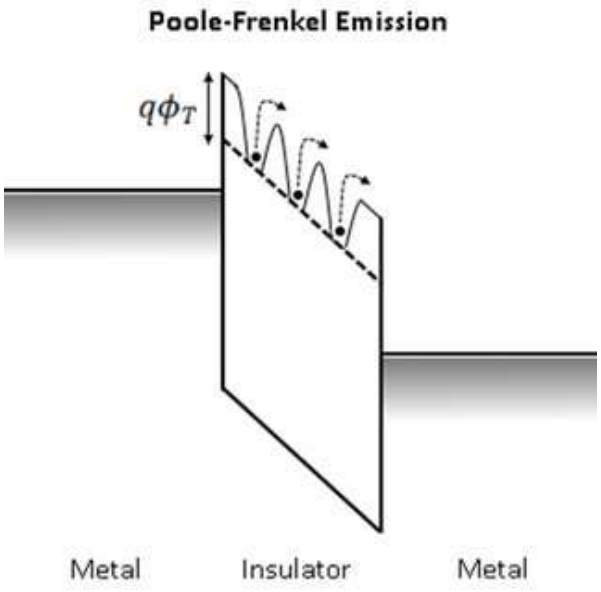

Figure 1.11 Schematic energy band diagram of Poole-Frenkel emission in metal-insulator-metal structure.

1.6.2.4 Space-charge limited conduction

When talking about semiconductors and insulators, "space charge" refers to the amount of empty space that is either positively or negatively charged.

If the cathode generates more electrons per second than the surrounding space can accommodate, for instance, the excess electrons will combine to form a negative space charge, resulting in a field that slows the cathode's electron production. The bulk of the semiconductor or insulator, i.e., the carrier mobility inside the material, governs the current rather than the electron injecting electrode.

When the rate of charge carrier injection from the contacting electrodes into the conduction band or valance band of a semiconductor or insulator is greater than the rate of recombination, space-charge limited dark conduction occurs. Therefore, this conduction mechanism is bulk limited. Once the carrier-injecting contact can supply a reservoir of carriers, the characteristics of the material through which the carriers are flowing govern the behavior of the injected carriers and, by extension, the current. High intrinsic resistivity is a result of limited carrier mobility due to the large forbidden energy gap in molecular crystals. The inherent resistance of the material is typically considerably bigger than the contact resistance, making it easy to monitor the SCL current even if the carrier-injecting contact is not ideal. Since there are no ideal crystals in the universe, traps resulting from imperfection of any kind are always present in crystals and interact with injected carriers from ohmic contacts to regulate carrier flow and set the current-voltage (*J*-*V*) characteristics.[72] First presented by Mott and Gurney (1940), the idea of space-charge-limited current between plane parallel electrodes has been developed further by a number of authors, including Lampert (1956). The Mott-Gurney law [73] describes the current density in the absence of trapping effects is:

$$J = \frac{9}{8}\mu\epsilon\epsilon_o\frac{V^2}{L^3} \qquad (1.8)$$

where L is the distance between the electrodes. In the case of nonuniform special traps presence as shown in Figure 1.12,[72] a modified form of the previous equation is used as will be discussed in chapter 5.

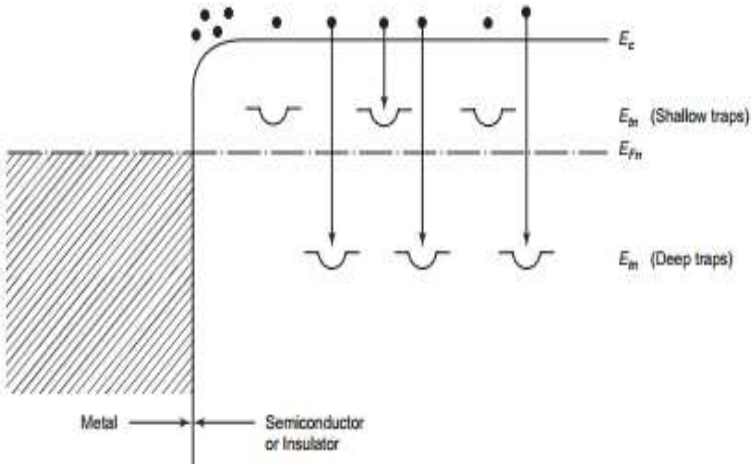

Figure 1.12 Energy level diagrams for electrons injected into a semiconductor from an ohmic contact, showing both shallow and deep electron traps.

1.6.3 Schottky junction photovoltaic

It is simple to use a Schottky diode for photovoltaics.[65] The semiconductor's Fermi level is greater than that the metal before they make contact. But when the two are brought together, electrons flow from the semiconductor into the metal's lower energy states, creating a balanced Fermi level where the depletion region and Schottky barrier are formed. When the Schottky diode is illuminated, as in Figure 1.13 [74], photons from the light can excite electrons in either the conductor or semiconductor. Due to its capacity for charge separation, the depletion area is the traditional target region for light absorption. Electron-hole pairs are created in semiconductors when light with energy exceeding the band gap is absorbed. The electric field in the depletion area accelerates the electron's migration to the bulk of the semiconductor. Additionally, the hole travels to the conductor where it recombines with its electrons. The Schottky barrier makes it challenging for carriers to go backward, which causes the charge to accumulate and create a voltage potential. Electrons will go from the semiconductor to the electrode and do work as a basic solar cell if the semiconductor and conductor are linked by a circuit with an external load.

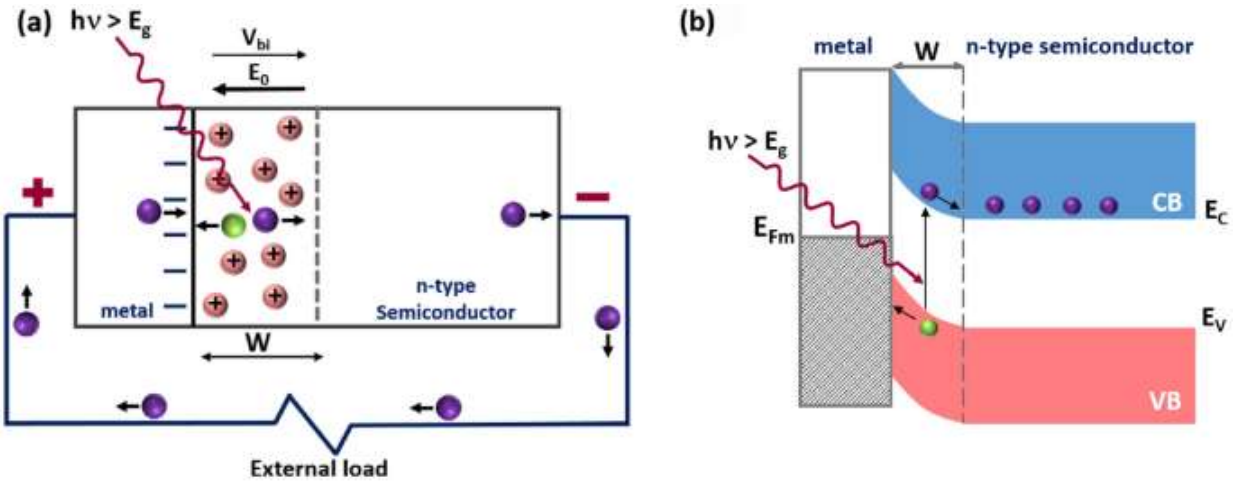

Figure 1.13 The Schottky junction's electron-hole pair is shown (a) in a circuit and (b) in an energy band structure.

When photons are absorbed by a conductor, the electrons may obtain enough energy to cross the barrier and add to the solar cell's current. However, this is a negligible effect, and hence the thickness of the conductor is often lowered to allow photons to flow through. Since charge separation is hindered if photons are absorbed in the n-type semiconductor's neutral zone, it is preferable to maximize photon absorption in the depletion region. Light often shines from the conductor side since a contact must be linked to the semiconductor. Therefore, it's imperative that the majority of the light be absorbed very next to the device's top surface. When the circuit is reverse biased, the Schottky diode also functions as a photodetector. Observable current is produced when an external potential is supplied, which rapidly accelerates carrier separation. There are a lot of benefits to using Schottky junction photovoltaics. Firstly, the design is elementary in both idea and implementation. The construction is straightforward: just combine two materials to create a barrier. Raising the barrier height by manipulating the work functions of the materials improves solar cell and photodetector performance. Optimizing the conductor to have both high light transmission and conductivity is possible. Since the semiconductor necessitates no unique conditions, developing such devices is a simple. Second, there isn't a lot of materials needed to build a basic cell. These devices can be manufactured at minimal cost since the conductor, semiconductor, and contacts can all be constructed from inexpensive materials. A third advantage is that they may be fabricated to an extremely fine thickness. Thin film photovoltaics are a viable option since a thin conductor is required and most of the light absorption occurs near the surface. Schottky junction photovoltaics have many potential applications, notably as solar cells, but they have not yet seen broad use. The primary reason for this is due to the fact that metals were the obvious first choice for use as the conductors. Due to its high work function and conductivity, gold is the best metal to utilize. While Schottky junction photovoltaics have made great strides in recent years, they lagged behind the competition because metal films present various problems that constrained the greatest efficiencies that could be reached. The main problem is that metal contacts have a low light transmittance but still

need to let light through. The metal will become transparent at the nanoscale, but its resistance will grow dramatically. Although this is optimizable, the resulting photocurrent is poor. Gold is expensive and inconvenient to utilize in big quantities, therefore it drives up the cost of solar cells. Typically, the work functions of inexpensive metals are not enough. So, advancements in Schottky junction solar cells will be halted until new ideas are found to improve performance without increasing prices.

1.7 Transition metal oxides (TMO) as selective contact

The capacity of a contact to transmit one kind of carrier (electrons/holes) while blocking the other type (holes/electrons) is known as contact selectivity in the context of photovoltaics. The contact is referred to as a "electron selective contact (ESC)" or a "hole blocking contact" (HBC). Hole Selective Contact (HSC)/Electron Blocking Contact is the other form of contact that permits holes to pass but prevents electrons (EBC).

The production of photovoltaic energy involves three main steps:

1-Absorption of light and the production of charge carriers.

2-Separation of charge carriers and their delivery to the contacts.

3- Extract the carrier and supply power to the load.

Typically, a p+/n^-/n+ or n+/p^-/p+ homojunction generated by doping c-Si is capable of all three operations. The absorber is the thickest part of the cell and is located in the center, where the n- and p-type doping ratio is lowest. It creates electron-hole pairs by absorbing light. The need for lateral conduction and contact resistance often dictate the thickness of the contact zones. Each contact in an n+ and p+ pair allows just one type of carrier to pass while blocking the other. This band bending between the differentially doped junctions is essential to the contacts' blocking effect. In order to separate electron-hole pairs, a force must be applied, and this is generated by the strong electric field present in the areas adjacent to the junction. The quasi-neutral area is located between the junction region and the bulk of the material, and it is here that diffusion is the major mode of transport.

To prevent the dark current while enabling the photocurrent, a nanometer-thin selective contact inter layer (electron blocking layer and hole blocking layer) is utilized here between the metal and silicon. When compared to Si, electron blocking layer have a large offset in the conduction band and a little offset in the valence band, whereas hole blocking layer have a large offset in the valence band and a small offset in the conduction band. Either a semiconductor or an insulator can be used. This contacting approach is based on the fact that the number of trap states at the heterojunction between two semiconductors or semiconductor/insulator is many orders of magnitude smaller than at the metal/semiconductor interface, while being far from perfect. Therefore, the contact recombination

current may be drastically lowered, facilitating enhanced carrier control. In addition, the forward bias diode injection current will be entirely stopped if the minority carrier has a high band offset. Having a low band offset for the dominant carrier means that the photo-generated current will be able to flow unimpeded. In an ideal scenario, the electron blocking layer/Si or hole blocking layer/Si interface would be fully passivated. Although a perfectly smooth interface is impossible to guarantee in practice, effective passivation can be achieved by experimenting with various surface treatments and annealing strategies.

In solar cells, transition metal oxides (TMO) have the potential to function as a selective contact layer.[75–78] The most essential features of TMO that may be put to use in this context are (i) its capacity to be doped from defects or extrinsic dopant species, (ii) its typically broad bandgap that is transparent to the visible spectrum of sunlight, and (iii) its considerably changing band lineup with Si. Because of their wide range of useful features, vanadium oxide (VO_x) thin films are extremely promising. Many techniques are used to prepare them, sol-gel technique is of considerable interest due to its simplicity and low cost, and the quality of films produced using this method can be equally as good as those synthesized by the other highly sophisticated methods.

1.8 PEDOT:PSS/Si heterojunction

Poly(3,4-ethylenedioxythiophene) poly(styrenesulfonate) (PEDOT:PSS or just PEDOT) may be made to be both highly conductive and transparent, giving it several potential uses.[79] In the class of polythiophenes, PEDOT:PSS is among the most well-known for its electrical activity. PEDOT:PSS may be used to achieve conductivities of up to 1000 S/cm with work functions adjustable between 4.8 and 5.2 eV. Because of these two characteristics, PEDOT:PSS is a promising organic material to achieve carrier-selectivity in heterojunction solar cells. Organic photovoltaic systems employ them as hole contacts, flexible transparent electrodes, and as a static dissipative coating.[80–82] A heterojunction formed by coating an n-type crystalline silicon wafer with a semiconductor material acts as a high-quality rectifying diode when used in solar panels. Typically, PEDOT:PSS is sold as an aqueous solution. As a result, PEDOT:PSS may be used in a wide range of solution-based coating processes, raising their potential as a cost-effective, high-volume production technique.[83] Unlike traditional p-n junction solar cells, which need temperatures of up to 800 degrees Celsius during fabrication, PEDOT:PSS/Si solar cells may be made at temperatures as low as 100 degrees Celsius.

Band diagrams for a PEDOT/Si device and a Schottky-junction device under illumination and modest forward bias are shown in Figure 1.14. Electrons and holes are shown in the band diagrams by the solid and void circles, respectively. Dark current is depicted by the dotted lines, while light current is shown by the solid ones.

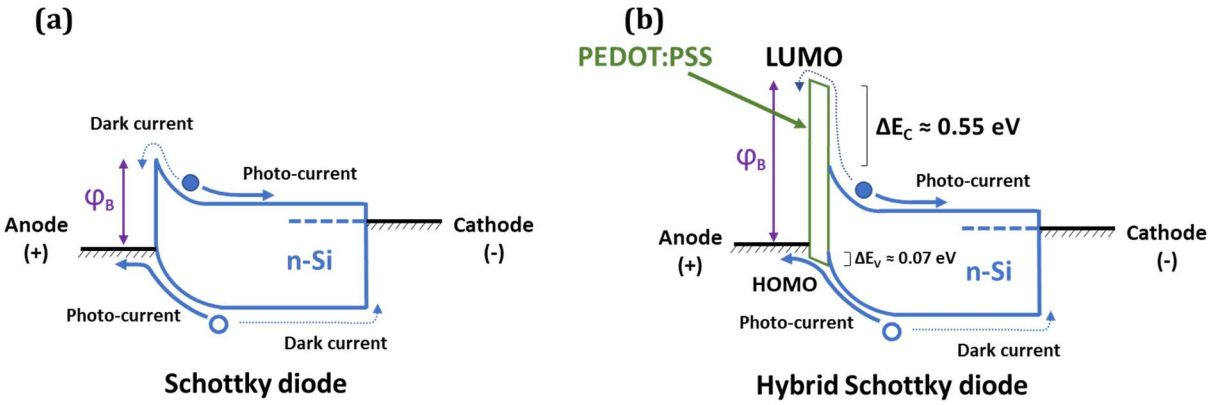

Figure 1.14 Band diagrams of illuminated photovoltaic devices. (a) Basic Schottky junction device (b) PEDOT:PSS/Si device.

Electrons in the conduction band do not flow from the cathode to the anode in the Schottky-junction shown in Figure 3.14 (a) because of the internal electric field created by the diode. However, the barrier hindering the recombination of electrons at the anode is relatively small, which leads to a saturation current density that is usually greater than desired, which deteriorates the open-circuit voltage (V_{OC}). Figure 3.14 (b) shows a PEDOT:PSS/Si device in which the conduction band electrons of silicon are prevented from entering the PEDOT:PSS by the electric field in silicon and the offset of the PEDOT:PSS LUMO from the conduction band E_C of silicon. In contrast, holes can flow towards the anode and transport photocurrent due to the lack of an offset between the silicon valence band and the PEDOT:PSS HOMO level. This configuration reduces the recombination at the anode and minimizes the hole barrier so that the V_{OC} can be increased and the J_{SC} value is safely maintained. The dark current in the PEDOT:PSS/Si device is carried by holes injected into the body of the n-type silicon due to the tiny barrier to hole current present in the device.[84]

1.9 Thesis outlines

In the thesis presented here, the improvement of solar cell properties caused by the NRET effect was sought after to enhance the short circuit current (J_{SC}) which was extra improved by the means of nanowires structure. This thesis also seeks to replace the diffused homojunctions that allow standard silicon solar cells to achieve high efficiency with low-temperature heterojunctions in an effort to reduce production costs. SiQDs were inserted between PEDOT:PSS and Si nanostructures of hybrid heterojunction solar cells. A comparative investigation was conducted to investigate the relationship between the different passivation ligands and their lengths to improve the NRET effect. In parallel, different VO_x thin films were fabricated with different oxidation states (V_2O_{5-x}, VO_{2-x}) using a simple solution processing-based technique and annealed in different atmospheres in an attempt to replace PEDOT:PSS films with weak stability. The hole-injection ability of the fabricated VO_x films was

investigated after their utilization in SiNWs-based solar cells. As far as the thesis author know, this is the first time that non-toxic VO_{2-x} films have been formed by reducing V_2O_5 films for use as a hole injection layer in Si-based solar cells. Because VO_x films exhibit high stability with hole injection ability when utilized in solar cells, a greater understanding of the current transport mechanism in VO_{2-x}/Si heterojunction diode was required, and this was studied in dark at different temperatures.

1.10 References

[1] World Energy Outlook 2022 – Analysis - IEA, (n.d.). https://www.iea.org/reports/world-energy-outlook-2022 (accessed December 15, 2022).

[2] The Sun as an Energy Resouce, (n.d.). https://www.volker-quaschning.de/articles/fundamentals1/index.php (accessed December 15, 2022).

[3] J. Yan, B.R. Saunders, Third-generation solar cells: a review and comparison of polymer:fullerene, hybrid polymer and perovskite solar cells, RSC Adv. 4 (2014) 43286–43314. https://doi.org/10.1039/C4RA07064J.

[4] AR5 Climate Change 2013: The Physical Science Basis — IPCC, (n.d.). https://www.ipcc.ch/report/ar5/wg1/ (accessed December 15, 2022).

[5] AR5 Climate Change 2014: Impacts, Adaptation, and Vulnerability — IPCC, (n.d.). https://www.ipcc.ch/report/ar5/wg2/ (accessed December 15, 2022).

[6] World Energy Outlook 2013 – Analysis - IEA, (n.d.). https://www.iea.org/reports/world-energy-outlook-2013 (accessed December 15, 2022).

[7] P.P. Khlyabich, B. Burkhart, A.E. Rudenko, B.C. Thompson, Optimization and simplification of polymer–fullerene solar cells through polymer and active layer design, Polymer (Guildf). 54 (2013) 5267–5298. https://doi.org/10.1016/J.POLYMER.2013.07.053.

[8] RENEWABLES 2022 GLOBAL STATUS REPORT, (n.d.). https://www.ren21.net/gsr-2022/ (accessed December 15, 2022).

[9] S. Sharma, K.K. Jain, A. Sharma, Solar Cells: In Research and Applications—A Review, Mater. Sci. Appl. 06 (2015) 1145–1155. https://doi.org/10.4236/MSA.2015.612113.

[10] M.M.A.V.M.M. Askari Mohammad Bagher, Types of Solar Cells and Application, Http://Www.Sciencepublishinggroup.Com. 3 (2015) 94. https://doi.org/10.11648/J.AJOP.20150305.17.

[11] P.-J. Ribeyron, Crystalline silicon solar cells: Better than ever, Nat. Energy. 2 (2017) 17067. https://doi.org/10.1038/nenergy.2017.67.

[12] F.C. Krebs, M. Hösel, M. Corazza, B. Roth, M. V. Madsen, S.A. Gevorgyan, R.R. Søndergaard, D. Karg, M. Jørgensen, Freely available OPV—The fast way to progress, Energy Technol. 1 (2013) 378–381. https://doi.org/10.1002/ENTE.201300057.

[13] A. McEvoy, L. Castañer, T. Markvart, Solar cells: Materials, manufacture and operation, Sol. Cells Mater. Manuf. Oper. (2012) 1–641. https://doi.org/10.1016/C2011-0-07789-X.

[14] R.Y. Srinivas B, Balaji S, Nagendra Babu M, Review on present and advance materials for solar cells., Int. J. Eng. Res. 12 (2015) 178–82.

[15] L. Noice, Progress on a Photovoltaic Cell Design Consisting of Silicon Nanowires and Poly (3-hexylthiophene), McNair Sch. Online J. 2 (2006) 309–319. https://doi.org/10.15760/mcnair.2006.309.

[16] ZSW achieves world record CIGS lab cell efficiency of 22.6% - PV Tech, (n.d.). https://www.pv-tech.org/zsw-achieves-world-record-cigs-lab-cell-efficiency-of-22-6/ (accessed December 16, 2022).

[17] S.N.F. Mohd-Nasir, M.Y. Sulaiman, N. Ahmad-Ludin, M.A. Ibrahim, K. Sopian, M.A. Mat-Teridi, Review of Polymer, Dye-Sensitized, and Hybrid Solar Cells, Int. J. Photoenergy. 2014 (2014) 1–12. https://doi.org/10.1155/2014/370160.

[18] Z. Zhu, D. Waller, R. Gaudiana, M. Morana, D. Mühlbacher, M. Scharber, C. Brabec, Panchromatic Conjugated Polymers Containing Alternating Donor/Acceptor Units for Photovoltaic Applications, Macromolecules. 40 (2007) 1981–1986. https://doi.org/10.1021/ma062376o.

[19] S. Gorjian, H. Ebadi, Introduction, in: Photovolt. Sol. Energy Convers., Elsevier, 2020: pp. 1–26. https://doi.org/10.1016/B978-0-12-819610-6.00001-6.

[20] Tomas Markvart, Solar Electricity, 2nd Edition, Synth. Lect. Power Electron. (2000) 298. https://www.wiley.com/en-us/Solar+Electricity%2C+2nd+Edition-p-9780471988526 (accessed December 16, 2022).

[21] D.M. Chapin, C.S. Fuller, G.L. Pearson, A New Silicon p-n Junction Photocell for Converting Solar Radiation into Electrical Power, JAP. 25 (1954) 676–677. https://doi.org/10.1063/1.1721711.

[22] A. Polman, M. Knight, E.C. Garnett, B. Ehrler, W.C. Sinke, Photovoltaic materials: Present efficiencies and future challenges, Science (80-.). 352 (2016). https://doi.org/10.1126/SCIENCE.AAD4424/SUPPL_FILE/POLMAN.SM.PDF.

[23] W. Shockley, H.J. Queisser, Detailed Balance Limit of Efficiency of p-n Junction Solar Cells, J. Appl. Phys. 32 (1961) 510–519. https://doi.org/10.1063/1.1736034.

[24] M.A. Green, S.P. Bremner, Energy conversion approaches and materials for high-efficiency photovoltaics, Nat. Mater. 16 (2017) 23–34. https://doi.org/10.1038/nmat4676.

[25] A. Luque, A. Martí, C. Stanley, Understanding intermediate-band solar cells, Nat. Photonics. 6 (2012) 146–152. https://doi.org/10.1038/nphoton.2012.1.

[26] T. Trupke, M.A. Green, P. Würfel, Improving solar cell efficiencies by down-conversion of high-energy photons, J. Appl. Phys. 92 (2002) 1668–1674. https://doi.org/10.1063/1.1492021.

[27] A. Rao, R.H. Friend, Harnessing singlet exciton fission to, (2017). https://doi.org/10.1117/2.1201203.004146.

[28] J.M. Spurgeon, H.A. Atwater, N.S. Lewis, A comparison between the behavior of nanorod array and planar Cd(Se, Te) photoelectrodes, J. Phys. Chem. C. 112 (2008) 6186–6193. https://doi.org/10.1021/jp077481u.

[29] N. Fukata, T. Subramani, W. Jevasuwan, M. Dutta, Y. Bando, Functionalization of Silicon Nanostructures for Energy-Related Applications, Small. 13 (2017) 1–13. https://doi.org/10.1002/smll.201701713.

[30] N. Fukata, Impurity Doping in Silicon Nanowires, Adv. Mater. 21 (2009) 2829–2832. https://doi.org/10.1002/adma.200900376.

[31]A.I. Hochbaum, P. Yang, Semiconductor Nanowires for Energy Conversion, Chem. Rev. 110 (2010) 527–546. https://doi.org/10.1021/cr900075v.

[32] R. Ulbricht, R. Kurstjens, M. Bonn, Assessing Charge Carrier Trapping in Silicon Nanowires Using Picosecond Conductivity Measurements, Nano Lett. 12 (2012) 3821–3827. https://doi.org/10.1021/nl3017835.

[33] E. Garnett, P. Yang, Light Trapping in Silicon Nanowire Solar Cells, Nano Lett. 10 (2010) 1082–1087. https://doi.org/10.1021/nl100161z.

[34] M.D. Kelzenberg, S.W. Boettcher, J.A. Petykiewicz, D.B. Turner-Evans, M.C. Putnam, E.L. Warren, J.M. Spurgeon, R.M. Briggs, N.S. Lewis, H.A. Atwater, Enhanced absorption and carrier collection in Si wire arrays for photovoltaic applications, Nat. Mater. 9 (2010) 239–244. https://doi.org/10.1038/nmat2635.

[35] B. Fazio, P. Artoni, M. Antonia Iatì, C. D'Andrea, M.J. Lo Faro, S. Del Sorbo, S. Pirotta, P. Giuseppe Gucciardi, P. Musumeci, C. Salvatore Vasi, R. Saija, M. Galli, F. Priolo, A. Irrera, Strongly enhanced light trapping in a two-dimensional silicon nanowire random fractal array, Light Sci. Appl. 5 (2016) e16062–e16062. https://doi.org/10.1038/lsa.2016.62.

[36] M. Dutta, N. Fukata, Low-temperature UV ozone-treated high efficiency radial p-n junction solar cells: N-Si NW arrays embedded in a p-Si matrix, Nano Energy. 11 (2015) 219–225. https://doi.org/10.1016/j.nanoen.2014.10.028.

[37] S.M. Wallace, W. Jevasuwan, N. Fukata, On-site growth method of 3D structured multi-layered graphene on silicon nanowires, Nanoscale Adv. 2 (2020) 1603–1612. https://doi.org/10.1039/d0na00098a.

[38] Alta Devices Achieves 30.8% Efficiency Record with New Generation Solar Cell Technology | Business Wire, (n.d.). https://www.businesswire.com/news/home/20130304005498/en/Alta-Devices-Achieves-30.8-Efficiency-Record-with-New-Generation-Solar-Cell-Technology (accessed December 17, 2022).

[39] E. Klampaftis, D. Ross, K.R. McIntosh, B.S. Richards, Enhancing the performance of solar cells via luminescent down-shifting of the incident spectrum: A review, Sol. Energy Mater. Sol. Cells. 93 (2009) 1182–1194. https://doi.org/10.1016/j.solmat.2009.02.020.

[40] H.-J. Muffler, M. Bär, I. Lauermann, K. Rahne, M. Schröder, M.C. Lux-Steiner, C.-H. Fischer, T.P. Niesen, F. Karg, Colloid attachment by ILGAR-layers: Creating fluorescing layers to increase quantum efficiency of solar cells, Sol. Energy Mater. Sol. Cells. 90 (2006) 3143–3150. https://doi.org/10.1016/j.solmat.2006.06.034.

[41] O. Chen, J. Zhao, V.P. Chauhan, J. Cui, C. Wong, D.K. Harris, H. Wei, H.-S. Han, D. Fukumura, R.K. Jain, M.G. Bawendi, Compact high-quality CdSe–CdS core–shell nanocrystals with narrow emission linewidths and suppressed blinking, Nat. Mater. 12 (2013) 445–451. https://doi.org/10.1038/nmat3539.

[42] L.E. Brus, Electron–electron and electron-hole interactions in small semiconductor crystallites: The size dependence of the lowest excited electronic state, J. Chem. Phys. 80 (1984) 4403–4409. https://doi.org/10.1063/1.447218.

[43]A.M. Smith, S. Nie, Chemical analysis and cellular imaging with quantum dots, Analyst. 129 (2004) 672. https://doi.org/10.1039/b404498n.

[44] T. Forster, Energiewanderung und Fluoreszenz, Naturwissenschaften 1946 336. 33 (1946) 166–175. https://doi.org/10.1007/BF00585226.

[45] S. Chanyawadee, P.G. Lagoudakis, R.T. Harley, M.D.B. Charlton, D. V. Talapin, H.W. Huang, C.-H. Lin, Increased Color-Conversion Efficiency in Hybrid Light-Emitting Diodes utilizing Non-Radiative Energy Transfer, Adv. Mater. 22 (2010) 602–606. https://doi.org/10.1002/adma.200902262.

[46] S. Lu, A. Madhukar, Nonradiative resonant excitation transfer from nanocrystal quantum dots to adjacent quantum channels, Nano Lett. 7 (2007) 3443–3451. https://doi.org/10.1021/nl0719731.

[47] H.M. Nguyen, O. Seitz, W. Peng, Y.N. Gartstein, Y.J. Chabal, A. V. Malko, Efficient radiative and nonradiative energy transfer from proximal CdSe/ZnS nanocrystals into silicon nanomembranes, ACS Nano. 6 (2012) 5574–5582. https://doi.org/10.1021/nn301531b.

[48] M. Achermann, M.A. Petruska, S. Kos, D.L. Smith, D.D. Koleske, V.I. Klimov, Energy-transfer pumping of semiconductor nanocrystals using an epitaxial quantum well, Nature. 429 (2004) 642–646. https://doi.org/10.1038/nature02571.

[49] S. Bhattacharjee, I.M.C.M. Rietjens, M.P. Singh, T.M. Atkins, T.K. Purkait, Z. Xu, S. Regli, A. Shukaliak, R.J. Clark, B.S. Mitchell, G.M. Alink, A.T.M. Marcelis, M.J. Fink, J.G.C. Veinot, S.M. Kauzlarich, H. Zuilhof, Cytotoxicity of surface-functionalized silicon and germanium nanoparticles: the dominant role of surface charges, Nanoscale. 5 (2013) 4870. https://doi.org/10.1039/c3nr34266b.

[50] C.M. Hessel, D. Reid, M.G. Panthani, M.R. Rasch, B.W. Goodfellow, J. Wei, H. Fujii, V. Akhavan, B.A. Korgel, Synthesis of Ligand-Stabilized Silicon Nanocrystals with Size-Dependent Photoluminescence Spanning Visible to Near-Infrared Wavelengths, Chem. Mater. 24 (2012) 393–401. https://doi.org/10.1021/cm2032866.

[51] C.M. Hessel, E.J. Henderson, J.G.C. Veinot, Hydrogen Silsesquioxane: A Molecular Precursor for Nanocrystalline Si–SiO 2 Composites and Freestanding Hydride-Surface-Terminated Silicon Nanoparticles, Chem. Mater. 18 (2006) 6139–6146. https://doi.org/10.1021/cm0602803.

[52] M. Dasog, K. Bader, J.G.C. Veinot, Influence of Halides on the Optical Properties of Silicon Quantum Dots, Chem. Mater. 27 (2015) 1153–1156. https://doi.org/10.1021/acs.chemmater.5b00115.

[53] M. Iqbal, T.K. Purkait, G.G. Goss, J.R. Bolton, M. Gamal El-Din, J.G.C. Veinot, Application of Engineered Si Nanoparticles in Light-Induced Advanced Oxidation Remediation of a Water-Borne Model Contaminant, ACS Nano. 10 (2016) 5405–5412. https://doi.org/10.1021/acsnano.6b01619.

[54] C.M. Gonzalez, M. Iqbal, M. Dasog, D.G. Piercey, R. Lockwood, T.M. Klapötke, J.G.C. Veinot, Detection of high-energy compounds using photoluminescent silicon nanocrystal paper based sensors, Nanoscale. 6 (2014) 2608–2612. https://doi.org/10.1039/C3NR06271F.

[55] C.-Y. Liu, Z.C. Holman, U.R. Kortshagen, Hybrid Solar Cells from P3HT and Silicon Nanocrystals, Nano Lett. 9 (2009) 449–452. https://doi.org/10.1021/nl8034338.

[56] D.P. Puzzo, E.J. Henderson, M.G. Helander, Z. Wang, G.A. Ozin, Z. Lu, Visible Colloidal Nanocrystal Silicon Light-Emitting Diode, Nano Lett. 11 (2011) 1585–1590. https://doi.org/10.1021/nl1044583.

[57] C.M. Hessel, E.J. Henderson, J.G.C. Veinot, An Investigation of the Formation and Growth of Oxide-Embedded Silicon Nanocrystals in Hydrogen Silsesquioxane-Derived Nanocomposites, J. Phys. Chem. C. 111 (2007) 6956–6961. https://doi.org/10.1021/jp070908c.

[58] C.M. Hessel, M.A. Summers, A. Meldrum, M. Malac, J.G.C. Veinot, Direct Patterning, Conformal Coating, and Erbium Doping of Luminescent nc-Si/SiO2 Thin Films from Solution Processable Hydrogen Silsesquioxane, Adv. Mater. 19 (2007) 3513–3516. https://doi.org/10.1002/adma.200700731.

[59] S.-M. Liu, Yang, S. Sato, K. Kimura, Enhanced Photoluminescence from Si Nano-organosols by Functionalization with Alkenes and Their Size Evolution, Chem. Mater. 18 (2006) 637–642. https://doi.org/10.1021/cm0519636.

[60] Y. Nishi, Study of silicon-silicon dioxide structure by electron spin resonance I, Jpn. J. Appl. Phys. 10 (1971) 52–62. https://doi.org/10.1143/JJAP.10.52.

[61] N. Fukata, C. Li, H. Morihiro, K. Murakami, M. Mitome, Y. Bando, Applied Physics A Hydrogenation effect on enhancement of photoluminescence of Er and Si nanocrystallites in Er-doped SiO 2 synthesized by laser ablation, Appl. Phys. A. 84 (2006) 395–401. https://doi.org/10.1007/s00339-006-3642-9.

[62] N. Fukata, J. Chen, T. Sekiguchi, S. Matsushita, T. Oshima, N. Uchida, K. Murakami, T. Tsurui, S. Ito, Phosphorus doping and hydrogen passivation of donors and defects in silicon nanowires synthesized by laser ablation, Appl. Phys. Lett. 90 (2007). https://doi.org/10.1063/1.2721377.

[63] N. Fukata, M. Mitome, Y. Bando, M. Seoka, S. Matsushita, K. Murakami, J. Chen, T. Sekiguchi, Codoping of boron and phosphorus in silicon nanowires synthesized by laser ablation, Appl. Phys. Lett. 93 (2008). https://doi.org/10.1063/1.3033226.

[64] R.J. Clark, M.K.M. Dang, J.G.C. Veinot, Exploration of Organic Acid Chain Length on Water-Soluble Silicon Quantum Dot Surfaces, Langmuir. 26 (2010) 15657–15664. https://doi.org/10.1021/la102983c.

[65] S.O. Kasap, Principles of Electronic Materials and Devices, Princ. Electron. Mater. Devices. (2017) 941–945. https://lib.hpu.edu.vn/handle/123456789/32461 (accessed December 16, 2022).

[66] D.A. Neaman, Semiconductor Physics and Devices, 4th edition, 2003. https://doi.org/10.1017/CBO9781107415324.004.

[67] S. Tongay, T. Schumann, A.F. Hebard, Graphite based Schottky diodes formed on Si, GaAs, and 4H-SiC substrates, Appl. Phys. Lett. 95 (2009) 222103. https://doi.org/10.1063/1.3268788.

[68] The physics and chemistry of the Schottky barrier height, Appl. Phys. Rev. 1 (2014) 011304. https://doi.org/10.1063/1.4858400.

[69] F.-C. Chiu, A Review on Conduction Mechanisms in Dielectric Films, Adv. Mater. Sci. Eng. 2014 (2014) 1–18. https://doi.org/10.1155/2014/578168.

[70] G. Wang, T.-W. Kim, T. Lee, W. Wang, M.A. Reed, Electronic Properties of Alkanethiol Molecular Junctions: Conduction Mechanisms, Metal–Molecule Contacts, and Inelastic Transport, in: Compr.

Nanosci. Technol., Elsevier, 2011: pp. 463–487. https://doi.org/10.1016/B978-0-12-374396-1.00138-0.

[71] S.M. Sze, K.K. Ng, Physics of Semiconductor Devices: Third Edition, 2006. https://doi.org/10.1002/9780470068328.

[72] Dielectric Phenomena in Solids, Elsevier, 2004. https://doi.org/10.1016/B978-0-12-396561-5.X5010-5.

[73] P.N. Murgatroyd, Theory of space-charge-limited current enhanced by Frenkel effect, J. Phys. D. Appl. Phys. 3 (1970) 308. https://doi.org/10.1088/0022-3727/3/2/308.

[74] A.K. Jehad, M. Yurddaskal, F. Gunes, C. Zafer, K. Kocabas, Investigation of graphene-based Schottky junction solar cell with heavy-doped silicon, J. Mater. Sci. Mater. Electron. 32 (2021) 28856–28869. https://doi.org/10.1007/s10854-021-07270-x.

[75] V. Shrotriya, G. Li, Y. Yao, C.W. Chu, Y. Yang, Transition metal oxides as the buffer layer for polymer photovoltaic cells, Appl. Phys. Lett. 88 (2006) 1–4. https://doi.org/10.1063/1.2174093.

[76] S. Murase, Y. Yang, Solution processed MoO 3 interfacial layer for organic photovoltaics prepared by a facile synthesis method, Adv. Mater. 24 (2012) 2459–2462. https://doi.org/10.1002/adma.201104771.

[77] H. You, Y. Dai, Z. Zhang, D. Ma, Improved performances of organic light-emitting diodes with metal oxide as anode buffer, J. Appl. Phys. 101 (2007) 1–4. https://doi.org/10.1063/1.2430511.

[78] J. Meyer, K. Zilberberg, T. Riedl, A. Kahn, Electronic structure of Vanadium pentoxide: An efficient hole injector for organic electronic materials, J. Appl. Phys. 110 (2011). https://doi.org/10.1063/1.3611392.

[79] A. Elschner, S. Kirchmeyer, W. Lovenich, U. Merker, K. Reuter, PEDOT, CRC Press, 2010. https://doi.org/10.1201/b10318.

[80] D. Alemu, H.-Y. Wei, K.-C. Ho, C.-W. Chu, Highly conductive PEDOT:PSS electrode by simple film treatment with methanol for ITO-free polymer solar cells, Energy Environ. Sci. 5 (2012) 9662. https://doi.org/10.1039/c2ee22595f.

[81] H. Do, M. Reinhard, H. Vogeler, A. Puetz, M.F.G. Klein, W. Schabel, A. Colsmann, U. Lemmer, Polymeric anodes from poly(3,4-ethylenedioxythiophene):poly(styrenesulfonate) for 3.5% efficient organic solar cells, Thin Solid Films. 517 (2009) 5900–5902. https://doi.org/10.1016/j.tsf.2009.03.212.

[82] S.-I. Na, S.-S. Kim, J. Jo, D.-Y. Kim, Efficient and Flexible ITO-Free Organic Solar Cells Using Highly Conductive Polymer Anodes, Adv. Mater. 20 (2008) 4061–4067. https://doi.org/10.1002/adma.200800338.

[83] A. Elschner, W. Lövenich, Solution-deposited PEDOT for transparent conductive applications, MRS Bull. 36 (2011) 794–798. https://doi.org/10.1557/mrs.2011.232.

[84] S. Avasthi, S. Lee, Y.L. Loo, J.C. Sturm, Role of majority and minority carrier barriers silicon/organic hybrid heterojunction solar cells, Adv. Mater. 23 (2011) 5762–5766. https://doi.org/10.1002/adma.201102712.

Chapter 2. Etching techniques and characterization methods

2.1 Etching techniques

There are two main ways to synthesize nanowires: the top-down and bottom-up strategies. The top-down method involves starting with a larger chunk of material, from which one removes material in a controlled manner until only the nanostructure(s) remain. Bottom-up methods, on the other hand, begin with the nanostructure's constituent parts—its atoms or molecules—and foster conditions in which those parts self-organize into the desired nanostructure. Using reactive ion etching (RIE) to remove nanowires from a bulk material while masking off sections of the surface with an etch-resistant substance is an example of top-down synthesis. Vapor-liquid-solid (VLS) growth, the most popular bottom-up technique, often employs gold as a catalyst.[1]. The advantages of the nanowire shape utilized in solar cells fabrication are, however, substantially lost when designing from the Bottom-up as the Au removal is challenging. Thus, top-down nanowire synthesis has been the emphasis of the work presented in this thesis. There are several different ways to form nanowires or fabricate them from the top down. In the next section, we will talk about how to make nanowire using a dry etching (for ordered arrays) and wet etching approaches.

2.1.1 Metal catalyzed electroless etching (MCEE)

More than 50 years ago, it was detailed how nanostructures might be formed by etching silicon in aqueous solutions of hydrofluoric acid combined with an oxidizing agent like HNO_3. [2] Stain etching (SE) is a frequent name for a specific type of Si etching that takes place at high dilution and within a narrow range of HF/oxidant ratios. Hydrogenated nano- or mesoporous silicon films with interference colors are typically produced by SE on top of an etched Si substrate. After 1990, this technique gained a lot of attention as a possible way to make luminescent Si films. This curiosity prompted additional research into standard SE once it was shown that its pace may be increased by the addition of a metal catalyst.[3] Li and Bohn subsequently investigated a less complex version of this MCEE to create porous Si.[4] Photo-luminescent nanostructures may be fabricated on p- and n-type wafers in the absence of an electrical potential.[4] As a result, MCEE became well known and was proposed for use in several areas of opto-electronics. In reference [5] and the references within, one may get a comprehensive review of the wide diversity of MCEE processes, their range of parameters, and their many applications.

In Figure 2.1[6], metal catalyst particles (Ag) placed to a Si surface serve as a prototypical example of the MCEE principle in action. Electron transmission from the valence band of silicon across the metal/Si contact replenishes the depleted electrons in the metal. In this way, electrical holes are implanted into the semiconductor immediately beneath the metal. Soon after, the holes spread to the semiconductor/electrolyte interface in the vicinity of the particle. The surrounding oxidized Si is then etched selectively by HF (mainly at the periphery and below a particle). For this reason, the

underetching causes the metal particles to "sink" into the Si, creating a vertical channel. Although no external current source is used, the entire process is electrochemical in nature. The process can be broken down into two synchronous reaction phases (the cathode reaction and the anode reaction), and it is identical to the mechanism of the deposition of copper nanoparticles on the surface of a silicon substrate.[7]

a. Cathode reaction:

$Ag^+ + e^- = Ag$

b. Anode reaction:

$Si + 2H_2O = SiO_2 + 4H^+ + 4e^-$

$SiO_2 + 6HF = SiF_6^{2-} + 2H_2O + 2H^+$

c. Overall reaction:

$Si + 6HF + 4Ag^+ = 4Ag + SiF_6^{2-} + 6H^+$

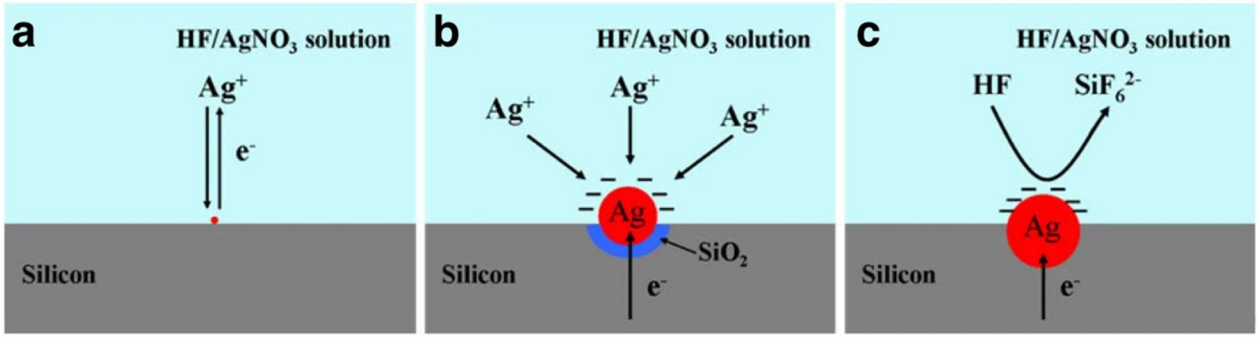

Figure 2.1 Deposition mechanism for Ag on Si substrate in dilute $HF/AgNO_3$ solution. (a) Nucleation of Ag forms. (b) the expansion of Ag particles and the oxidation of the Si substrate. (c) HF etching of the SiO_2 around it leaves tiny crevices in which Ag particles become trapped.

On the metal's surface, electrons are used catalytically to decrease the H_2O_2 (or other oxidant) present in the HF/H_2O_2 solution. Immersing a silicon substrate coated with silver nanoparticles in a solution of hydrogen peroxide and hydrofluoric acid ($HF\text{-}H_2O_2$) causes the silver nanoparticles to sink to the bottom (Figure 2.2) [6] because SiO_2 is continuously formed from the silicon contacting the silver nanoparticles via H_2O_2 as hole donor and oxidant and HF as solvent. Silica around the silver nanoparticles is continually oxidized and dissolved, etching the silicon substrate to create silicon nanowires.

a. Cathode reaction:

$H_2O_2 + 2H^+ \rightarrow 2H_2O + 2\ h^+$

b. Anode reaction:

$Si + 6HF + nh^{+} \rightarrow H_2SiF_6 + nH^{+} + [n/2]H_2$

c. Overall reaction:

$Si + 6HF + n/2H_2O_2 \rightarrow H_2SiF_6 + nH_2O + [2 - n/2]H_2$

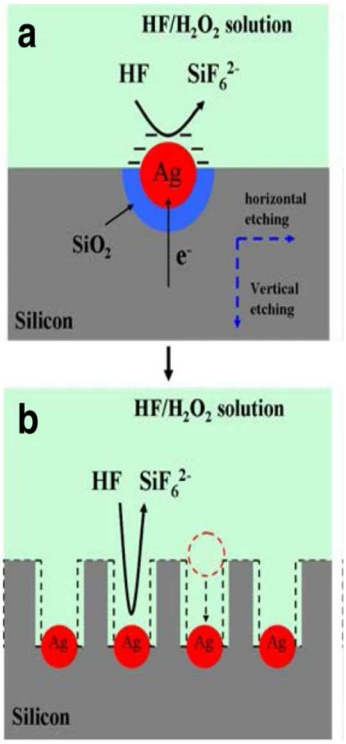

Figure 2.2 Schematic diagram of Ag nanoparticle-assisted etching with H_2O_2.

However, the size, shape, spatial distribution, and sort of metal particles have a significant impact on the etching current distribution close to the particles, and hence on the form of the channel. To etch in a vertical orientation, silver nanoparticles on the silicon surface may accelerate the etching reaction around and below the silicon substrate to generate pits, where they may subsequently sink due to gravity. Increases in the concentration of hydrogen peroxide (H_2O_2), which serves as a hole donor and oxidant during etching, cause the silicon surrounding the Ag nanoparticles to oxidize at a faster rate, hence increasing the silicon's horizontal etching rate. [6]

2.1.2 Nanoimprint lithography (NIL)

To create SiNWs and other nanostructures, nanoimprint lithography, a top-down RIE manufacturing technique, employs molds to imprint the pattern needed for the procedure.[8] This technique is attractive because molds can be built with the precise configuration requested and reused several times to form comparable SiNWs, resulting in a high level of control and repeatability, which is typically crucial for industrial applications and reproducible studies.[9] This mold allows for precise manipulation of the cross-sectional size and form of SiNWs, as well as their placement in a variety of predetermined arrays.

After the SiNWs have been formed by the etching process, their length and shape can be modified as desired. The combination of nanoimprint lithography with SiNWs allows for a wide range of customization and extensive scaling. SiNWs are fairly pure Si structures identical to the underlying substrate after the etching mask is removed. The Si industry is interested in nanoimprint lithography, a relatively new technique that has not yet become extensively employed.

These SiNWs have been employed in the past by the Fukata group laboratory in p-n junction solar cells.[10] The procedure is depicted in Figure 2.3.[11] Nanoimprint lithography SiNWs are formed by first preparing a Si substrate. Because of how surface sensitive the imprint and etching process is, the wafer surface must be spotless. A thin coating of photoresist is spin-coated onto the wafer's surface. Patterns must be produced in the photoresist by the impression mold very close to the Si surface, therefore its uniformity and the thickness formed by spin-coating are crucial. Finally, a quartz mold is forced into the photoresist while the Si wafer is in a vacuum. High-pressure stamping of a quartz mold containing nanowires of the desired size and arrangement into photoresist results in a pattern of holes that is mirror-imaged in the mold. During the pressing process, the photoresist is fluid and flows around the mold to create the imprint. During the imprint pressing process, the photoresist is cured by passing ultraviolet light through a clear quartz mold. The photoresist keeps the pattern even after being removed. Due to the risk of damaging the Si surface if the impression were to press all the way to it, the imprint's holes are lined with a thin layer of resist. For mask deposition, this thin coating must be peeled off afterwards. The photoresist is removed off the wafers one layer at a time using a plasma etcher until the resist is gone from the bottom of the holes but not from the sides. After the wafers have been imprinted, a mask material is put on top of them. Masks matching to the original quartz mold nanowires are left on the Si wafer surface when the photoresist is dissolved in solution, leaving just the mask in contact with the Si surface. When the masks are in place, the samples are ready for reactive ion etching. The Si around the masks will be etched vertically and removed using Bosch etching with SF_6 and C_4F_8 plasma. Under optimal circumstances, vertical etching produces straight-walled SiNWs beneath the masks and a roughened, though normally flat, surface in between the SiNWs. By repeating the etching process, material may be removed and the SiNWs can be grown to greater lengths. Finally, the mask material is stripped away, and the wafer is cleaned, leaving only the Si substrate with the SiNWs sticking out. Nanoimprint lithography's resolution is unaffected by the backscattering and interference of resist thanks to this method, which does not need the employment of intense beams. The method demonstrates more of a physical fabrication than a chemical one. It is possible to mass produce NW arrays at a reasonable cost using the nanoimprint lithography technique.

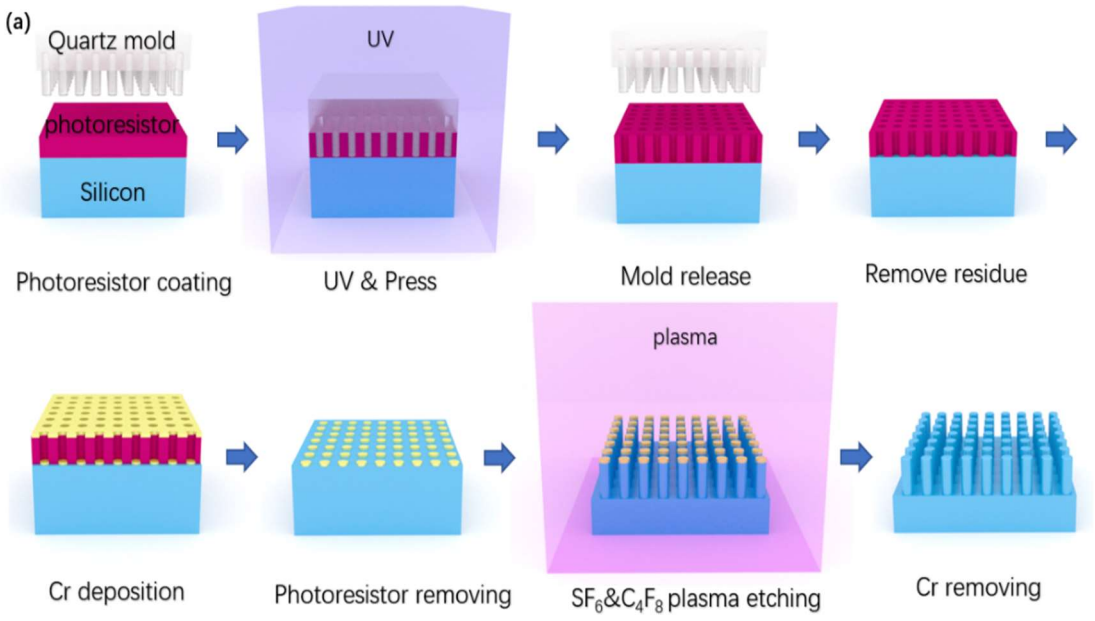

Figure 2.3 Schematic diagram of the steps involved in the construction of an array of SiNWs using NIL.

2.2 Processing equipment

2.2.1 Sputtering system

The electronic industry frequently uses sputtering, a form of physical vapor deposition, to manufacture thin coatings. As a result of its usefulness, it was put to use here in the deposition of the metal electrodes. Metal atoms are transferred from a metal target to the surface of a sample facing the target using energetic ions from an inert gas, as shown in Figure 2.4 (a).[12] Typically, inert gas molecules (Ar gas in this experiment) ionize from electron collisions when a high voltage is applied between the metal target and the chamber. It is usual practice to employ a magnetron to concentrate electrons close to the target's surface, where they can form a dense plasma. Accelerating toward the negative charge below the target, the ionized Ar atoms smash against the metal particles that make up the target. Neutral metal atoms are ejected from the target and some make it into the sample as a result of the impact. In a direct hit, high-energy metal ions might deposit at the impact point on the sample surface. In order for the metal ions to deposit on all surfaces, the sample must be rotated so that they have a direct line of sight to each surface at some point in the rotation. However, some metal atoms lose energy in collisions with the gas, leading them to travel more randomly on their way to the surface. This causes extremely thin depositions everywhere, not only where there is a direct line of sight to the metal target. Applications that need sharp mask cut-offs might be hindered by this deposition phenomena. While thermal evaporation may also be employed, unlike CVD, it will not result in uniformly thin layers

across all of the SiNW surfaces. The benefits of sputtering include fast deposition, high adherence to the surface, and little sample heating.

In this study, deposition of Ag and Ti metal electrodes was carried out in a conventional laboratory setting utilizing an Anelva L-3325-FH sputtering equipment (Figure 2.4 (b)). Room temperature was maintained, and rotation was applied during the sputtering process, with the samples. In both the DC and RF systems utilized for Ag and Ti depositions, respectively, the Ar gas pressure was set to 2 x 10^{-1} Pa.

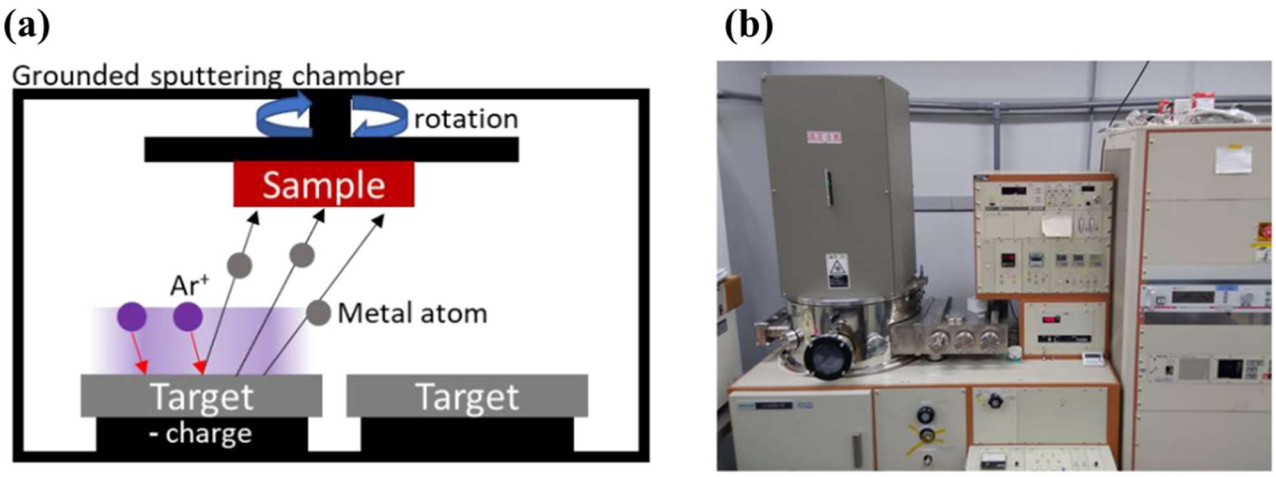

Figure 2.4 (a) A pictorial representation of the sputtering operation. Thin layer deposition is achieved across the whole exposed surface by the angular impact of ejected metal atoms striking the sample as it rotates. (b) Picture of the Anelva L-3325-FH sputtering system.

2.2.2 Rapid thermal annealing (RTA)

As can be seen in Figure 2.5, rapid thermal annealing (RTA) treatment is a procedure that may quickly heat the sample at a very high temperature within a short amount of time. The temperature may be adjusted between 150 and 1200 degrees Celsius.

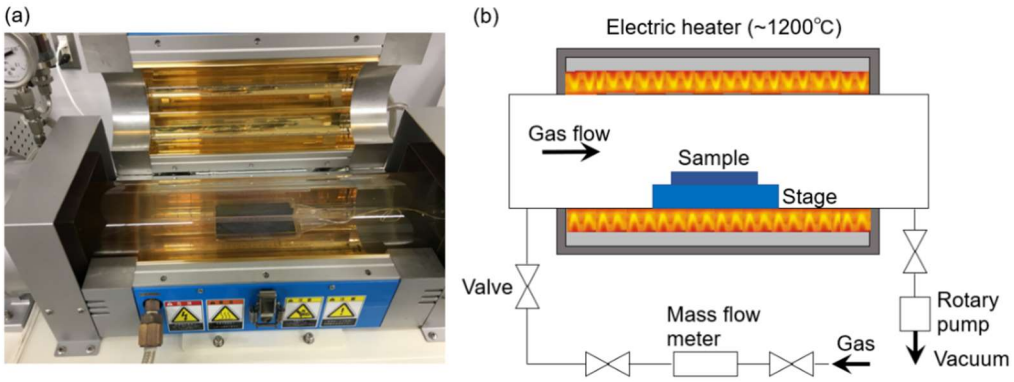

Figure 2.5 (a) equipment and (b) schematic of the RTA system

There is a maximum of 200 °C/s that may be reached in the temperature ramping process. Dopant activation and defect density reduction in NWs both need high-temperature annealing. When it comes to activation energies, RTA systems can offer a broad variety of time and temperature possibilities. Interdiffusion is also prevented by the rapid cooling that follows the RTA annealing process.

In this thesis, RTA is used to anneal vanadium oxides films with three different ambient atmospheres, under vacuum and with nitrogen and oxygen gas flow of 200 sccm using the machine depicted in Figure 2.5 (a).

2.3 Characterization techniques

2.3.1 Electron microscopy: (SEM and TEM)

The next round of studies relied heavily on electron microscopy to determine the atomic-level structure of the materials. Due to its great depth of focus and compatibility with 3D structures, scanning electron microscopy (SEM) was especially depended upon, while tunneling electron microscopy (TEM) played a more supporting role. In order to evaluate the results, it is helpful to have a brief overview of the mechanics involved in electron microscopy. To generate pictures of solid objects, both SEM and TEM employ focused beams of powerful electrons as a probe. While both methods of characterization employ electrons for imaging, their other components and processes are quite different. As seen in Figure 2.6, SEM works by sweeping a focused electron beam back and forth over a sample surface. This raster approach slows down SEM and lowers its resolution, but it also helps SEM produce intuitive pictures. Electromagnetic lenses are used to concentrate the beam of an electron source into a tiny spot on the sample; the resolution of the microscope depends in part on the size of this spot. In order to create the raster pattern, the objective lenses are used to shift the beam's focal point across the surface. As the electrons clash with the sample, some of them will scatter off the surface and into the detector below. Each pixel in a picture is the result of the detector recording the strength of signals acquired when the probe was focused on a specific location. To account for the varying brightness of these spots caused by the substrate's influence on the scattered electrons, the detector creates a "beam raster" that assigns pixels to each spot. Imaging often makes use of secondary electrons. Although the higher-energy, backscattered electrons created by elastic scattering are helpful for phase identification. The electron beam collides with an atom in the sample, exciting and ejecting an electron. This process, known as inelastic scattering, produces secondary electrons. Since the high-energy electron beam can take a curved course through the material, secondary electrons can emerge from as far as 550 nm away from the incident beam. Although resolution suffers, additional sample data is gained in exchange. Since secondary electrons are less energetic than the electron beam, a Faraday cage is utilized to funnel them towards the detector and gather many signals. Since the collector is tilted with respect to the surface of

the sample, it is more effective at gathering electrons that are dispersed in one direction than in the other.

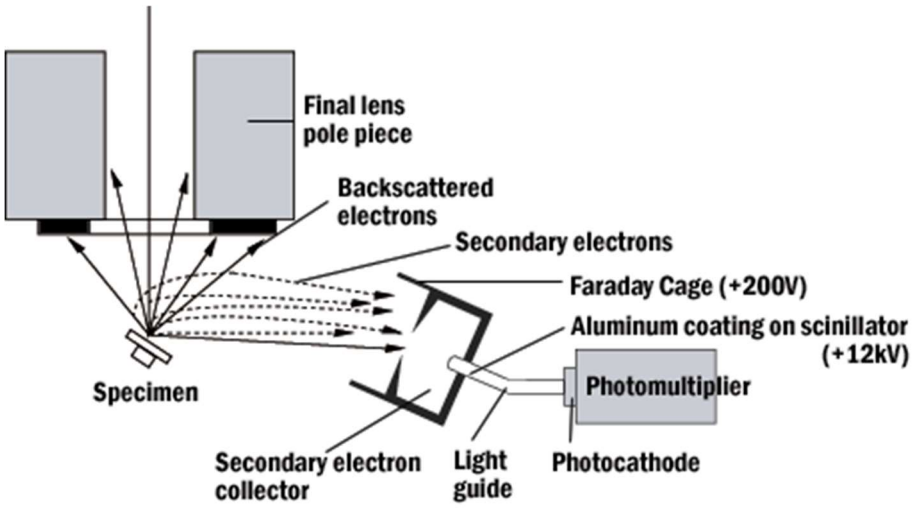

Figure 2.6 Illustration of a simple SEM setup. Secondary electrons are created in the interaction zone when an electron beam is focused and raster-scanned across a sample's surface; these electrons are then attracted to the Faraday cage and detected.

[Source: https://cmrf.research.uiowa.edu/scanning-electron-microscopy]

Since electrons move randomly inside the sample, they are more likely to escape from edges than from flat surfaces, which plays a significant role in creating the picture. This causes the edges of the structures to stand out, particularly at high magnification and for thin nanostructures. The electrons' interactions with matter vary from one substance to another due to differences in density and electron structure. There may be some compositional distinction here, however secondary electrons may not pick it up as well. The electrons in the electron beam will clump together in the sample, causing a wide range of side effects. When these electrons find a path to move through, they tend to disperse in places outside the picture that are made of conductive materials. As a result, conductors stand out more clearly and seem much darker. Electrons will gather into high charge concentrations if the substance is insulative or if a conductive material is separated. As a result, scattering will rise and the image's brightness will improve. Insulative pictures are notoriously challenging to capture, yet they provide useful qualitative data on conductivity. Furthermore, charging the sample can induce streaks owing to delayed ejections, charge buildup and discharge, resulting in image jumps, and can cause the material to change state or move, potentially harming the sample. Last but not least, because the raster process is sluggish, the sample could shift or migrate during the procedure, distorting the final image. While longer scans provide sharper pictures, they distort scale, thus shorter scans are better for precise measurements. The consequences of the parameters of the electron beam are another area of weakness. By changing the acceleration voltage, the power of the electron beam may be modified. Brighter electron

beams from higher voltages mean a smaller probe and better resolution. Although greater acceleration voltages are often preferred, imaging surface features or very thin materials might be challenging due to the electrons' increased penetration depth. In addition, there is a greater possibility of harming the sample, therefore the voltage needs to be tuned based on the sample's constituent parts. The amount of electrons used to form the picture may be increased by adjusting the probe's current. In order to create contrast in the image, the current must be somewhat strong. Noise and charging effects can be amplified by currents that are too high, therefore this is another factor to optimize. The NIMS Foundry's Hitachi field emission SEM SU8000S were utilized for the thesis experiments (Figure 2.7). Unless otherwise noted, images were generally captured at 5-10 keV. A probe current of around 10 mA and a separation between the probe and the sample of about 8 mm were utilized.

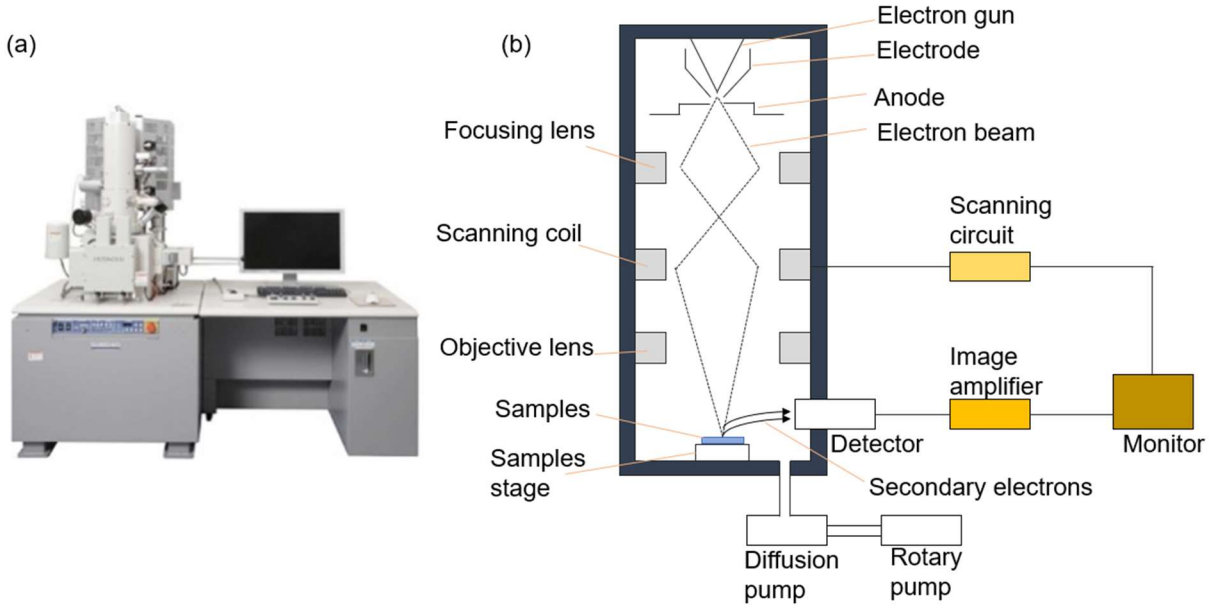

Figure 2.7 (a) equipment and (b) schematic of SEM. [Source: http://www.hitachi-hightech.com]

By sending an electron beam through a material, transmission electron microscopy (TEM) provides pictures with atomic-scale resolution thanks to the electrons' shorter wavelength (Figure 2.8). As with SEM, TEM uses electromagnetic lenses to focus an electron beam, but in TEM, the beam is swept across the sample rather being concentrated in a single location. At the opposite end of the sample, we may collect the electrons that made it through. When electrons flow through a sample, the atoms in the sample scatter them, creating a dark contrast. The density, thickness, and composition of the sample all have a role in the scattering effect. Electron beams can be diffracted by crystalline materials, which have repeating crystal planes. Thus, TEM may be used to investigate anything from the macroscopic form and distribution of a material to its atomic crystal structure. However, there are various limitations on sample preparation that must be met for good imaging. Especially when trying to collect crystal diffraction data, the sample must be very thin since some of the beam must pass through it to gain any information at all. Small, thin samples can be used, or a larger one can be chopped or ground down to

layer size. The sample is then suspended on a TEM grid made of carbon, copper, or some other tiny structure. In the case of quantum dots sample, it can dispersed in a suitable solvent then drop-casted on the TEM grid. However, 3D structures at the upper nano- and micro-scales might be more challenging to employ with TEM due to the instrument's working principals and sample compatibility requirements. These studies made use of a JEOL JEM-2100 200kV-TEM system equipped with carbon and copper grids and controlled by NIMS Foundry professors.

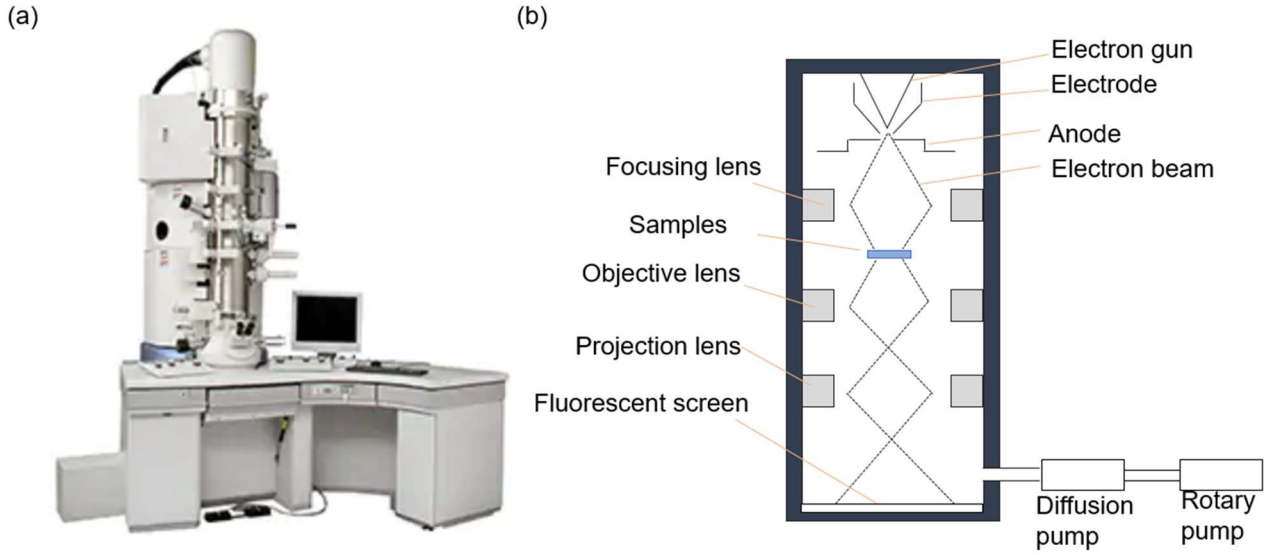

Figure 2.8 (a) equipment and (b) schematic of TEM. [Source: http://www.hitachi-hightech.com]

2.3.2 Energy Dispersive X-ray Spectroscopy

Sometimes it was necessary to look at where and how often certain characteristics were present in the research. To accomplish this, the characterization method of Energy Dispersive X-ray Spectroscopy (EDS) was applied. Ionization occurs when high-energy particles strike an atom, causing an electron in one of its inner shells to become so excited that it escapes. A photon is produced whenever an electron from a higher energy orbital falls to a lower energy orbital. Either this photon will escape as a distinctive x-ray or it will knock off an electron whose spectrum may be studied using Auger spectroscopy. There is a limited range of x-ray energies attainable due to the discrete nature of electron shell energies. Because electrons from various outer shells can drop to specific different inner shells, a single element can emit many distinct x-rays. Energy analysis of these X-rays can be used to identify the element being studied because various elements have varying electron shell energies. The electron shell energies measured by x-ray spectroscopy are independent of bonding or crystal structure, making the analysis straightforward. An X-ray fluorescence spectrometer (XRF) uses photons to dislodge the electron from an atom, while an electron microscope uses electrons. The electron source can be an electron microscope, which is very handy, and the electron beam can be accelerated to very high energies in either a scanning electron microscope (SEM) or transmission electron microscopy (TEM) system, resulting in the distinctive X-rays. The interaction zone that is defined is deeper than that for the

secondary electrons utilized in SEM imaging because these high-energy electrons may penetrate deeply into the surface whereas the X-rays can readily escape. The EDS method uses a technique called energy dispersive spectroscopy to analyze the X-rays it generates. A second detector collects the resultant X-rays, converting them into an amount of electron-hole pairs proportional to the X-ray energy. In an X-ray energy vs intensity plot, the energy of each X-ray is displayed against its intensity. Analysis of a single point's composition is possible, as is analysis of a line or a square region using a concentrated electron beam. Assuming that the X-rays gathered at each location can be positively identified, a rough map of the area's elemental distributions may be constructed.

Each element emits a unique set of distinctive X-rays that can be reliably recognized, allowing for the complete characterization of the resulting spectrum. If the electron was ejected from the first, second, or third shell, the peak will have those respective prefixes appended to it: K, L, or M. The peak is categorized as α, β, γ, etc. and 1, 2, 3, etc. based on the shell and orbital levels of the electron filling the vacancy. Because to selection restrictions, only a subset of orbital transitions are conceivable for each element, leading to a small number of peaks; furthermore, not all peaks are collectable due to the low energy of the SEM or TEM beam. The intensity of the gathered peaks may be used to calculate the abundance of each element in comparison to those already in the database. This is because the number of atoms in a sample increases the quantity of X-rays emitted at a given energy. In order to determine the location of peaks, the energy of the X-rays is compared to the energies used for characterizing objects. There is often overlap between peaks, particularly for elements with a high atomic number due to the random distribution of their many distinctive X-rays over the spectrum. Therefore, knowing the composition in advance is necessary, and peak position alone is not sufficient for identification. When using an automated technique, such as EDS mapping, this peak overlap might be a simple cause of inaccuracy. The poor fluorescence yield and limited number of peaks make it challenging to detect elements with low atomic numbers. Elements below oxygen are notoriously hard to identify and measure, while those below Be are impossible to detect at all. Moreover, EDS is a useful instrument for determining elemental composition, although it is prone to large amounts of inaccuracy. Variances in peak intensities used to quantify composition can be caused by a number of factors, including the influence of background signals, differences in how each element absorbs electrons and X-rays, differences in X-ray fluorescence, and the elements' locations in the sample. This means that EDS quantifications should be treated as approximations within a margin of error of a few percent at most. EDS can't be used to identify or quantify trace levels of elements below 1 or 2 percent since the quantity of distinctive X-rays collected is so little relative to background signals.

Samples were analyzed using the Hitachi SU8000S SEM at NIMS Foundry, which have energy dispersive x-ray spectroscopes connected.

2.3.3 X-ray diffraction (XRD)

X-ray diffraction equipment was utilized to characterize the crystal structure of annealed metal oxides films. If a substance contains regular crystal planes, then multiple incident X-rays may diffract so that the refracted X-rays are in-phase and suffer constructive interference depending on the distance between the crystal planes and the angle of the X-rays, in accordance with Bragg's Law:

$$n\lambda = 2dsin\theta$$

where n is an integer, λ is the wavelength of the X-rays being used, d is the distance between the parallel crystal planes, and θ is the incidence angle, as shown in Figure 2.9. The diffracted X-rays will only constructively interact at particular angles if the wavelength of the X-rays and d are maintained constant. Since different crystalline materials have different d values on their various parallel crystal planes, the X-rays will constructively interfere with one another at distinct angles for each. This is measured using XRD, which involves irradiating a sample with X-rays of the same wavelength at an angle and then collecting the resulting X-rays, which have been constructively interfered. Diffraction patterns in single crystal samples are only produced in single reciprocal lattice places that depend on the crystal's orientation, and these spots might be hard to locate if the crystal orientation is unknown. Due to the abundance of parallel crystal planes in polycrystalline materials, data on all crystal planes may be conveniently gathered by simply moving the beam and detector along a line.

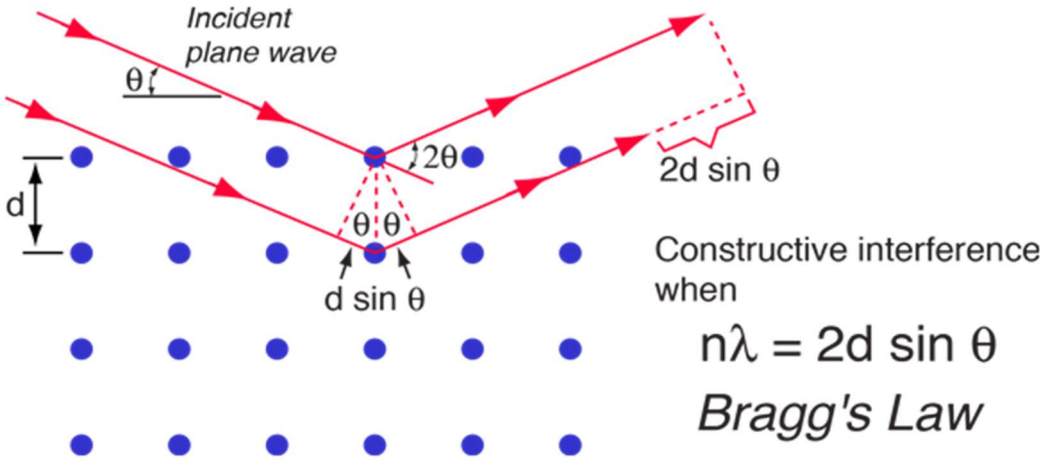

Figure 2.9 Bragg's law parameters and atomic crystal planes are shown in an illustration of X-ray diffraction.

The unique peaks measured by XRD may be used to uniquely identify the crystalline phases of a wide variety of materials. XRD may be used to gather data on a material's crystal identity, microstructure (such as crystallite size and preferred orientations), thin film widths, lattice spacing changes owing to processing techniques or residual stress, phase quantification, and so on.[13] The XRD peaks of tiny crystal grains, for instance, are often wider and shorter. This is due to the fact that imperfect destructive interference for slightly deviated X-rays is produced by the smaller number of parallel crystal surfaces

that provide constructive interference at the right angle. Because of the different angles at which the diverted X-rays are gathered, the peak broadens. Since stress shortens or tenses bond distances, XRD may also detect residual stress. As a result, non-uniform stress will cause the peaks to enlarge, whereas uniform strain will cause a change in their location.

In order to prepare a specimen for XRD, the material must have a sufficiently repeating crystal structure, a flat surface, a wide enough area to refract enough X-rays, and a somewhat thick thickness, as X-rays have a considerable penetration depth. The last issue may be solved for thin films by utilizing beam grazing angles to ensure that the beam traverses as much of the sample horizontally as feasible. The following study used a PANalytical X'Pert thin film X-ray diffractometer to examine polycrystalline thin film samples that satisfied the specifications for specimens. The X-ray source was Cu Kα radiation, and the beam was positioned at a 5^{o} grazing incidence angle while the detector was rotated. The location of the samples was modified so that the beam traversed the appropriate thin film layer.

2.3.4 X-ray photoelectron spectroscopy (XPS)

The ability of X-ray photoelectron spectroscopy (XPS) to clarify chemical identity, composition, and bonding structure without bulk interference has given it a central role in surface research. The method relies on calculating the amount of energy lost by core electrons as they are expelled due to x-ray irradiation. It is therefore possible to ascribe electronic transitions to individual components and bonding arrangements.

X-ray sources like Mg Kα and Al Kα are employed in XPS analysis. An atom in the solid absorbs the X-ray if its photon energy is greater than its binding energy, leading to photoemission of electrons from the core and valence levels. A spectrometer measures the strength of the released electrons to create a spectrum. An element's binding energy can be used as a fingerprint characteristic to determine the energy level at which its photoemitted electrons are emitted.

The photon energy affects the kinetic energy of the released electrons, and the following equation summarize the fundamental relationship:

$$h\nu = KE + BE + \phi$$

where KE is the kinetic energy of the ejected electron, BE is its binding energy, φ is the spectrometer work function, and hv is the energy of the incident photon as determined by the incident x-rays. The ionized atom must relax in order for a photoelectron to be released. This is accomplished by the ejection of a secondary electron known as an Auger electron, which is created during the XPS process. Auger peaks can provide valuable information about associated atoms even if they have the potential to interfere with photoelectronic peaks. When the surface is exposed to x-rays, photoelectrons are expelled from it with kinetic energies based on their orbitals of origin. The resultant signal (and lineshape) may be utilized to establish the elemental composition and bond structure of the surface since an element's

orbital fingerprint identifies its chemical state. XPS is particularly well-suited to studying surfaces since electrons have a shallow escape depth (<15 nm),therefore XPS is said to as a surface-sensitive technology. The measuring environment is limited by the mean free path of the electrons. Ultra-high vacuum (UHV) conditions are typically used in XPS operations to minimize energy loss due to collisions. This prevents the surface from being covered with gas-phase molecules that have been absorbed. Over the past decade, advances in electron optics have made near ambient pressure conditions and, by extension, in situ XPS measurements possible by shortening the distance electrons must travel to reach the analyzer input.

The electronic state and amount of elements were determined by X-ray photoelectron spectroscopy (XPS; Quantum-2000 ULVAC-PHI) investigation in this study. Monochromatic Al Kα radiation (hν=1486.6 eV) at 200 W and 45° take off angle was used for the XPS experiments. Following the measurement of the survey spectrum, high resolution measurements of the components of interest were carried out. High-resolution spectra of each element were fitted with curves to learn about their electronic states and conduct quantitative analyses. An element's electronic state can be identified by analyzing the chemical change in the energy locations of its associated peaks. Bonding alters the binding energy position of an atom relative to its elemental state by increasing or decreasing its valence electron density. Electrostatic charge in the positive direction is noticed while working with insulating materials (VO_x) due to photoemission from these samples. When charged, the peak moves to the side with a higher binding energy. It was determined that a correction to the spectra was necessary with regard to the C *1s* peak at 284,6 eV. Following a Shirley background removal, spectra were deconvolved using a Gaussian-Lorentzian peak profile.

2.3.5 UV-Vis-NIR

UV-Vis-NIR spectroscopy was used to analyze the materials in this study since their optical characteristics were crucial for the solar cell application. It is possible to learn about a material's electrical characteristics by studying its optical qualities, which are dependent on the way in which structures reflect and absorb light and are in turn related to interactions between photons and electrons in the material. Vibrational spectroscopy and X-ray spectroscopy have proven that when electromagnetic radiation is shone upon a material, numerous distinct interactions between the photons and material atoms can occur. A UV-Vis-NIR spectrometer adds up all of these interactions by studying what occurs when light of varying energy is shone on a sample. The total amount of incident light (I) is equal to the sum of the light that is reflected from the material (R), transmitted through the material (T), absorbed by the material (A), and scattered on the surface or inside the material (S). A UV-Vis spectrometer instrument can be used to record these varying results. Transmission may be measured by recording the light that travels through a thin, transparent, or liquid-based sample. Transmission through the thick, opaque materials utilized in these tests is believed to be minimal, leading to the equation I=(R)I+(A)I+(S)I. Collecting the reflected and scattered light together reduces

the system to I=(R+S)I+(A)I since both processes deflect light away from an observer, although in opposite directions. Most of the light that reflects and scatters in all directions may be gathered using an integration sphere, and then compared to the intensity of I to derive (R+S). It is considered that any light that is not captured is absorbed (A). By manipulating the incident light wavelength with a diffraction grating, it is possible to plot the intensity of the desired factor versus the light wavelength, revealing the dependency of these components on light wavelength. The subsequent studies analyzed the materials' % reflectance at wavelengths between 300 and 1300 nm using a Jasco V-670 UV-Vis-NIR spectrophotometer equipped with an integrating sphere attachment.

2.3.6 Fluorescence spectroscopy

Fluorescence spectroscopy is a characterization technique used to measure photoluminescence (PL) spectra of quantum dots. When electrons in semiconductor quantum dots relax from an excited to a ground state, a phenomenon known as photoluminescence (PL) occurs (electron-hole radiative recombination). This procedure is hindered by the presence of non-radiative recombination, which arises from a number of sources (most notably lattice defects, Auger recombination, and surface recombination). Since non-radiative recombination results in energy loss, it is crucial to maximize the radiative recombination process while minimizing the non-radiative recombination process.

The photoluminescence (PL) spectrum represents the photoluminescence (PL) of a quantum dot solution versus frequency (or wavelength). The photoluminescence (PL) quantum yield (PLQY), full width at half maximum (FWHM), and emission peak wavelength (λ_{max}) are all significant optical features. The quantum efficiency of a QD is measured by its photoluminescence quantum yield (PLQY), which is the ratio of photons emitted to those absorbed. Maximum light harvesting and lowest energy losses may be achieved with a PLQY close to 100%, which is indicative of high crystallinity, few defects, and a slow non-radiative recombination rate. It's possible that a device's best performance corresponds to its highest possible PLQY (i.e. high external quantum efficiency in optoelectronics). The maximum wavelength at which an emission occurs is denoted by λ_{max}. Since monodispersed quantum dots exhibit a gaussian distribution, it is essential to achieve a certain λ_{max} value to maximize their potential applications. The FWHM is the half-intensity width of the emission or excitonic peaks. Applications that rely on accurate color reproduction, including color displays and LEDs, benefit greatly from a narrower emission FWHM (<50 nm). The synthesized quantum dots must have a limited size distribution and few crystalline imperfections that can produce sub-bandgaps in order to achieve narrow emission.

The following study used fluorescence spectrophotometer (Jasco FP-8500) at room temperature with excitation wavelengths between 200 and 400 nm.

2.3.7 Time-resolved PL decay (TRPL)

Time-resolved photoluminescence decay spectroscopy (TRPL) is another method for characterizing PL emissions. The technique of TRPL is an extension of fluorescence spectroscopy that involves the

stimulation of quantum dots with a short laser pulse and the subsequent measurement of their photoluminescence using a detector. The PL lifetime of a luminous particle might be calculated by fitting the TRPL curve. It is possible to calculate the PL lifetime (τ) as the inverse of the product of the total recombination rate constants.

The decay rate (Γ) of a quantum dot may be calculated using data from both PLQY and the TRPL measurement of PL lifetime:

$$\text{Decay rate } (\Gamma) = \frac{\text{PLQY}}{\tau}$$

It is possible that the quality of the crystal structure and the dynamics of the excited state of a QD system can be gleaned from the variation in the value of Γ as a result of various synthetic optimizations.

2.3.8 Photovoltaic characterization

Analyzing the electrical and photovoltaic characteristics of solar cell samples was possible with the help of in-house equipment such solar simulator, sample stage, and source meter. The sample is illuminated by a solar simulator whose output is an approximation of the solar spectrum of our sun. Despite the solar simulator's light spectrum not being a precise match for the sun's, the arrangement should be consistent with most other solar cell reports. Once the sample is in place on the gold-coated stage, a front contact probe connects it to the source meter. To begin, a dark I-V curve is created by sweeping the voltage from reverse bias to forward bias while measuring the current with a source meter, which is used to examine the diode characteristics of the sample. In order to determine the photovoltaic qualities, an illuminated *I*-V curve is generated by sweeping the voltage while monitoring the current while the device is lighted.[14] Since carriers are being produced by photogeneration, the current profile should now be a superposition of the diode profile, indicating a photovoltaic effect. Given the significance of sample size, we calculate the current density *J* by dividing the measured values by the sample's surface area, and then we display the results as a function of voltage, V. The obtained data is then automatically processed to determine the fundamental characteristics of the solar cells. At the points where the axes cross, we may get precise readings of the open circuit voltage V_{OC} and the short circuit current density J_{SC}.

Maximum power, given the observed data, is determined by plotting the data as power (I•V) vs voltage and locating the maximum where:

$$\frac{d(JV)}{dV} = 0$$

The fill factor FF is then calculated using the maximum power voltage and current, V_m and I_m, respectively:

$$FF = \frac{J_m V_m}{J_{sc} V_{oc}}$$

The power conversion efficiency (abbreviated PCE) of solar cells can be calculated as follow:

$$PCE = \frac{J_{sc} V_{oc} FF}{HA}$$

where H is the power density of the light and A is the receiving area. The PCE simply represents the proportion of power that the cell can give in comparison to the amount of light power displayed on it. The following tests were conducted using a 100 mW cm^{-2} power density and an Asahi Spectra solar simulator illuminated with AM1.5G light. Sharp single-crystalline silicon solar cell (BS-500) was used for the calibration. The performance of the solar cells was measured with the use of a Keithley 2400 source meter. All the readings were taken in ambient air at room temperature.

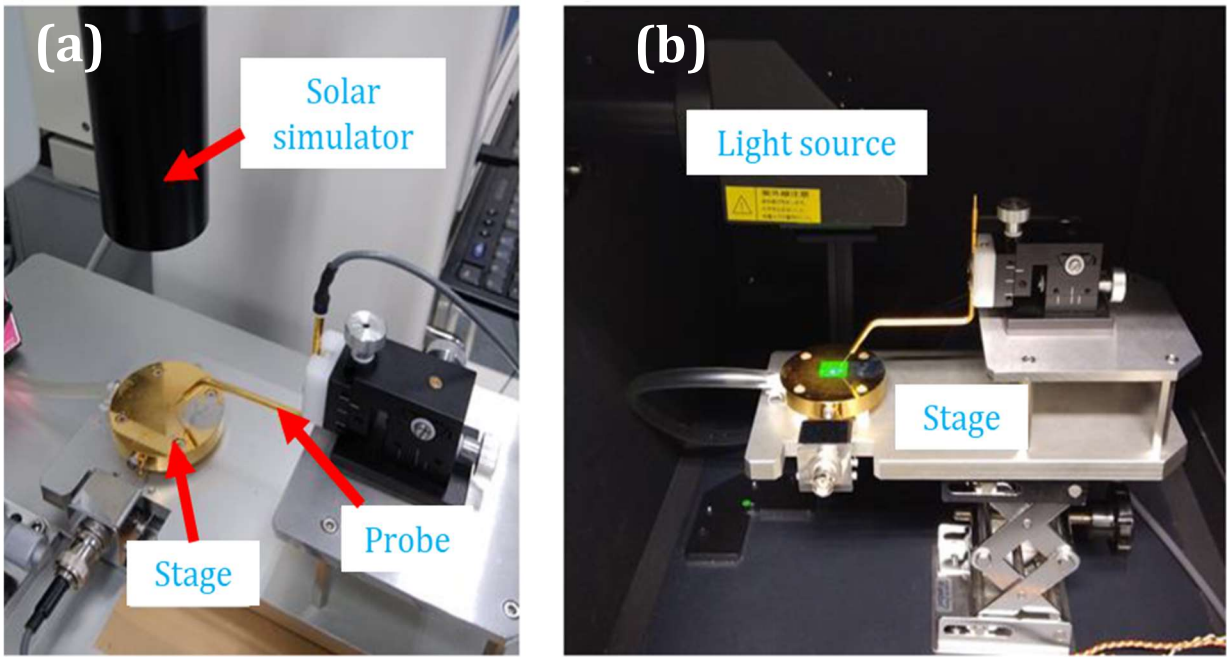

Figure 2.10 (a) Indoor photovoltaic and solar energy testing apparatus. (b) View of the inside of the Bunkoukeiki EQE monitoring facility.

In addition, the devices' responses to various wavelengths of light were quantified by spectral response tests. The ratio of electrons created and collected for every incident photon is the external quantum efficiency (EQE) of a solar cell. The EQE spectrum is created by varying the incident light's wavelength and measuring the resulting current. This tells us whether or not the sample is at a spot where you can collect the carriers that are created when the light is absorbed at various frequencies. In addition to revealing the amount of carrier loss, the EQE may also reveal how well a cell absorbs light. Since different wavelengths of light are absorbed by the cell at varying depths, EQE may be thought of as a depth-selective probe. Higher losses might occur at certain depths if the EQE decreases at certain wavelengths. White light is sent through a diffraction grating to divide the light and a portion of the light

is then directed toward the sample for the EQE measurement. At each wavelength of the incoming light, the resultant photocurrent is measured, converted to an EQE percentage, and displayed versus light's wavelength. The next studies replicated the sun simulator tests by measuring EQE using Bunkoukeiki BQE-100F measurement instrument. All the measurements were taken in ambient air at room temperature.

2.4 References

[1] X. Zhang, W. Jevasuwan, K.C. Pradel, T. Subramani, T. Takei, N. Fukata, Hole gas accumulation in Si/Ge core-shell and Si/Ge/Si core-double shell nanowires †, Nanoscale. 10 (2018) 21062. https://doi.org/10.1039/c8nr05590d.

[2] R.J. Archer, Stain films on silicon, J. Phys. Chem. Solids. 14 (1960) 104–110. https://doi.org/10.1016/0022-3697(60)90215-8.

[3] D. Dimova-Malinovska, M. Sendova-Vassileva, N. Tzenov, M. Kamenova, Preparation of thin porous silicon layers by stain etching, Thin Solid Films. 297 (1997) 9–12. https://doi.org/10.1016/S0040-6090(96)09434-5.

[4] X. Li, P.W. Bohn, Metal-assisted chemical etching in HF/H2O2 produces porous silicon, Appl. Phys. Lett. 77 (2000) 2572–2574. https://doi.org/10.1063/1.1319191.

[5] Z. Huang, N. Geyer, P. Werner, J. de Boor, U. Gösele, Metal-Assisted Chemical Etching of Silicon: A Review, Adv. Mater. 23 (2011) 285–308. https://doi.org/10.1002/adma.201001784.

[6] Y. Liu, G. Ji, J. Wang, X. Liang, Z. Zuo, Y. Shi, Fabrication and photocatalytic properties of silicon nanowires by metal-assisted chemical etching: effect of H2O2 concentration, Nanoscale Res. Lett. 7 (2012) 663. https://doi.org/10.1186/1556-276X-7-663.

[7] Z.W. Pan, Z.R. Dai, L. Xu, S.T. Lee, Z.L. Wang, Temperature-Controlled Growth of Silicon-Based Nanostructures by Thermal Evaporation of SiO Powders, J. Phys. Chem. B. 105 (2001) 2507–2514. https://doi.org/10.1021/jp004253q.

[8] S. Barcelo, Z. Li, Nanoimprint lithography for nanodevice fabrication, Nano Converg. 3 (2016) 21. https://doi.org/10.1186/s40580-016-0081-y.

[9] K.J. Morton, G. Nieberg, S. Bai, S.Y. Chou, Wafer-scale patterning of sub-40 nm diameter and high aspect ratio (>50:1) silicon pillar arrays by nanoimprint and etching, Nanotechnology. 19 (2008) 345301. https://doi.org/10.1088/0957-4484/19/34/345301.

[10] W. Jevasuwan, K.C. Pradel, T. Subramani, J. Chen, T. Takei, K. Nakajima, Y. Sugimoto, N. Fukata, Diffused back surface field formation in combination with two-step H 2 annealing for improvement of silicon nanowire-based solar cell efficiency, (n.d.).

[11] J. Chen, T. Subramani, W. Jevasuwan, K.C. Pradel, N. Fukata, Three-dimensional radial junction solar cell based on ordered silicon nanowires, Nanotechnology. 30 (2019). https://doi.org/10.1088/1361-6528/ab0451.

[12] S. Swann, Magnetron sputtering, Phys. Technol. 19 (1988) 67–75. https://doi.org/10.1088/0305-4624/19/2/304.

[13] D. Wang, P. Schaaf, Ni–Au bi-metallic nanoparticles formed via dewetting, Mater. Lett. 70 (2012) 30–33. https://doi.org/10.1016/j.matlet.2011.11.102.

[14] A. McEvoy, L. Castañer, T. Markvart, Solar cells: Materials, manufacture and operation, Sol. Cells Mater. Manuf. Oper. (2012) 1–641. https://doi.org/10.1016/C2011-0-07789-X.

Chapter 3. Optimizing non-radiative energy transfer from Si quantum dots to improve Si nanostructure hybrid solar cells

3.1 Enhancement of hybrid solar cells efficiency by quantum dots

The most popular conjugate p-type conducting polymer used as a hole transporting layer (HTL) is poly (3,4-ethylene dioxythiophene):poly (styrene sulfonate) or (PEDOT:PSS), which is transparent and extremely conductive. It is simple to create Schottky connections between PEDOT:PSS and SiNWs using a solution technique at room temperature.

In comparison to traditional c-Si solar cells, organic-inorganic hybrid heterojunction solar cells have considerably lower power conversion efficiency. Their energy conversion efficiency can be increased by using the non-radiative energy transfer (NRET) effect. Through a long-range dipole-dipole interaction, NRET may transmit energy to a neighboring layer, outperforming both short-range charge transfer and radiative energy transfer (RET). (RET).[1–9] This phenomenon was initially demonstrated in colloidal compound semiconductor quantum dots (QDs) including CdS, CdSe, and PbS.[1–8] nc-Si QDs represent a viable low-toxicity option that makes use of inexpensive and easily available materials.

Both the passivation rate generated by ligand molecules and the gap that exists between QDs and the surface of the solar cell have a strong influence on the magnitude of the NRET effect. In order to increase the NRET effect, the distance between SiQDs and the surfaces of solar cells should be reduced. By changing the ligand species, a reduced distance may be attained between the SiQDs and the solar cell surface.

In this chapter, the improvement of solar cell properties caused by the NRET effect was investigated. Between the PEDOT:PSS and Si nanostructures of hybrid heterojunction solar cells, SiQDs were introduced. In order to determine the nature of the connection that exists between the various passivation ligands and their respective lengths in order to optimize the NRET effect, a comparison study was carried out. In the end, a greater efficiency was effectively obtained by the largest augmentation of the NRET effect using SiQDs terminated with 1-octene, which has the shortest ligand length of the samples utilized in this investigation. This was the case because 1-octene has the shortest chain length of the investigated ligands.

3.2 Experimental

The metal-catalyzed electroless etching (MCEE) procedure is commonly used to create nanowires and nanohole structures.[10,11] To guarantee effective heterojunction contact between the PEDOT:PSS and Si nanostructures, we used the MCEE approach in conjunction with chemical polish etching (CPE)

to create Si nanotips for hybrid solar cell device production on an n-type (100) CZ (thickness 280 µm, resistivity 1 - 10 Ω cm). De-ionized water (DI water), acetone (ACE), piranha solution (H_2SO_4:H_2O_2), and isopropanol (IPA) were used to clean the Si substrates for 10 minutes each prior to etching. The two-step MCEE method was used to create the nanohole structures. The first phase used electroless metal deposition using HF/$AgNO_3$ solution, and the second involved a vertical etching step using HF/H_2O_2 solution. After removing Ag and silicon oxide, CPE treatment was performed with HNO_3 and HF to minimize surface defects and metal contamination. During this process, HNO_3 aids in the development of the oxide layer of the Si nanostructure and HF aids in its removal. The structure was transformed from nanohole to nanotip form by this method. Additional reports offer comparable process details.[12,13]

Figure 3.1 depicts the hybrid solar cell's manufacturing process. Spin coating was used to apply PEDOT:PSS to the Si nanotips. A hybrid heterojunction of PEDOT:PSS/Si was created when thermal annealing was used to dry the PEDOT:PSS solvent. Finally, Ag and Ti/Ag metal electrodes were deposited on the front and back, respectively.

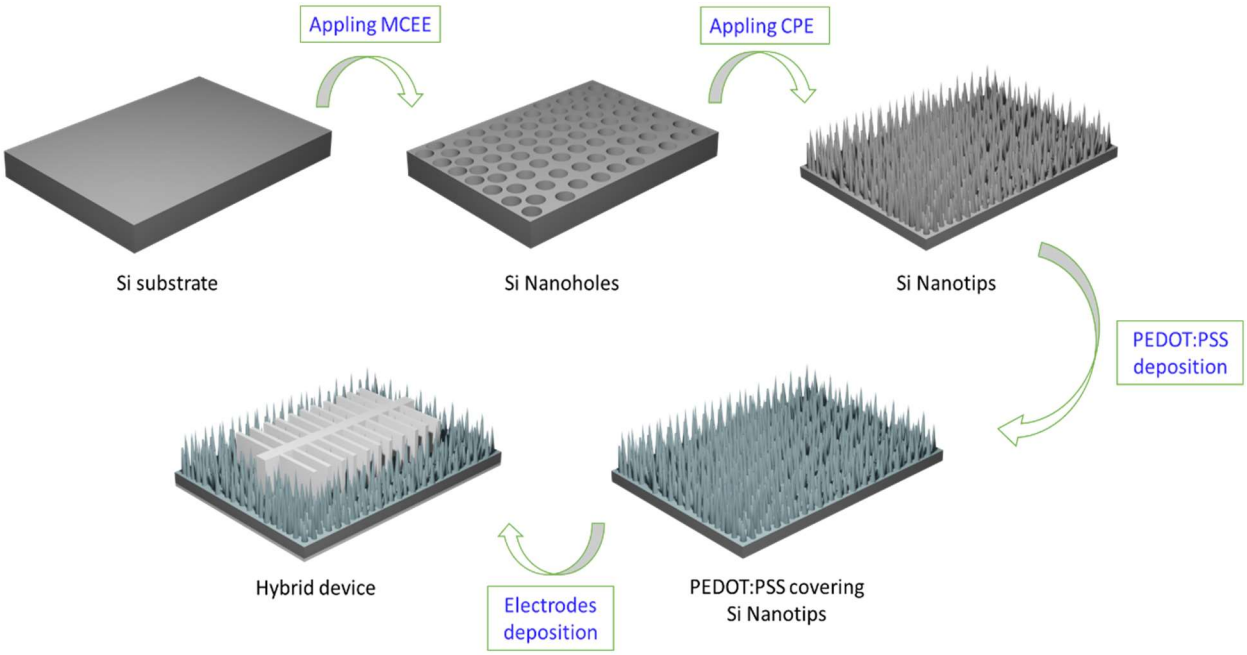

Figure 3.1 Schematics of the fabrication process of a hybrid solar cell device**.**

The fabrication process of SiQDs is illustrated in Figure 3.2. It consists of two distinct steps: (i) SiQDs/SiO_2 composite powders and (ii) ligand-terminated SiQDs. [14–16] (i) In the first step, Hydrogen silsesquioxane (HSQ), an H-Si-O substance acquired from Dow Chemical and utilized as received, is the beginning material. The HSQ was dissolved 40% by weight in methyl isobutyl ketone, also known commercially as FOx (flowable oxide). The solvent was first eliminated with the use of a rotating evaporator in a water bath at 40 °C under 75 Pa. The solvent had gone after about an hour, leaving an HSQ gel behind. The white solid powder was then produced by drying this gel overnight under vacuum.

This was put in a quartz crucible and then moved to a high temperature furnace. Thermal annealing was done at 1100 °C for 1 hour in a 95% Ar and 5% H_2 environment. After cooling to room temperature, a SiQDs/SiO_2 composite solid that is dark brown in color was produced. After being ground in a mechanical mortar and pestle, the mixture yielded the fine powder seen in Figure 3.2. (ii) After that, 200 mg of the SiQDs/SiO_2 composite powder was sonicated for one minute with 2 mL of deionized (DI) water and 2 mL of ethanol. 2 mL of HF was added to the aforementioned mixture in order to extract SiQDs from the composite and shrink the size of the SiQDs. In order to chemically etch the SiO_2 matrix and progressively shrink the size of the SiQDs, the suspension was agitated for 30 min, which led to the creation of hydrogen (H)-terminated SiQDs. After that, the supernatant was decanted after the H-terminated SiQDs were separated using excess toluene. To create a powder of H-terminated SiQDs, the product was then transferred to a round-bottomed flask and dried under a dry Ar gas flow. 10 mL of 1-octadecene solution was added, and 1 hour of Ar bubbling was used to remove the gas. The reaction was conducted overnight at 290 °C in ambient Ar. The surface termination species is changed from H to 1-octadecene by this process. The SiQDs were terminated using the same techniques with 1-dodecene and 1-octene, but at reaction temperatures of 190 °C and 100 °C, respectively. A 1:1 combination of ethanol and methanol was used to eliminate any extra 1-octadecene from the resultant clear light-yellow solution. To obtain the 1-octadecene-passivated SiQD solution, 5 mL of toluene was added at the end.

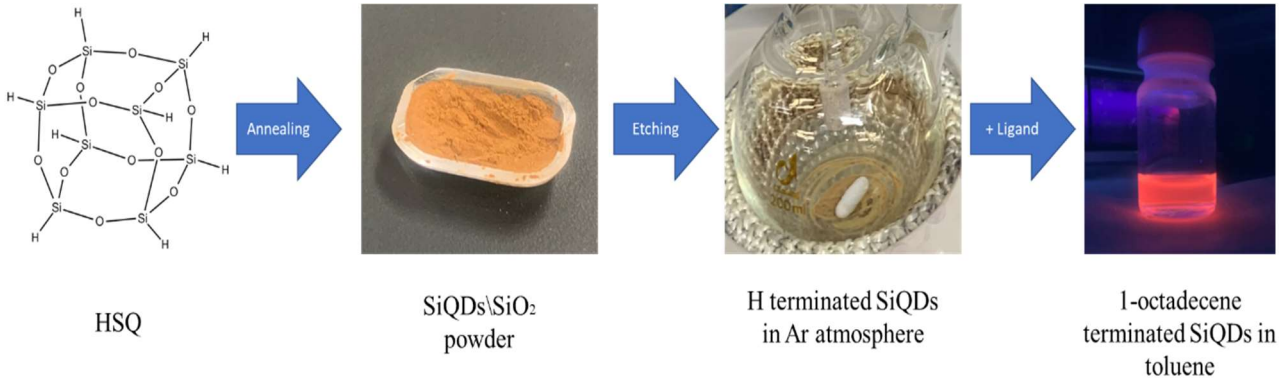

Figure 3.2 Fabrication process of Si QDs terminated with ligand molecules.

3.3 Results and discussion

3.3.1 Characterization of SiQDs and Si nanotip structures covered with PEDOT:PSS

To verify the creation of 1-octadecene-passivated SiQDs, TEM measurements were made. The production of QDs with an average diameter of 3 to 4 nm is seen in the TEM image in Figure 3.3 (a). Figure 3.3 (b) displays a high-resolution TEM image with interplanar lattice fringes of 0.31 nm, corresponding to the Si (111) lattice space. These findings provide proof that SiQDs are formed. The optical characteristics of 1-octadecene-passivated SiQDs are depicted in Figure 3.3 (c). The characteristic Stokes shift that has been observed for SiQDs is visible in the absorption and

photoluminescence spectra. These findings unequivocally demonstrate that the production of SiQDs was successful.

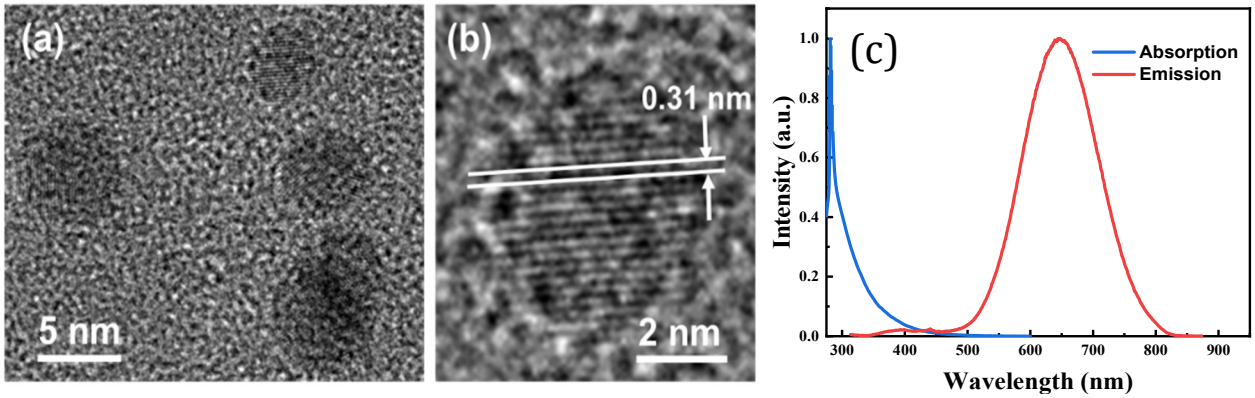

Figure 3.3 (a) TEM and (b) HRTEM images of 1-octadecene passivated SiQDs. (c) Normalized absorption and fluorescence spectrum of 1-octadecene passivated SiQDs.

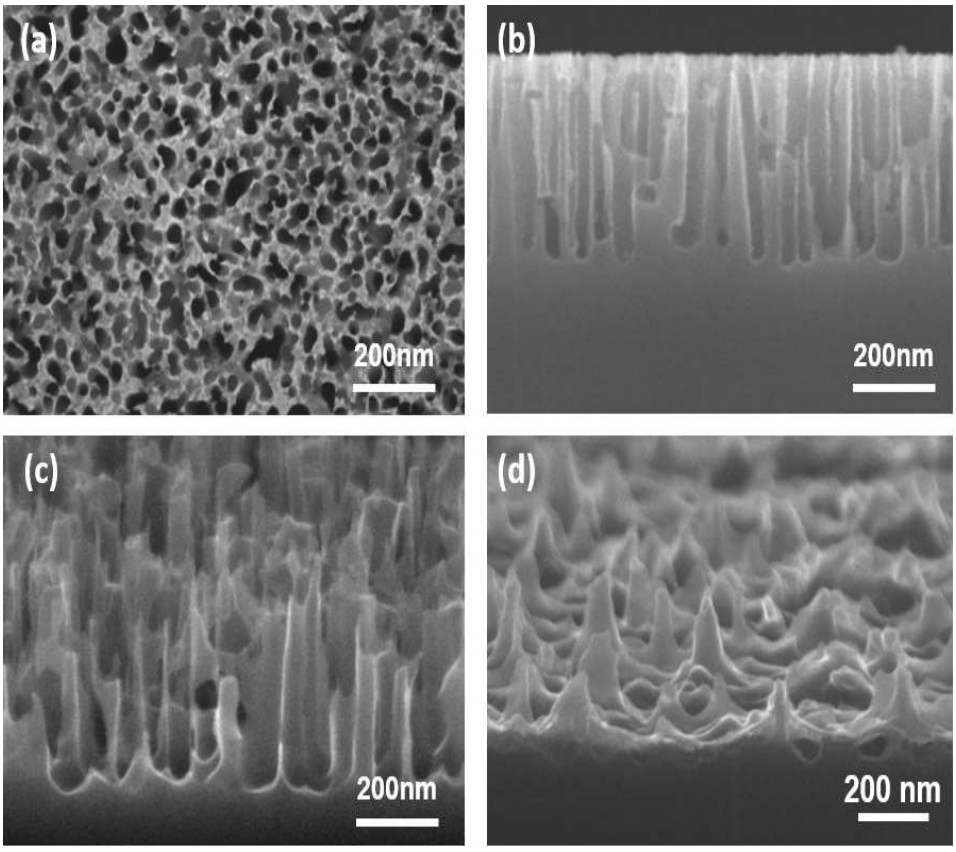

Figure 3.4 SEM images of (a) top-view of the nanoholes, (b) cross-sectional view of the nanoholes and (c) silicon nanotips as fabricated. (d) SEM image of silicon nanotips coated with PEDOT:PSS.

We created Si nanotip structures using a two-step MCEE approach coupled with a CPE treatment to make sure that the heterojunctions between PEDOT:PSS and Si nanostructures had excellent contacts. A top view and cross-sectional view SEM image of high-density nanoholes created utilizing the two-step

MCEE method are shown in Figures 3.4 (a) and (b). These nanoholes are typically 30 to 50 nm in diameter. SEM images of modified Si nanotips following CPE treatment are shown in Figure 3.4(c). The nanostructures' depth and density were decreased, while the distances between them were expanded. Additionally, the CPE process eliminates metal contamination and minimizes surface imperfections. To optimize the coverage of PEDOT:PSS, the concentration and treatment period of CPE may be adjusted to modify the surface shape of nanotips. Figure 3.4 (d) depicts a cross-sectional view of nanotips coated with PEDOT:PSS, revealing PEDOT:PSS infiltrating and coating the surface of the Si nanotips. By reducing the length of the minority carrier diffusion paths, the heterojunctions with Si nanotips and PEDOT:PSS enhance the junction area and hence the efficiency of charge collection. Figure 3.5 clearly illustrates how the changed nanostructure's improved solar cell performance as a result of CPE treatment.

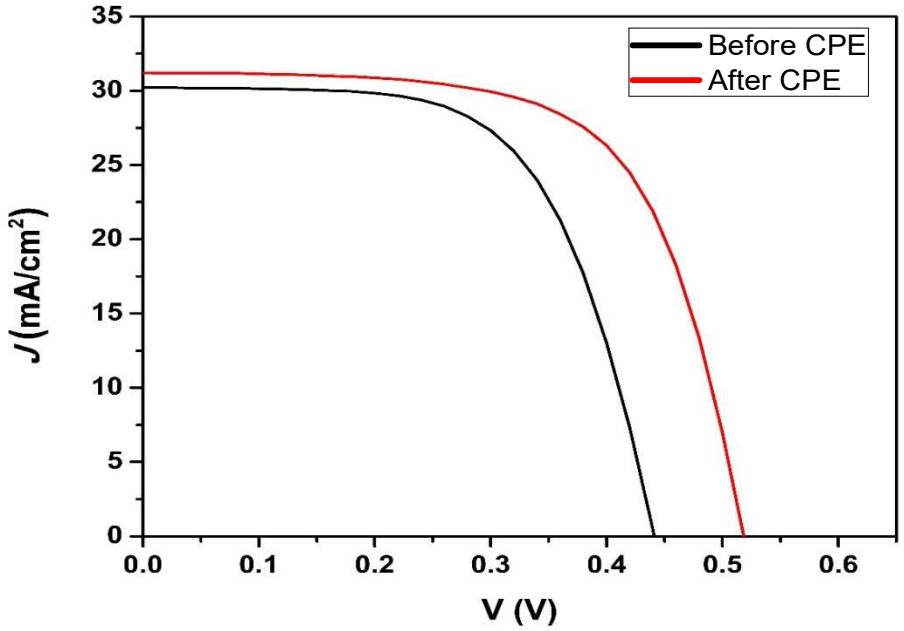

Figure 3.5 J-V curve of the hybrid Si solar cell device before and after CPE

3.3.2 Energy transfer effect by SiQDs

Using energy transfer from SiQDs passivated with chemical ligands is a practical way to increase the efficiency of energy conversion.[9,13,17] As illustrated in Figure 3.6 (a), the SiQDs were coated on the Si nanotip surfaces before being coated with the PEDOT:PSS. Because the PEDOT:PSS coating is carried out at room temperature and pressure, it has no effect on the SiQDs.

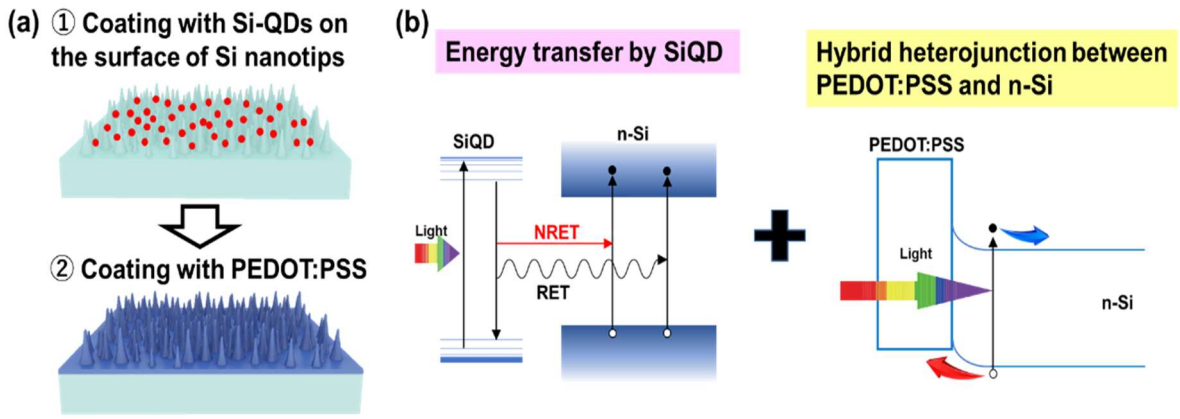

Figure 3.6 (a) Fabrication process of SiQDs and PEDOT:PSS coating on the Si nanotips. (b) Schematic illustration of energy transfer from SiQD to n-Si and energy band diagram of PEDOT:PSS and n-Si hybrid heterojunctions.

Figure 3.6 (b) displays the energy transfer and energy band diagram of the PEDOT:PSS/Si heterojunction and SiQDs. SiQDs use the NRET and RET processes to transmit the energy from the UV area of solar light to the Si layer. More electron-hole pairs may be produced in the n-Si region as a result of this SiQD effect. Effective separation of light-induced carriers is achieved by the hybrid heterojunction of PEDOT:PSS and n-Si. Increased short circuit current and improved energy conversion efficiency can be achieved by combining the energy transfer effect with hybrid heterojunctions. To study the SiQD energy transfer impact in the hybrid heterojunction solar cell, solar cell devices were created. The J-V curves and the solar cell performance with and without coating with SiQDs are shown in Figure 3.7 and Table 3.1. 1-octadecene is used to terminate the SiQDs. The solar cell with SiQDs exhibits a higher J_{SC} of 33.08 mA cm^{-2} than the solar cell without SiQDs, resulting in a higher energy conversion efficiency of 11.39%. This is because of the NRET effect produced by the SiQDs.[9,13]

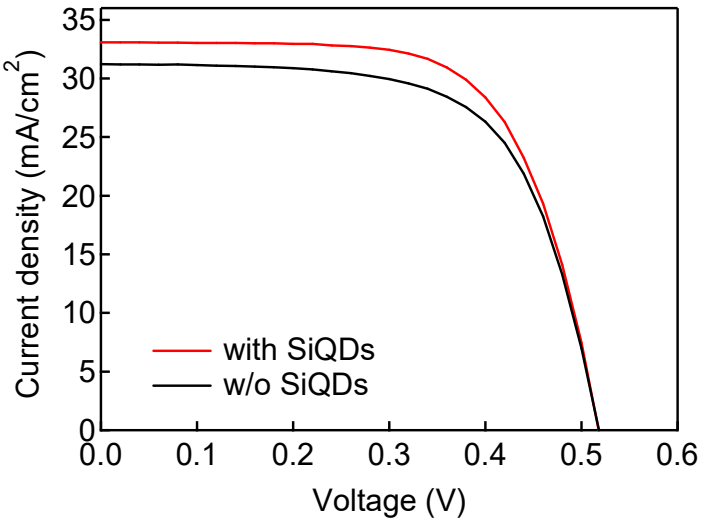

Figure 3.7 J-V curve of the hybrid Si solar cell device with and without SiQD

Table 3.1 Solar cell properties of hybrid Si solar cell with and without the SiQD coating.

	J_{SC} (mA cm^{-2})	V_{OC} (V)	FF	η (%)
Without SiQDs	31.10 ± 0.12	0.52 ± 0.01	0.65 ± 0.01	10.5 ± 0.40
With SiQDs	33.08 ± 0.14	0.52 ± 0.01	0.67 ± 0.01	11.4 ± 0.44

Higher energy solar light can be efficiently absorbed by the SiQDs, and the energy can then be transferred via NRET to the underlying n-Si layer. The organic polymer PEDOT:PSS and n-Si nanotips efficiently segregate the produced charge carriers in the n-Si region. The short-circuit current therefore rises. The solar cell's band structure remains unaffected, hence the open circuit voltage is unaffected as well. The SiQDs with the passivated ligand can function as a hydrophilic layer, which can assist offer higher coverage of PEDOT:PSS and lower the series resistance, which results in an improvement in FF.

The Si nanotip array with nc-Si QD terminated with 1-octadecene displayed substantially better external quantum efficiency (EQE) values than did the hybrid device without nc-Si QD (Figure 3.8). The higher UV light absorptivity of nc-Si QDs, which is reabsorbed by the hybrid device through the RET and NRET effect, is thought to be responsible for the improvement. This, in turn, has greatly boosted the energy conversion efficiency of solar cells.

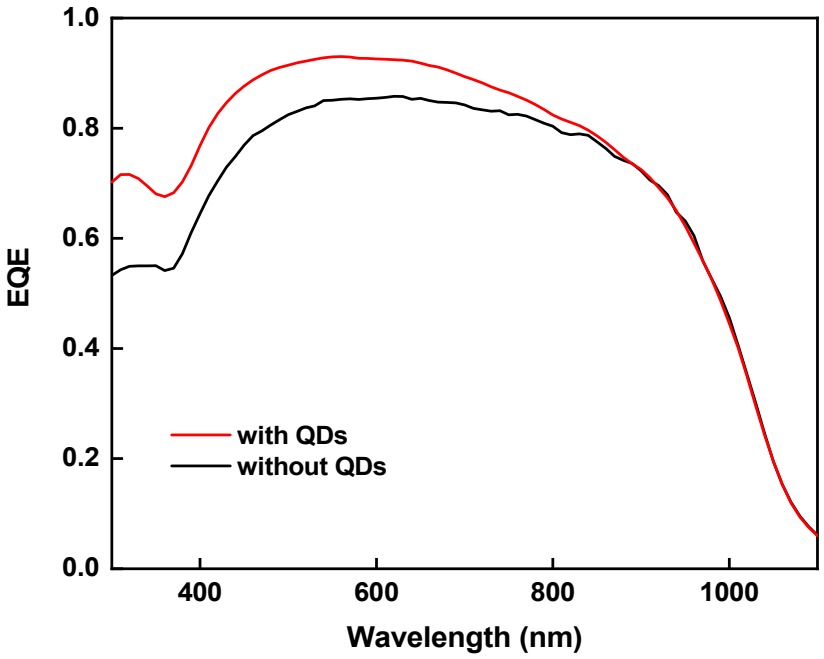

Figure 3.8 EQE spectra of Si nanotips solar cells with and without nc-Si QDs.

3.3.3 Effect of ligand length passivated with SiQDs

The NRET effect depends heavily on the length of the ligands that have been passivated with the surface of SiQDs, hence this factor is crucial for its efficient application. Over short distances, the transfer efficiency caused by the NRET effect is kept at a high level (very near to 100%), but as the distance increases, the efficiency rapidly drops.[18]

The Förster radius (R_0) is the radius at which the transfer efficiency is equal to 50%. One can determine the Förster radius (R_0) by [1]

$$(\tau_{NRET})^{-1} = (R_0/d)^4(\tau_{RET})^{-1} \qquad (3.1)$$

Here, the distance (d) is calculated by adding the ligand's length and the SiQDs' radius, and $(\tau_{RET})^{-1}$ and $(\tau_{NRET})^{-1}$is the RET and NRET decay rates. In order to calculate the NRET efficiency (Q_F), one uses the following equation:[19]

$$Q_F = \frac{{R_0}^6}{d^6+{R_0}^6} \qquad (3.2)$$

If d << R_0, Q_F approaches 1, indicating that the NRET process loses almost no energy. If d >> R_0, the Q_F will be close to 0, implying that the NRET procedure cannot occur. As a result, the NRET is a phenomenon that greatly depends on distance.

To explore the influence of the NRET impact on ligand length, the average size of SiQDs was held constant while the ligand length was varied. This is because the size of SiQDs affects the emission characteristics of SiQDs, and therefore the NRET effect. A shorter ligand length decreases the overall distance (d) in Eq. (3.2), increasing the Q_F. To passivate the SiQD surface, 1-octene and 1-dodecene, two shorter ligands, were utilized in place of 1-octadecene.1-octene, 1-dodecene and 1-octadecene have lengths that are around 0.75 nm, 1.25 nm, and 2 nm, respectively.[20]

1-octene and 1-dodecene both have ligand passivation procedures that are similar to those of 1-octadecene. Because 1-octene and 1-dodecene have a lower boiling point (bp) than 1-octadecene, the only change is the heating temperature.[21] In this thesis we term these SiQDs samples with different passivation ligands the octene sample, dodecene sample, and octadecene sample. The PL decay characteristics of the three samples were measured after deposited on glass and silicon substrates and are depicted in Figure 3.9 in order to assess the energy transfer efficiency. Table 3.2 is a list of the lifetime's fitting outcomes. For all the samples, τ_{glass} is greater than $\tau_{silicon}$. This difference is due to the disparity between the radiative and nonradiative decay rates. The radiative and intrinsic non-radiative recombination channels dominate the PL decay of SiQDs on a glass substrate, whereas NRET and RET to the Si layer contribute to the PL decay rate as an additional energy transfer channel for SiQDs on a Si substrate. This is due to the fact that the NRET occurs successfully from the SiQDs to the Si substrate.

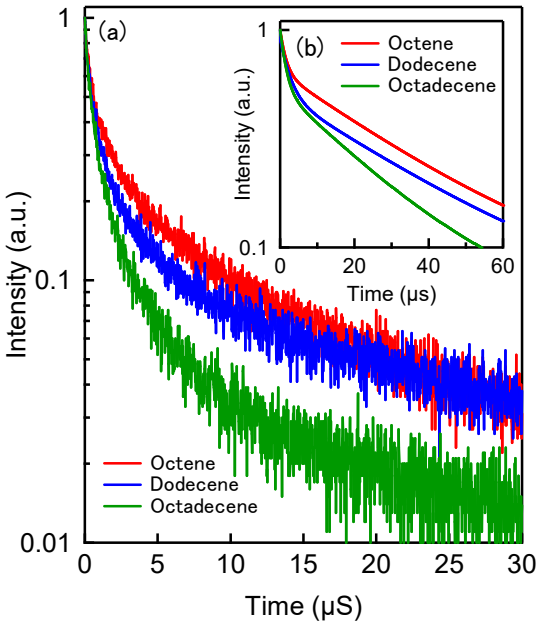

Figure 3.9 PL decays of SiQDs passivated with three different ligands coated on (a) Si and (b) glass substrates.

Table 3.2 PL lifetimes of SiQDs passivated with three different ligands coated on glass and Si substrates.

	τ_{glass} (μs)	$\tau_{silicon}$ (μs)
Octadecene	24.8	5.81
Dodecene	27.6	6.06
Octene	34.2	6.60

By examining the PL decay curves for the glass and Si substrates, it is possible to determine the PL decays brought on by the two energy transfer mechanisms, RET and NRET. The primary kind of decay for the SiQDs on the glass is photon emission by the RET.[1,9] Thus, it can be described in the case of silicon as: [1,9]

$$(\tau_{RET})^{-1} = \text{QE}\,(\tau_{silicon})^{-1} \qquad (3.3)$$

$(\tau_{RET})^{-1}$is the RET decay rate, QE is the quantum efficiency (=30%) and $(\tau_{silicon})^{-1}$ is the total decay rate of the SiQDs on silicon. There is an NRET channel to the Si surface for SiQDs on silicon.

The decay rate $(\tau_{silicon})^{-1}$ can also be determined by

$$(\tau_{silicon})^{-1} = (\tau_{glass})^{-1} + (\tau_{ET})^{-1} \qquad (3.4)$$

$(\tau_{ET})^{-1} = (\tau_{RET})^{-1} + (\tau_{NRET})^{-1}$ (3.5)

$(\tau_{ET})^{-1}$, $(\tau_{RET})^{-1}$ and $(\tau_{NRET})^{-1}$ are the total energy transfer, RET and NRET decay rates of SiQDs.

The calculated RET and NRET decay rates are listed in Table 3.3. The findings indicate that in every sample, the NRET decay rate is faster than the RET decay rate. Compared to the RET rate, the NRET rates are around 1.5–1.7 times faster. This suggests that the NRET mechanism becomes dominant in the energy transfer process and may be efficiently applied to raise solar cell efficiency.

Table 3.3 Energy transfer rates and their ratio of the three samples

	$\tau_{(RET)}^{-1}$	$\tau_{(NRET)}^{-1}$	$\tau_{(NRET)}^{-1} / \tau_{(RET)}^{-1}$
Octadecene	$(19.37\ \mu s)^{-1}$	$(12.48\ \mu s)^{-1}$	1.55
Dodecene	$(20.20\ \mu s)^{-1}$	$(12.61\ \mu s)^{-1}$	1.60
Octene	$(22.00\ \mu s)^{-1}$	$(13.00\ \mu s)^{-1}$	1.69

Equations (1) and (2) can be used to compute the Forster radius R_0 and NRET efficiency Q_F. Table 3.4 presents the results. While the NRET efficiency exhibits an inverse correlation with d and R_0, the R_0 obtained for the three samples exhibits a correlation with the distance d (ligand length plus average SiQD radius). In this case, the average SiQD radius is unaffected by the ligand type. When d changes, the length of the ligand also changes. The energy was transmitted through the NRET mechanism most efficiently by the SiQDs passivated with octene. This finding demonstrates unequivocally that making the passivation ligands shorter can boost the NRET efficiency.

Table 3.4 Calculated values of Forster radius (R_0) and NRET efficiency (Q_F) of the three samples. d is ligand length plus SiQD radius.

	d (nm)	**R_0 (nm)**	**Q_F (%)**
Octadecene	3.5	3.9	64.9
Dodecene	2.8	3.1	67.0
Octene	2.3	2.6	68.8

To examine the influence of ligand length on the NRET, three different ligands were used in the fabrication of the hybrid PEDOT:PSS/Si heterojunction solar cells. Figure 3.10 (a) depicts the solar cell

device performance, while Table 3.5 lists the solar cell performance parameters. By decreasing the length of the ligand from octadecene to octene, the performance of solar cells was enhanced. The sample of octene had the greatest J_{SC}, at 36.20 mA cm^{-2}. Due to the enhancement of J_{SC}, the octene sample provided the greatest level of efficiency at 12.4%.

Table 3.5 Parameters of solar cell performance after coating the three samples.

	J_{SC} (mA cm^{-2})	V_{OC} (V)	FF	η (%)
Octadecene	33.08 ± 0.14	0.52 ± 0.01	0.67 ± 0.01	11.4 ± 0.44
Dodecene	34.41 ± 0.11	0.53 ± 0.005	0.66 ± 0.015	12.0 ± 0.42
Octene	36.20 ± 0.09	0.52 ± 0.01	0.67 ± 0.01	12.4 ± 0.46

Figure 3.10 (b) illustrates the correlation between J_{SC} enhancement and NRET efficiency to clarify the NRET impact of SiQDs terminated with various ligands. Increased NRET efficiency increases J_{SC}. This research demonstrates conclusively the significance of the NRET effect in boosting photocarrier production in the active layer of solar cells. These findings point to a possible improvement in solar cell performance due to greater NRET efficiency after SiQDs have been passivated with shorter ligands.

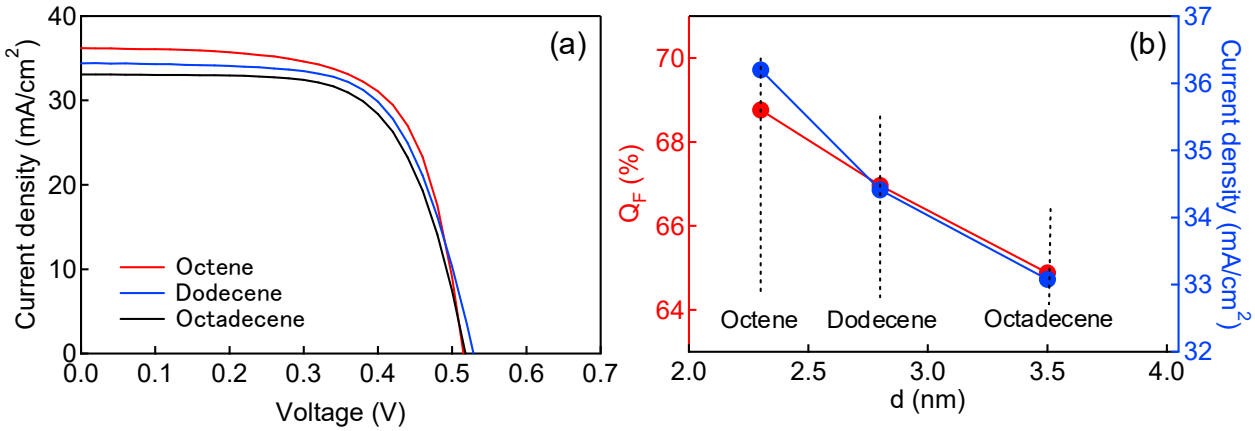

Figure 3.10 (a) J-V curves for hybrid PEDOT:PSS/Si heterojunction solar cells after coating with ligand molecules. (b) The relationship between J_{SC} improvement and NRET efficiency.

As mentioned before, SiQDs absorb solar light and subsequently transport the energy to the depletioned area in the n-Si layer, where photocarriers can be separated. Unlike Si homojunction solar cells, hybrid heterojunction solar cells benefit from the NRET effect due to their structure. In Figure 3.11

(a) and (b), the NRET processes of a Si homojunction cell and a hybrid cell are compared with one another. Figures 3.11 (a) illustrates a range of separations between the SiQDs and the depletion area in a p-Si/n-Si homojunction cell. Some photo-carriers are unable to be efficiently segregated due to recombination by majority carriers in the p-Si layer, resulting in a reduced photocurrent. Figure 3.11 (a) also shows a hybrid heterojunction solar cell in which the depletion region is created in the n-Si layer and the SiQDs are in contact with this region. This arrangement works well to segregate the photo-carriers and hence promotes the NRET effect. Figures 3.11(b) illustrate how J_{SC} has been improved in these two configurations. In comparison to a homojunction structure made of p-Si and n-Si, the enhanced J_{SC} in a PEDOT:PSS/n-Si hybrid heterojunction is significantly greater. In contrast to the p-Si/n-Si homojunction, which generates some electron-hole pairs outside the depletion zone, the PEDOT:PSS/n-Si hybrid structure generates virtually all of its electron-hole pairs inside the depletion region and efficiently separates them, leading to a larger J_{SC}. Accordingly, hybrid configurations are a good fit for exploiting the NRET effect.

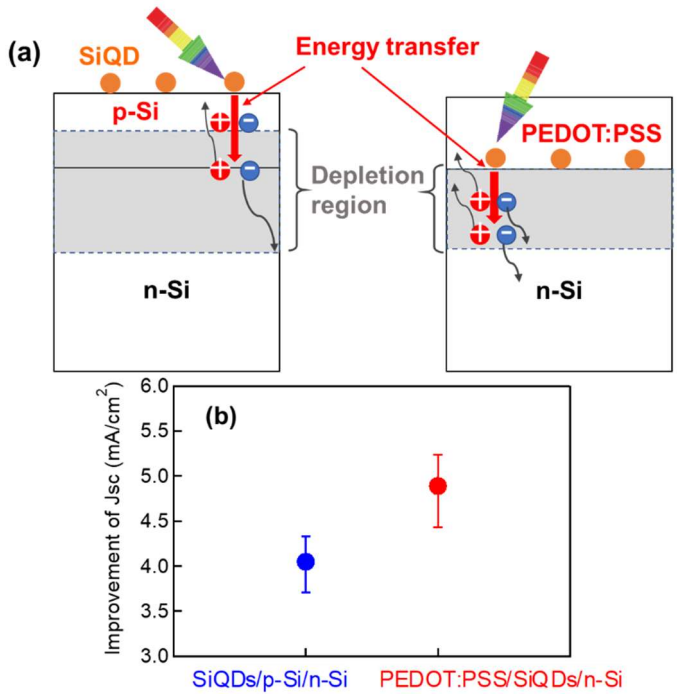

Figure 3.11 (a) Schematic diagram of the difference in energy transfer of SiQD at p-Si/n-Si homojunction and PEDOT:PSS/n-Si hybrid heterojunction structure. (b) Comparison of improved J_{SC} seen with these two structures.

H-terminated SiQDs, which have a shorter bond length than the aforementioned ligand species, were examined for in-depth further research into the dependency of NRET efficiency on ligand length. Between the Si nanotips and PEDOT:PSS, as well as the structures depicted in Figure 3.6, H-terminated SiQDs were inserted. With J_{SC} = 32.83 mA cm^{-2}, Voc = 0.51 V, and FF = 0.70, the efficiency was 11.6%. Because of the degradation in the J_{SC}, the efficiency was surprisingly lower than that achieved from the

hybrid solar cells containing octane- and dodecene-terminated SiQDs. This is probably because SiQDs' surface has been reoxidized. H-terminated SiQDs are more susceptible to reoxidation than octane- and dodecene-terminated SiQDs. This outcome demonstrates that resistance to reoxidation is crucial for maximizing the SiQDs' NRET impact.

3.4 Summary

The NRET effect caused by SiQDs terminated with ligands was studied in hybrid heterojunction solar cells made of PEDOT:PSS and Si nanostructures. The hybrid heterojunction structure offers the benefits of both the Si nanostructures' broad-band optical absorption capacity and the PEDOT:PSS polymer's easy fabrication methods using a solution-based method. Improved J_{SC} was produced by the NRET effect of SiQDs capped with ligands, illuminating a practical means of enhancing solar cell characteristics. Compared to homojunction SiNW solar cells with radial p-n junctions, PEDOT:PSS/Si nanostructure hybrid solar cells are more effective at using the NRET. The NRET phenomenon is a strongly distance-dependent phenomena, as demonstrated by the strong relationship between the NRET process and the length of the passivation ligands. Shortening the ligand length improved NRET efficiency and led to greater J_{SC}, which in turn improved energy conversion efficiency.

3.5 References

[1] S. Lu, A. Madhukar, Nonradiative resonant excitation transfer from nanocrystal quantum dots to adjacent quantum channels, Nano Lett. 7 (2007) 3443–3451. https://doi.org/10.1021/nl0719731.

[2] H.M. Nguyen, O. Seitz, D. Aureau, A. Sra, N. Nijem, Y.N. Gartstein, Y.J. Chabal, A. V. Malko, Spectroscopic evidence for nonradiative energy transfer between colloidal CdSe/ZnS nanocrystals and functionalized silicon substrates, Appl. Phys. Lett. 98 (2011) 161904. https://doi.org/10.1063/1.3579545.

[3] S. Chanyawadee, R.T. Harley, M. Henini, D. V. Talapin, P.G. Lagoudakis, Photocurrent enhancement in hybrid nanocrystal quantum-dot p-i-n photovoltaic devices, Phys. Rev. Lett. 102 (2009) 077402. https://doi.org/10.1103/PhysRevLett.102.077402.

[4] G. Allan, C. Delerue, Energy transfer between semiconductor nanocrystals: Validity of Förster's theory, Phys. Rev. B - Condens. Matter Mater. Phys. 75 (2007) 195311. https://doi.org/10.1103/PhysRevB.75.195311.

[5] S. Lu, Z. Lingley, T. Asano, D. Harris, T. Barwicz, S. Guha, A. Madhukar, Photocurrent induced by nonradiative energy transfer from nanocrystal quantum dots to adjacent silicon nanowire conducting

channels: Toward a new solar cell paradigm, Nano Lett. 9 (2009) 4548–4552. https://doi.org/10.1021/nl903104k.

[6] H.M. Nguyen, O. Seitz, W. Peng, Y.N. Gartstein, Y.J. Chabal, A. V. Malko, Efficient radiative and nonradiative energy transfer from proximal CdSe/ZnS nanocrystals into silicon nanomembranes, ACS Nano. 6 (2012) 5574–5582. https://doi.org/10.1021/nn301531b.

[7] O. Seitz, L. Caillard, H.M. Nguyen, C. Chiles, Y.J. Chabal, A. V. Malko, Optimizing non-radiative energy transfer in hybrid colloidal-nanocrystal/ silicon structures by controlled nanopillar architectures for future photovoltaic cells, Appl. Phys. Lett. 100 (2012) 021902. https://doi.org/10.1063/1.3675634.

[8] M. Achermann, M.A. Petruska, S. Kos, D.L. Smith, D.D. Koleske, V.I. Klimov, Energy-transfer pumping of semiconductor nanocrystals using an epitaxial quantum well, Nature. 429 (2004) 642–646. https://doi.org/10.1038/nature02571.

[9] M. Dutta, L. Thirugnanam, P. Van Trinh, N. Fukata, High Efficiency Hybrid Solar Cells Using Nanocrystalline Si Quantum Dots and Si Nanowires, ACS Nano. 9 (2015) 6891–6899. https://doi.org/10.1021/acsnano.5b03268.

[10] K. Peng, J. Hu, Y. Yan, Y. Wu, H. Fang, Y. Xu, S. Lee, J. Zhu, Fabrication of single-crystalline silicon nanowires by scratching a silicon surface with catalytic metal particles, Adv. Funct. Mater. 16 (2006) 387–394. https://doi.org/10.1002/adfm.200500392.

[11] Z. Huang, N. Geyer, P. Werner, J. De Boor, U. Gösele, Metal-assisted chemical etching of silicon: A review, Adv. Mater. 23 (2011) 285–308. https://doi.org/10.1002/adma.201001784.

[12] T. Subramani, J. Chen, Y. Kobayashi, W. Jevasuwan, N. Fukata, Highly Air-Stable Solution-Processed and Low-Temperature Organic/Inorganic Nanostructure Hybrid Solar Cells, ACS Appl. Energy Mater. 2 (2019) 2637–2644. https://doi.org/10.1021/acsaem.8b02218.

[13] T. Subramani, J. Chen, Y.L. Sun, W. Jevasuwan, N. Fukata, High-efficiency silicon hybrid solar cells employing nanocrystalline Si quantum dots and Si nanotips for energy management, Nano Energy. 35 (2017) 154–160. https://doi.org/10.1016/j.nanoen.2017.03.037.

[14] C.M. Hessel, E.J. Henderson, J.G.C. Veinot, Hydrogen silsesquioxane: A molecular precursor for nanocrystalline Si-SiO2 composites and freestanding hydride-surface-terminated silicon nanoparticles, Chem. Mater. 18 (2006) 6139–6146. https://doi.org/10.1021/cm0602803.

[15] M.L. Mastronardi, F. Maier-Flaig, D. Faulkner, E.J. Henderson, C. Kübel, U. Lemmer, G.A. Ozin, Size-dependent absolute quantum yields for size-separated colloidally-stable silicon nanocrystals, Nano Lett. 12 (2012) 337–342. https://doi.org/10.1021/nl2036194.

[16] M.L. Mastronardi, F. Hennrich, E.J. Henderson, F. Maier-Flaig, C. Blum, J. Reichenbach, U. Lemmer, C. Kübel, D. Wang, M.M. Kappes, G.A. Ozin, Preparation of monodisperse silicon nanocrystals using density gradient ultracentrifugation, J. Am. Chem. Soc. 133 (2011) 11928–11931. https://doi.org/10.1021/ja204865t.

[17] N. Fukata, T. Subramani, W. Jevasuwan, M. Dutta, Y. Bando, Functionalization of Silicon Nanostructures for Energy-Related Applications, Small. 13 (2017) 1–13. https://doi.org/10.1002/smll.201701713.

[18] S. Maniam, H.F. Higginbotham, T.D.M. Bell, S.J. Langford, Chapter 8. Naphthalene Diimide-based Photovoltaics, in: Naphthalenediimide Its Congeners From Mol. to Mater., Royal Society of Chemistry (RSC), 2017: pp. 244–276. https://doi.org/10.1039/9781782621386-00244.

[19] G. Heliotis, G. Itskos, R. Murray, M.D. Dawson, I.M. Watson, D.D.C. Bradley, Hybrid inorganic/organic semiconductor heterostructures with efficient non-radiative energy transfer, Adv. Mater. 18 (2006) 334–338. https://doi.org/10.1002/adma.200501949.

[20] Y. Liu, M. Gibbs, J. Puthussery, S. Gaik, R. Ihly, H.W. Hillhouse, M. Law, Dependence of carrier mobility on nanocrystal size and ligand length in pbse nanocrystal solids, Nano Lett. 10 (2010) 1960–1969. https://doi.org/10.1021/nl101284k.

[21] R.J. Clark, M. Aghajamali, C.M. Gonzalez, L. Hadidi, M.A. Islam, M. Javadi, M.H. Mobarok, T.K. Purkait, C.J.T. Robidillo, R. Sinelnikov, A.N. Thiessen, J. Washington, H. Yu, J.G.C. Veinot, From hydrogen silsesquioxane to functionalized silicon nanocrystals, Chem. Mater. 29 (2017) 80–89. https://doi.org/10.1021/acs.chemmater.6b02667.

Chapter 4. Solution-processed thermally treated VO_x thin films' use as hole injectors in Si nanowire-based solar cells

4.1 Vanadium oxides films as a hole transporting layer

In OSCs and organic light-emitting diodes, transition metal oxides (TMOs) with high work functions (WF) are frequently utilized as a layer that transports holes.[1–4] Vanadium oxide thin films have a wide range of beneficial characteristics, making them very promising. They are prepared using a variety of methods, including pulsed laser deposition, chemical vapor deposition, spray pyrolysis, magnetron sputtering, and sol-gel processes.[5–9] Due to its ease of use and low cost, the last approach is of great interest. The quality of films created using this method can be on par with those created using the other methods stated above. In a prior work done by Zilberberg et al., PEDOT:PSS was swapped out for sol-gel produced V_2O_5 film to serve as the hole extraction layer in an OSC. Without any post-deposition treatment, this layer was homogeneous and amorphous and had a high WF of 5.6 eV.[10] In comparison to PEDOT:PSS-derived OSCs, the V_2O_5-derived device performed better and shown higher stability, losing just 20% of its original efficiency after 400 hours of usage in an atmospheric environment. Hancox et al. created films of sub-stoichiometric solution-processable vanadium pentoxide ($V_2O_{x(sol)}$) for use as hole-extracting layers in OSCs under various atmospheric processing conditions. Gap states were discovered within the bandgap of $V_2O_{x(sol)}$ below the Fermi level as a result of the partial filling of the V *3d* lower band, which permitted hole extraction. ITO/$V_2O_{x(sol)}$/P3HT:PCBM/BCP/Al attained a better conversion efficiency (η = 3.34%) than other comparable cell architectures of MoO_x, ITO, and PEDOT:PSS based cells.[11]

The previously created PEDOT:PSS/Si hybrid solar cells have a limited lifetime because of oxidation in the polymer layer caused by water and molecular oxygen transport through it when used outdoors. As a result, the device degrades generally and exhibits unstable performance.[12,13] The biggest obstacle to these devices' widespread adoption is the necessity for permanent stability. In one attempt to improve the stability of this hybrid device, PEDOT:PSS was replaced with zwitterionic tetrathiafulvalene (TTF)-extended dicarboxylate radicals (TEDs) and TED-Li. With TED-Li, this cell demonstrated a longer lifetime.[14] However, the processes for creating these organic compounds are time-consuming.[15] Another team was able to achieve efficiency that is equivalent to a hybrid PEDOT:PSS/Si device.[16] A SiNW substrate was sandwiched between layers of V_2O_5 and TiO_2, which served as the corresponding hole- and electron-transporting layers. Although the minority carrier lifetime was increased by the deposition of the V_2O_5 layer, the recombination rate is predicted to eventually rise because the SiNW surface is only partially passivated by the deposited V_2O_5 layer, which only covers the top of the nanowires. The work on creating and enhancing passivation has been

inspirational, but the usage of V_2O_5, which is notorious for its toxicity, frustrates researchers and encourages them to seek for better substitutes.

In this chapter, the fabrication of different vanadium oxide (VO_x) thin films with different oxidation states (V_2O_{5-x}, VO_{2-x}) using a simple solution processing-based technique and annealing in different atmospheres will be discussed. The hole-injection ability of the fabricated VO_x films was investigated after their use in SiNW-based solar cells. A comparison of the outdoor stability of VO_{2-x}/SiNWs and PEDOT:PSS/SiNWs devices was undertaken.

4.2 Experimental

4.2.1 Fabrication of VO_x/Si Heterojunction Solar Cells

In order to create the precursor solution, 0.02 milliliters of Vanadium(V) oxytriisopropoxide (VOTIP) was diluted in 3 milliliters of anhydrous IPA (99.9%). For 60 seconds at 3000 rpm, the solution was spun onto a Si substrate (both planar and with NWs). During the spin-coating process, the precursor solution reacted with ambient water vapor to create non-stoichiometric V_2O_5.[9] By adjusting the spin-coating speed, it is possible to alter the thickness of the deposited layers. Decomposition of Vanadium(V) oxytriisopropoxide (VOTIP) into solid TMO is commenced at above 104 °C, as shown by Zhang et al.[17] The samples are heated on a hotplate at 150 °C for 3 minutes to completely evaporate the water and isopropanol. Next, the samples were placed in a tube furnace and annealed in oxygen, nitrogen, or a vacuum (0.15 Torr) at the required temperatures. In order to create Schottky solar cells, an Ag grids (250 nm) and Ti/Ag (50 nm/250 nm) electrodes were sputtered onto the front and back sides of the samples with the NWs structures, respectively. This is seen in the schematic design in Figure 4.1.

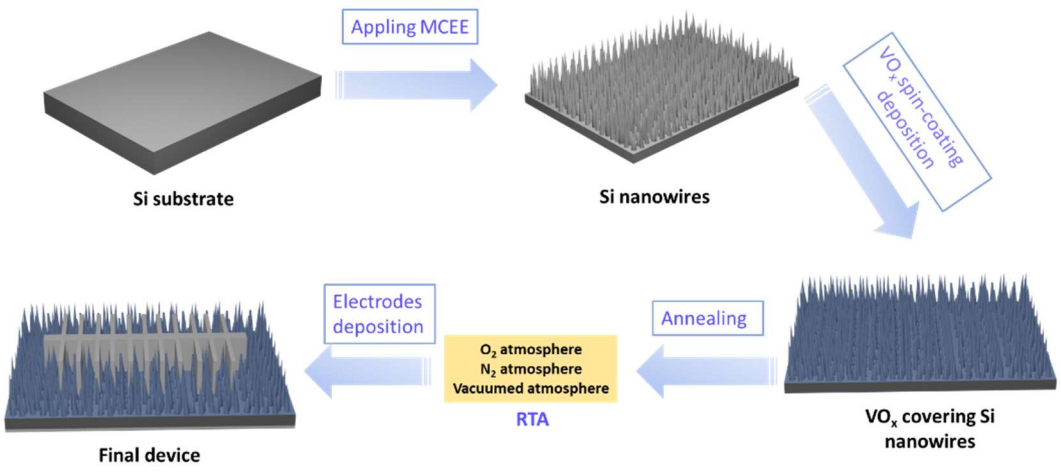

Figure 4.1 Schematics of the fabrication process of a hybrid solar cell device.

4.3 Results and discussion

4.3.1 VO_x films characterization

XRD was used to assess the crystallinity of vanadium oxide thin films, as seen in Figure 4.2. On planar Si substrates, 20 nm-thick vanadium oxide thin films were deposited, and they were subsequently heated to 450 °C for 30 min while being exposed to ambient O_2, N_2, and vacuum atmospheres. When the temperature in the oxygen ambient climbs to 450 °C, five diffraction peaks corresponding to orthorhombic V_2O_5 (JCPDS No. 41-1426) are observed[18,19], indicating that V_2O_5 takes on a crystalline form. The film's favored orientation along the (001) plane is demonstrated by the prominent peak at 20.3°. V_2O_5's (200), (001), (101), (301), and (002) crystal planes are identified by their corresponding diffraction peaks at 15.3°, 20.3°, 21.7°, 31.0°, and 41.3°. After annealing in N_2 environment, one significant peak of (011)-oriented structure in the space group $p2_1/c$ was found, pointing to the presence of monoclinic VO_2 (M).

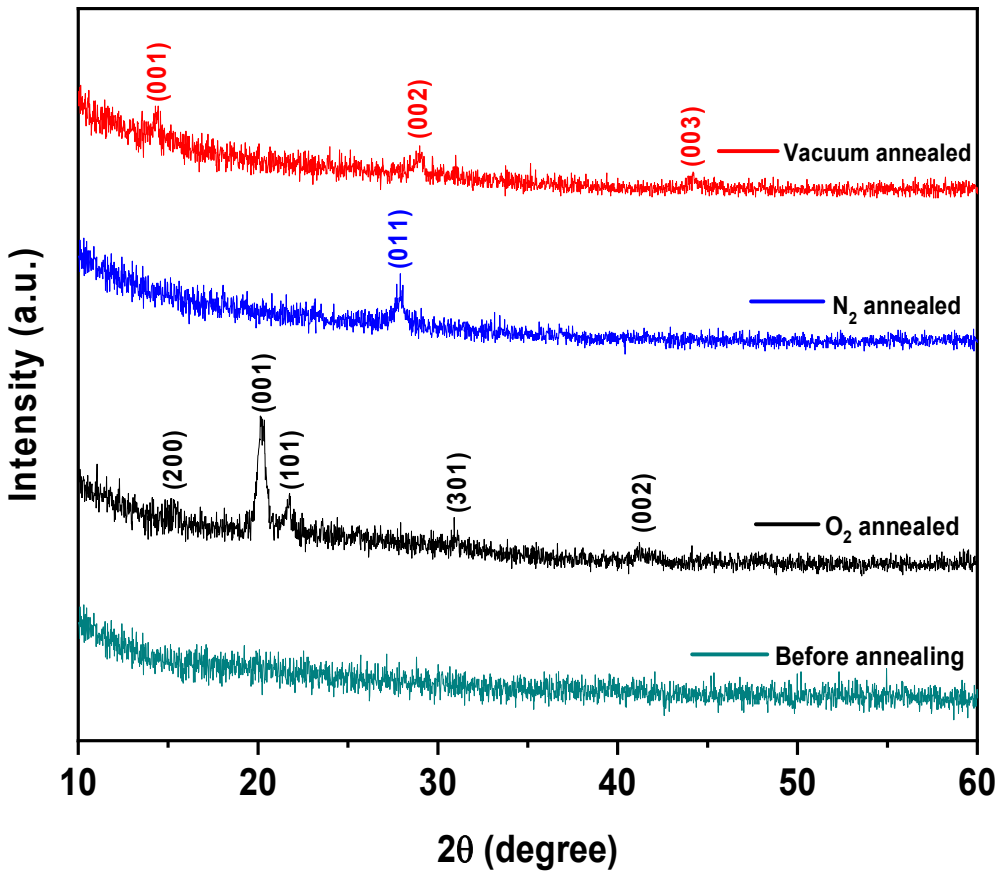

Figure 4.2 XRD pattern of vanadium oxide thin films annealed in O_2, N_2, and under vacuum at 450 °C.

After 450 degrees Celsius of vacuum annealing, another phase was formed with a diffraction analysis showing the (001), (002), and (003) crystalline planes of monoclinic VO_2 (B) with the space group C_2/m (JCPDS 01-081-2392), which corresponding the diffracted angles of 14.3, 28.9, and 44.0 degrees,

respectively. When annealed in environments with varying amounts of oxygen, distinct crystal forms have been seen. When annealing occurs in an environment with low ambient oxygen, the decomposition process of V_2O_5 becomes more prominent. The results of a prior investigation [19] using oxygen-deficient annealing atmospheres are in excellent accord with this propensity of decomposition into VO_2.

X-ray photoelectron spectroscopy (XPS) measurements were used to determine whether or not the creation of VO_2 is a result of the complete decomposition of V_2O_5 into VO_2. To track the stoichiometry and chemical alteration of the deposited 20-nm vanadium oxide (VO_x) films handled under various environmental conditions, the XPS photoemission spectra were examined. It appears that annealing alters the oxidation state of vanadium.[21] After Shirley background removal and fitting by Gaussian-Lorentzian convolution, Figure 4.3 (a-c) displays the V *2p* spectra of vanadium oxide films that were annealed in O_2, N_2, and under vacuum at 450 °C. The V *2p* core level may be tightly matched to two doublet peaks for oxygen annealing (Figure 4.3 (a)), with a peak area ratio of 2:1. The *2p* doublet of the V^{5+} cation is shown by the two prominent peaks at 517.4 eV and 524.9 eV. The occurrence of small peaks at 516.2 eV and 523.1 eV, which are identified as V^{4+} cations (as previously reported[17,22]), can be used to infer insufficient stoichiometry of V_2O_5. According to the composition study, the amount of V^{4+} was discovered to be 12%, which suggests that the TMO film has a limited number of oxygen vacancies. As a result, it may be written as V_2O_{5-x}. In the case of nitrogen annealing (Figure 4.3 (b)), the peaks at 517.6 and 525.0 eV are often attributed to V^{5+}, but the other V $2p_{3/2}$ and V $2p_{1/2}$ peaks located at 516.6 and 523.7 eV, respectively, can be attributed to V^{4+} oxidation states. Unexpectedly, the V^{4+} cation quantity grows noticeably and even begins to surpass V^{5+}, with the atomic ratio of V^{4+} to V^{5+} changing to around 1.46:1, indicating reducing effects on the sample. The tiny V $2p_{3/2}$ and V $2p_{1/2}$ peaks situated at 515.3 and 522.5 eV can be used to pinpoint the extremely few oxygen vacancies that come from V^{3+}(which has metallic properties).[23,24] XPS examination reveals the existence of V^{4+} (V $2p_{3/2}$ at 516.2 eV and V $2p_{1/2}$ at 524 eV) and V^{3+} (V $2p_{3/2}$ at 514.7 eV and V $2p_{1/2}$ at 522.4 eV) after vacuum annealing (Figure 4.3 (c)). The site of the V^{3+} peak agrees well with earlier research.[25,26] The XPS results clearly show that annealing VO_x films in a vacuum has the tendency to convert V_2O_5 to VO_2 plus some V^{3+} oxidation states, with a molar ratio of V^{4+}: V^{3+} estimated and determined to be 3.3:1 from the area ratio of the fitted spectra of V *2p*. The stoichiometry of VO_x is nearly identical to that of VO_2 with oxygen vacancies; hence, it is designated as VO_{2-x}. When comparing VO_x films annealed in N_2 and in vacuum, we find that the latter has a substantially larger concentration of V^{3+} cations (representing oxygen deficiencies) than the former. From the XPS spectra, we can determine that samples annealed in nitrogen have a concentration of 6% oxygen deficiency, whereas those annealed in a vacuum have a concentration of 23%.

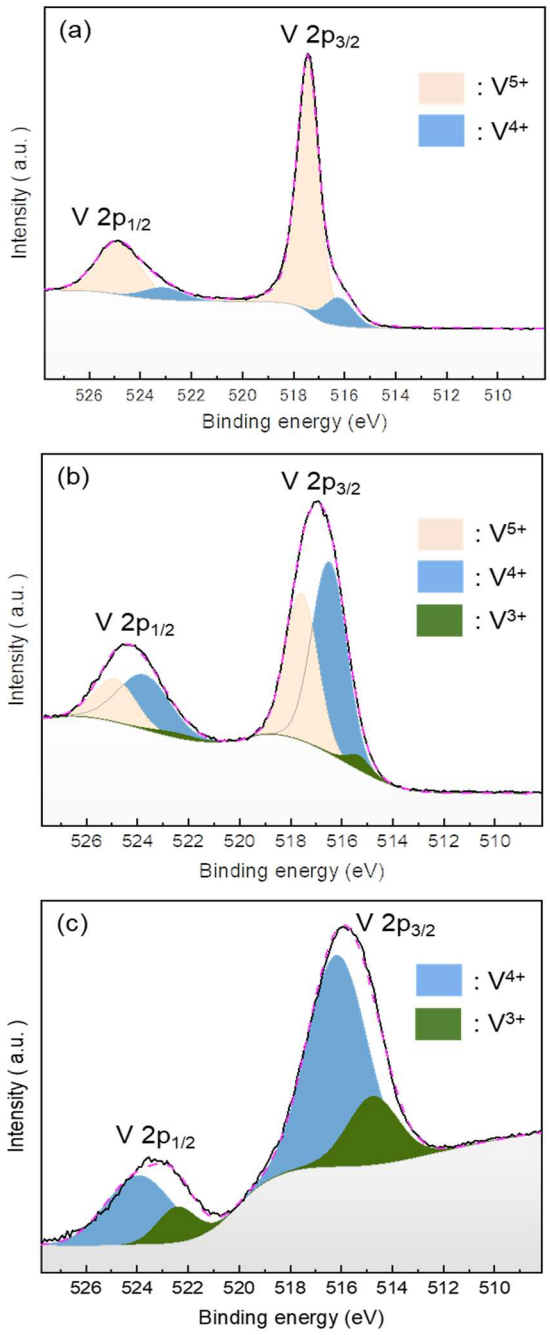

Figure 4.3 V *2p* core-level XPS spectra of VO_x thin-films annealed at 450 °C in (a) O_2, (b) N_2, and (c) under vacuum. The black solid line represents the experimental XPS spectra; the yellow, blue, and green areas are decomposed XPS spectra; the dashed purple line is the sum of all the decomposed XPS spectra.

Micrographs taken using a scanning electron microscope (SEM) reveal SiNWs with a mean size of 420 nm (Figure 4.4 (a,b)). For vanadium oxide-coated SiNWs, the corresponding SEM-EDS maps are displayed in Figure 4.5. The results unambiguously demonstrate the existence of vanadium along the NWs. The SiNWs are completely covered by the deposited TMO, as illustrated in Figure 4.5 (b), when the top and bottom points of the NW are compared. Despite the fact that the V and O atomic percentages

are lower at the bottom of NWs than they are at the top, one may be certain that the spinning solution is able to permeate the gaps between NWs and produce a thinner layer on the bottom of the SiNWs.

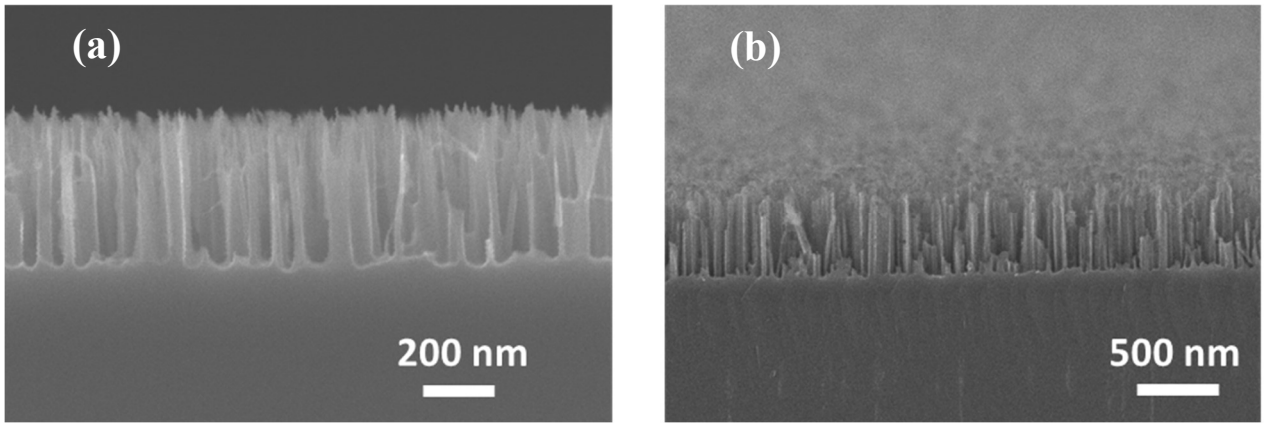

Figure 4.4 SEM images of the fabricated Si nanowires, (a) cross-sectional and (b) 15˚ tilted side view of SiNWs arrays.

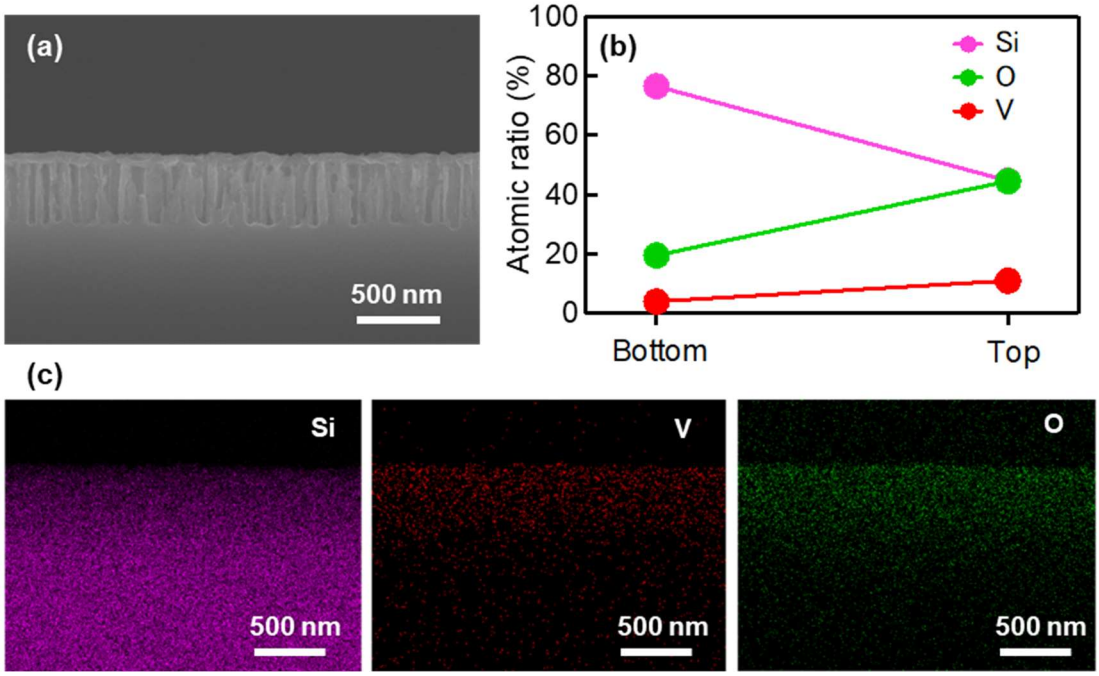

Figure 4.5 (a) SEM image of vanadium oxide deposited radially on Si NWs, (b) EDS-atomic ratio, and (c) EDS elemental mapping for vanadium oxide after being spun on Si NWs.

4.3.2 Solar cells' performance after utilizing VO_x films

Fabrication of Schottky junction-type solar cells employing n-Si NWs coated with annealed vanadium oxide (VO_x) under varied environmental circumstances was studied, as was the efficacy of the annealed VO_x film as a hole-injection layer. The suggested band diagram of an VO_x/n-SiNWs heterojunction is shown in Figure 4.6 (a). Figure 4.6 (b) depicts the J-V characteristic curve of several solar cells with an Ag/VO_x/n-SiNWs/Ti/Ag structure illuminated with 100 mW cm^{-2} of light. VO_x layer creation was followed by 450 degrees Celsius of annealing in oxygen, nitrogen, and vacuum.

With J_{SC}= 21.88 mA cm^{-2}, V_{OC} = 0.3 V, and FF = 0.31, the solar cell with VO_x annealed in vacuum had the highest power conversion efficiency (PCE) of the three devices. With these parameters (J_{SC} = 13.2 mA cm^{-2}, V_{OC} = 0.3 V, and FF = 0.27) the efficiency of the nitrogen-annealed solar cell was 48% lower.

The reason why VO_x annealed under vacuum is more efficient than VO_x annealed in nitrogen is because, as demonstrated by XPS research, V^{4+} cations are more prevalent under vacuum conditions and the ratio of V^{3+} oxidation states is greater than in nitrogen. This is due to a reduction in the hole injection barrier at the anode/Si interface caused by the addition of additional states close to the Fermi level in the gap in the VO_{2-x} film.[27] In other words, the shallow defect states produced by oxygen deficiency in the band gap assist the passage of holes via the VO_{2-x} layer. It is apparent that the greater oxygen deficiencies contributed to the larger J_{SC} for the sample annealed in vacuum compared to that annealed in N_2, with almost no change in the open circuit voltage. The relatively low FF value of the device utilizing VO_x annealed under vacuum is attributed to the low R_{sh} of 74.419 Ω cm^{-2}. As shown in the inset of Figure 4.6 (b), the efficiency of the solar cell based on vanadium oxide annealed in oxygen was incredibly low, with the value of J_{SC} significantly reduced; V_{OC}, and FF were small, indicating a poor connection between silicon and V_2O_{5-x}, which is almost an insulating material. These findings show that the band alignment in this instance is unsuitable because there are no pathways for the holes to follow through the V_2O_{5-x} to reach the anode, which prevents the optically produced charges from transferring readily. As a result, the device operates like a circuit with resistor elements.

The reflectance spectra of 20 nm-VO_x film annealed at 450 °C in various conditions are shown in Figure 4.6 (c), and Figure 4.6 (d) displays the Tauc plots used to determine the associated optical band gaps. The J_{SC} value of the solar cell is negatively impacted by the amount of visible light that VO_x films annealed in oxygen reflect compared to those annealed in nitrogen or in vacuum. The reflectance for vacuum-annealed and nitrogen-annealed films were comparable and rather weak, with a minor advantage for vacuum-annealed film. For oxygen, nitrogen, and vacuum-annealed VO_x films, the computed band gaps were 2.48 eV, 2.88 eV, and 3.24 eV, respectively.

According to the XPS discussion above, the variation in VO_x stoichiometry is most likely the cause of the band gap variation. Similar broad band gaps have been reported in the semiconducting phase of VO_2.[28–30] With such a big band gap, it would be expected that a significant hole-injection barrier would form at the VO_{2-x}/Si contact, degrading the PCE. The higher PCE caused by electron transportation to the silicon's valence band may be caused by the existence of gap states in VO_{2-x} films close to the Fermi level. At the VO_{2-x}/Si interface, the gap states appeared to be aligned with the Si valence band, which in turn creates hole-transporting pathways from Si to the anode via the TMO layer by injecting electrons into the hole sites in the Si valence band.[31]

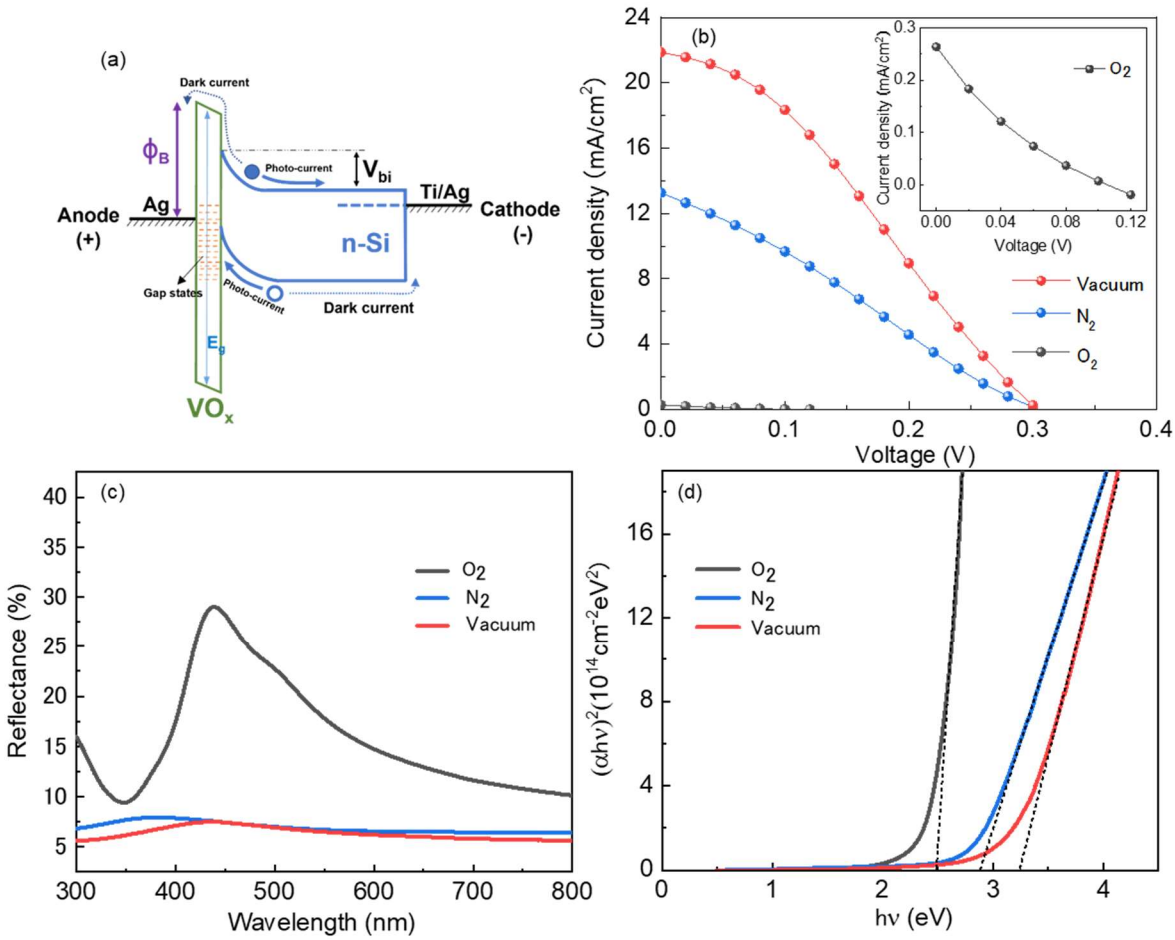

Figure 4.6 (a) Proposed band diagram for VO_x/n-Si solar cell: V_{bi} of Si and (E_g, E_f, amount of gap states) of VO_x vary according to VO_x stoichiometry and deposition conditions. (b) *J*-V characteristics for VO_x/n-SiNWs solar cells, with the TMOs films annealed in O_2, N_2, and under vacuum at 450 °C. The inset shows the *J*-V curve for an O_2 annealed VO_x-based device. (c) Reflectance spectra in the UV-vis region for VO_x films annealed in O_2, N_2, and under vacuum at 450 °C. (d) Tauc plots showing the corresponding optical band gaps.

4.3.3 Vacuum-annealing temperature optimization

Four distinct solar cells were made by annealing the VO_x layer under vacuum (VO_{2-x}(B)) at 200 °C, 300 °C, 400 °C, and 500 °C in an effort to find the best temperature for VO_x films and enhance hole-injection capabilities. The device containing the VO_{2-x}(B) layer annealed at 400 °C exhibits the highest performance, with J_{SC} = 22.2 mA cm^{-2}, V_{OC} = 0.36 V, and FF = 0.55, yielding a PCE of 4.5%. This is seen from the *J-V* curve in Figure 4.7. When the sample crystallizes more, the series resistance decreases and the antireflection property improves, however when the annealing temperature approaches 500 °C, the PCE tends to decline to a lower value due to a decrease in V_{OC} and FF. This could be because VO_2 (B) has a propensity to shift phases and irreversibly transform into rutile VO_2 (R) when its temperature reaches ≥450 °C. [19,32] The characteristic of oxygen deficiencies existing in the bandgap that permit hole

injection to the anode may be lost due to the metallic behavior of VO_2 (R). The FF value was also affected by the decline of R_{sh} to 74.8 Ω/cm² from 1292 Ω/cm² at 400 °C.

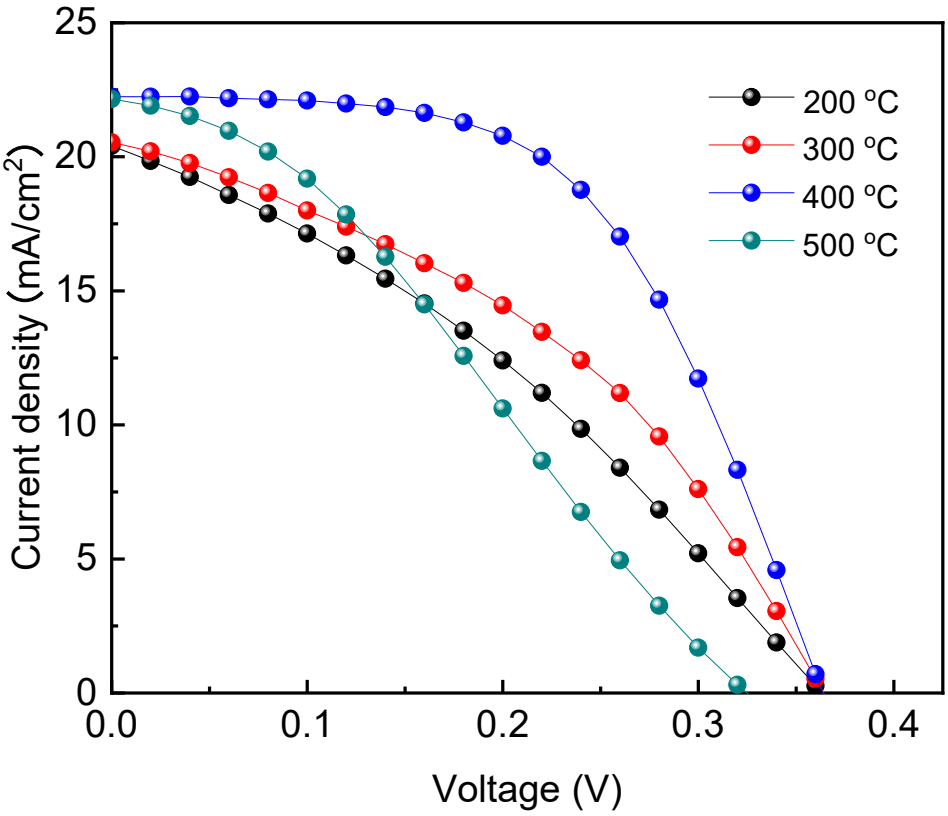

Figure 4.7 *J*-V characteristics of VO_{x-2}/n-SiNWs solar cells, with the TMOs films annealed under vacuum at 200, 300, 400, and 500 °C.

4.3.4 VO_{2-x} film thickness optimization

TMO thickness was a critical manufacturing variable, and solar cell devices with varied VO_x thicknesses were created and annealed at 400 °C under vacuum. The *J-V* characteristics and external quantum efficiency (EQE) of the manufactured devices are shown in Figure 4.8 (a, b). Table 4.1 provides a list of the measured solar cell parameters. The EQE results indicate the photocarrier production in 10-, 15-, 25-, and 50-nm VO_{2-x}(B)-based devices occurs throughout a wide wavelength range (300 - 1100 nm).

The drop in the 50-nm device curve can be attributed to the fact that the thicker layers block some light from reaching the Si, resulting in a fall in J_{SC}. The J_{SC} values derived from EQE are quite similar to the *J-V* curve measurements. Only the device based on a 5 nm layer has a much lower J_{SC} value. The poor performance of the 5-nm VO_{2-x}(B)-derived device may be attributable to the fact that the VO_{2-x}(B) film was deposited in the shape of tiny islands rather than a uniform film, which would have an effect on charge segregation at the interfaces and the passivation of the SiNW surfaces. When vacuum-depositing V_2O_5, Chen et al. noticed a similar pattern of activity.[33]

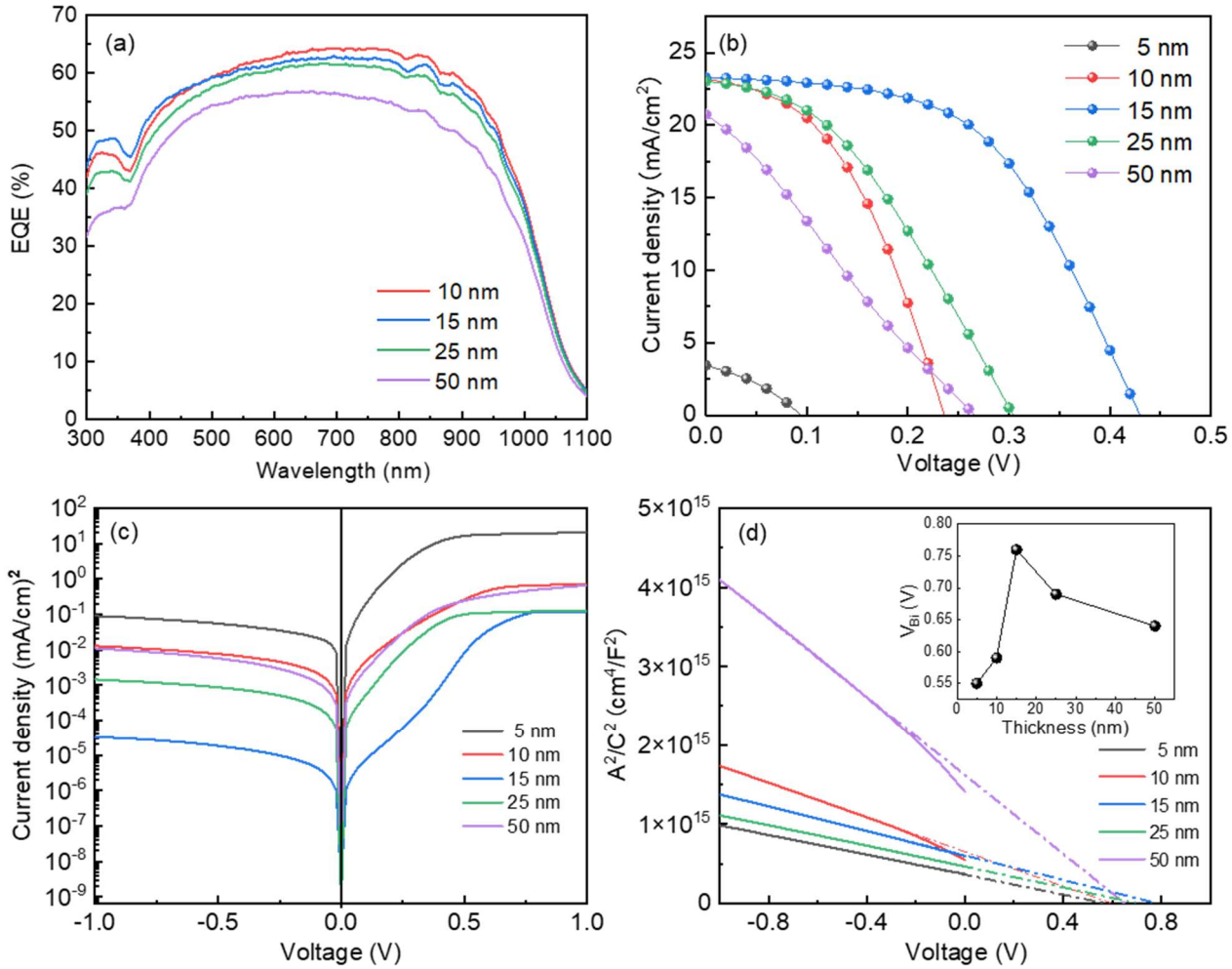

Figure 4.8 (a) EQE of VO_{x-2}/n-SiNWs solar cells with varying thicknesses of VO_{x-2}. (b) *J*-V characteristics for VO_{x-2}/n-SiNWs solar cells, with the TMOs films deposited at different thicknesses and annealed under vacuum at 400 °C. (c) Current-voltage characteristics in the dark of VO_{x-2}/n-SiNWs devices with different VO_{x-2} thicknesses. (d) Capacitance-voltage measurements of the same devices. The inset shows the dependence of V_{bi} on the thickness of VO_{x-2} films.

The strong relationship between VO_{2-x}(B) thickness and open-circuit voltages suggests that the ability of VO_{2-x}(B) to passivate silicon's surface changes with thickness. A rise in VO_{2-x}(B) layer thickness from 5 nm to 15 nm was accompanied by an increase in V_{OC} value. This enhancement can be attributed to the better coverage of thicker films for the NWs and the improvement of charge separation at the junction interface as a result of saturation current J_o decreasing, which can be seen from the dark current-voltage characteristics shown in Figure 4.8 (c). On increasing the thickness to more than 15 nm, V_{OC} tends to decrease, which might be attributable to a reduction in the built-in voltage (V_{bi}) caused by the increased thickness, as shown in the Mott-Schottky plot in Figure 4.8 (d). Therefore, the recombination rate increases once again for samples that are thicker than 15 nm. This is because the process of transferring electrons (dark current) from Si to VO_{2-x}(B) thicker films is easier than it is in devices with a 15-nm feature size. The greatest performance was obtained with a solar cell utilizing a

15 nm-VO_x layer annealed under vacuum at 400 °C, with J_{SC} = 23.27 mA cm^{-2}, V_{OC} = 0.43 V, and FF = 0.52, resulting in a power conversion efficiency of 5.28%.

Table 4.1 Solar cell parameters of Ag/VO_{2-x}(B)/n-SiNWs/Ti/Ag structure utilizing different thicknesses of the hole-injection layer.

VO_{2-x}(B) Thickness (nm)	Voc (V)	Jsc (mA/cm²)	Jsc^{EQE} (mA/cm²)	FF	η%	R_s (Ω cm²)	R_{sh} (Ω cm²)
5	0.09 ± 0.004	3.55 ± 0.03	N/A	34 ± 1.4	0.11 ± 0.15	8.46 ± 0.04	66.7 ± 1.3
10	0.23 ± 0.01	23.19 ± 0.1	23.1	44 ± 2.7	2.25 ± 0.22	5.92 ± 0.02	94.8 ± 3.4
15	0.43 ± 0.02	23.27 ± 0.5	23.2	52 ± 3.3	5.28 ± 0.31	7.01 ± 0.03	345.8 ± 9.2
25	0.29 ± 0.01	23.10 ± 0.2	22.6	39 ± 1.9	2.69 ± 0.28	7.51 ± 0.06	131.7 ± 5.4
50	0.26 ± 0.01	20.70 ± 0.6	20.6	25 ± 1.5	1.37 ± 0.33	11.64 ± 0.03	22.5 ± 1.6

Jsc^{EQE}: Photocurrent density calculated from the integration of EQE curves.

3.4.5 Stability comparison between VO_x and PEDOT:PSS

The stability of the hybrid solar cell made of n-SiNWs and PEDOT:PSS was compared to that of the VO_{2-x}(B)/n-SiNWs device. Over the course of 14 days at 60% humidity at room temperature, the PCE of the two devices was measured. The VO_{2-x} device demonstrated more stability than PEDOT:PSS: as a result of Voc & FF improvement and R_s reduction, its normalized PCE increased every day and finally exceeded unity, i.e., increased by around 10%.

It is probable that the oxidation of silver electrodes in air is responsible for the extraordinary gradual improvement of the VO_{2-x}-derived device, in which the work function of silver improved from 4.3 eV to 5.0 eV when the silver layer was oxidized, hence enhancing FF and the performance of the solar cell.[33,34] After two days, J_{SC} remained unchanged but V_{OC} increased from 0.42 V to 0.44 V, probably due to a drop in saturation current accompanied by oxidation of the silver electrodes. It was anticipated that the PEDOT:PSS device would exhibit a comparable improvement, however the quick deterioration of the produced cell more than offset the observed electrode improvement. The device made with PEDOT:PSS was unable to hold even 80% of its initial PCE two days after manufacture. The primary cause of this abrupt fall in PCE is a decline in FF, which exhibited a 70% decrease after 300 hours. According to Norrman et al., oxygen absorption, which results in PEDOT:PSS phase separation, is the primary cause of the PEDOT:PSS deterioration.[12] After 14 days, the PEDOT:PSS device's PCE had dropped by 88%, making it abundantly evident that the TMO device, which had reached PCE = 5.69%, was better than the hybrid device, which had achieved PCE = 1.36%.

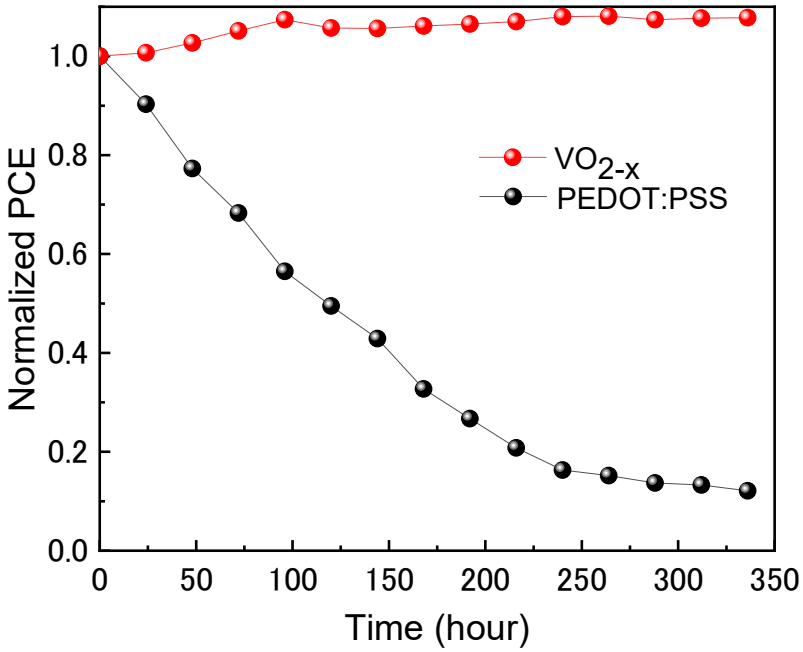

Figure 4.9 Normalized PCE decay of PEDOT:PSS and VO_{x-2}/Si nanostructure solar cell devices.

4.4 Summary

In conclusion, a variety of vanadium oxides films with distinct crystal structures and stoichiometries were successfully grown on a silicon substrate by a straightforward solution processing method, then annealed in a variety of environments. Solar cells made with a anode/VO_x/n-SiNWs/cathode showed that the VO_x layer performs a hole-injection role, which allows for easier separation and collection of photogenerated carriers in the presence of oxygen deficiencies (where vacuum-annealed films performed best). The V_{bi} computations showed that the passivation of SiNWs by the TMOs films might be improved by adjusting the deposition conditions. For maximum cell efficiency, a VO_x layer of 15 nm in thickness should be deposited and annealed at 400 °C in a vacuum. When compared to SiNWs-based solar cells that used PEDOT:PSS films, the VO_x film-based cells were more stable.

4.5 References

[1] V. Shrotriya, G. Li, Y. Yao, C.W. Chu, Y. Yang, Transition metal oxides as the buffer layer for polymer photovoltaic cells, Appl. Phys. Lett. 88 (2006) 1–4. https://doi.org/10.1063/1.2174093.

[2] S. Murase, Y. Yang, Solution processed MoO 3 interfacial layer for organic photovoltaics prepared by a facile synthesis method, Adv. Mater. 24 (2012) 2459–2462. https://doi.org/10.1002/adma.201104771.

[3] H. You, Y. Dai, Z. Zhang, D. Ma, Improved performances of organic light-emitting diodes with metal oxide as anode buffer, J. Appl. Phys. 101 (2007) 1–4. https://doi.org/10.1063/1.2430511.

[4] J. Meyer, K. Zilberberg, T. Riedl, A. Kahn, Electronic structure of Vanadium pentoxide: An efficient hole injector for organic electronic materials, J. Appl. Phys. 110 (2011). https://doi.org/10.1063/1.3611392.

[5] L.J. Meng, R.A. Silva, H.N. Cui, V. Teixeira, M.P. dos Santos, Z. Xu, Optical and structural properties of vanadium pentoxide films prepared by d.c. reactive magnetron sputtering, Thin Solid Films. 515 (2006) 195–200. https://doi.org/10.1016/J.TSF.2005.12.061.

[6] A. Bouzidi, N. Benramdane, A. Nakrela, C. Mathieu, B. Khelifa, R. Desfeux, A. Da Costa, First synthesis of vanadium oxide thin films by spray pyrolysis technique, Mater. Sci. Eng. B. 95 (2002) 141–147. https://doi.org/10.1016/S0921-5107(02)00224-6.

[7] M.E.A. Warwick, R. Binions, Chemical vapour deposition of thermochromic vanadium dioxide thin films for energy efficient glazing, J. Solid State Chem. 214 (2014) 53–66. https://doi.org/10.1016/J.JSSC.2013.10.040.

[8] S. Beke, S. Giorgio, L. Korösi, L. Nánai, W. Marine, Structural and optical properties of pulsed laser deposited V2O5 thin films, Thin Solid Films. 516 (2008) 4659–4664. https://doi.org/10.1016/J.TSF.2007.08.113.

[9] N. Özer, Electrochemical properties of sol-gel deposited vanadium pentoxide films, Thin Solid Films. 305 (1997) 80–87. https://doi.org/10.1016/S0040-6090(97)00086-2.

[10] K. Zilberberg, S. Trost, H. Schmidt, T. Riedl, Solution processed vanadium pentoxide as charge extraction layer for organic solar cells, Adv. Energy Mater. 1 (2011) 377–381. https://doi.org/10.1002/aenm.201100076.

[11] I. Hancox, L.A. Rochford, D. Clare, M. Walker, J.J. Mudd, P. Sullivan, S. Schumann, C.F. McConville, T.S. Jones, Optimization of a high work function solution processed vanadium oxide hole-extracting layer for small molecule and polymer organic photovoltaic cells, J. Phys. Chem. C. 117 (2013) 49–57. https://doi.org/10.1021/jp3075767.

[12] K. Norrman, M. V. Madsen, S.A. Gevorgyan, F.C. Krebs, Degradation patterns in water and oxygen of an inverted polymer solar cell, J. Am. Chem. Soc. 132 (2010) 16883–16892. https://doi.org/10.1021/ja106299g.

[13] A. Seemann, H.J. Egelhaaf, C.J. Brabec, J.A. Hauch, Influence of oxygen on semi-transparent organic solar cells with gas permeable electrodes, Org. Electron. 10 (2009) 1424–1428. https://doi.org/10.1016/J.ORGEL.2009.08.001.

[14] T. Subramani, J. Chen, Y. Kobayashi, W. Jevasuwan, N. Fukata, Highly Air-Stable Solution-Processed and Low-Temperature Organic/Inorganic Nanostructure Hybrid Solar Cells, ACS Appl. Energy Mater. 2 (2019) 2637–2644. https://doi.org/10.1021/acsaem.8b02218.

[15] Y. Kobayashi, T. Terauchi, S. Sumi, Y. Matsushita, Carrier generation and electronic properties of a single-component pure organic metal, Nat. Mater. |. 16 (2017). https://doi.org/10.1038/NMAT4768.

[16] G. Ma, R. Du, Y. Cai, C. Shen, X. Gao, Y. Zhang, F. Liu, W. Shi, Solar Energy Materials and Solar Cells Improved power conversion e ffi ciency of silicon nanowire solar cells based on transition metal oxides, Sol. Energy Mater. Sol. Cells. 193 (2019) 163–168. https://doi.org/10.1016/j.solmat.2019.01.010.

[17] L. Zhang, C. Jiang, C. Wu, H. Ju, G. Jiang, W. Liu, C. Zhu, T. Chen, V2O5 as Hole Transporting Material for Efficient All Inorganic Sb2S3 Solar Cells, ACS Appl. Mater. Interfaces. 10 (2018) 27098–27105. https://doi.org/10.1021/acsami.8b09843.

[18] H. Jiang, H. Chen, Y. Wei, J. Zeng, H. Liu, Y. Zhang, H. Wu, Biotemplate-mediated structural engineering of rod-like V 2 O 5 cathode materials for lithium-ion batteries, (2019). https://doi.org/10.1016/j.jallcom.2019.02.118.

[19] F. Xia, L. Yang, B. Dai, Z. Yang, L. Xu, G. Gao, C. Sun, Z. Song, V. Ralchenko, J. Zhu, Thermal transition behaviors of vanadium pentoxide film during post-deposition annealing, Surf. Coatings Technol. 405 (2021) 126637. https://doi.org/10.1016/j.surfcoat.2020.126637.

[20] Z.A. Umar, N. Ahmed, R. Ahmed, M. Arshad, M. Anwar-Ul-Haq, T. Hussain, M.A. Baig, Substrate temperature effects on the structural, compositional, and electrical properties of VO2 thin films deposited by pulsed laser deposition, Surf. Interface Anal. 50 (2018) 297–303. https://doi.org/10.1002/SIA.6368.

[21] S. Rathi, I.Y. Lee, J.H. Park, B.J. Kim, H.T. Kim, G.H. Kim, Postfabrication annealing effects on insulator-metal transitions in VO2 thin-film devices, ACS Appl. Mater. Interfaces. 6 (2014) 19718–19725. https://doi.org/10.1021/am5046982.

[22] L.G. Gerling, S. Mahato, A. Morales-Vilches, G. Masmitja, P. Ortega, C. Voz, R. Alcubilla, J. Puigdollers, Transition metal oxides as hole-selective contacts in silicon heterojunctions solar cells, Sol. Energy Mater. Sol. Cells. 145 (2016) 109–115. https://doi.org/10.1016/j.solmat.2015.08.028.

[23] C. Rameshan, M.L. Ng, A. Shavorskiy, J.T. Newberg, H. Bluhm, Water adsorption on polycrystalline vanadium from ultra-high vacuum to ambient relative humidity, Surf. Sci. 641 (2015) 141–147. https://doi.org/10.1016/j.susc.2015.06.004.

[24] C.Y. Kim, A.A. Escuadro, P.C. Stair, M.J. Bedzyk, Atomic-scale view of redox-induced reversible changes to a metal-oxide catalytic surface: VOx/α-Fe2O3(0001), J. Phys. Chem. C. 111 (2007) 1874–1877. https://doi.org/10.1021/jp067862s.

[25] Y. Ishige, T. Sudayama, Y. Wakisaka, T. Mizokawa, H. Wadati, G.A. Sawatzky, T.Z. Regier, M. Isobe, Y. Ueda, Interplay between Mott physics and Peierls physics in hollandite-type vanadates with a metal-insulator transition, Phys. Rev. B - Condens. Matter Mater. Phys. 83 (2011) 1–6. https://doi.org/10.1103/PhysRevB.83.125112.

[26] C.T. Wang, D.L. Lai, M.T. Chen, Synthesis of iron-doped vanadium-tin oxide nanocrystallites for CO gas sensing, Mater. Lett. 64 (2010) 65–67. https://doi.org/10.1016/j.matlet.2009.09.065.

[27] M.T. Greiner, M.G. Helander, W.M. Tang, Z. Bin Wang, J. Qiu, Z.H. Lu, Universal energy-level alignment of molecules on metal oxides, Nat. Mater. 11 (2012) 76–81. https://doi.org/10.1038/nmat3159.

[28] S. Choi, S.J. Chang, J. Oh, J.H. Jang, S. Lee, Electrical and Optical Properties of VO2 Polymorphic Films Grown Epitaxially on Y-Stabilized ZrO2, Adv. Electron. Mater. 4 (2018) 1–6. https://doi.org/10.1002/aelm.201700620.

[29] C. Zhang, C. Koughia, O. Güneş, J. Luo, N. Hossain, Y. Li, X. Cui, S.J. Wen, R. Wong, Q. Yang, S. Kasap, Synthesis, structure and optical properties of high-quality VO2 thin films grown on silicon, quartz and sapphire substrates by high temperature magnetron sputtering: Properties through the transition temperature, J. Alloys Compd. 848 (2020) 1–13. https://doi.org/10.1016/j.jallcom.2020.156323.

[30] A. Plecenik, T.C. Ramalho, P. Marcus, Reduction of V2O5 thin films deposited by aqueous sol – gel method to VO2 (B) and investigation of its photocatalyt ..., 2 (n.d.).

[31] J. Gao, C.L. Perkins, J.M. Luther, M.C. Hanna, H.Y. Chen, O.E. Semonin, A.J. Nozik, R.J. Ellingson, M.C. Beard, N-type transition metal oxide as a hole extraction layer in PbS quantum dot solar cells, Nano Lett. 11 (2011) 3263–3266. https://doi.org/10.1021/nl2015729.

[32] S. Zhang, J. Fu, Q. Su, L. Wu, X. Li, In Situ Characterization on Thermal Transitions of VO2(B): Toward VO2(R) and V2O3, Rare Met. Mater. Eng. 45 (2016) 1374–1380. https://doi.org/10.1016/S1875-5372(16)30116-3.

[33] C.P. Chen, Y.D. Chen, S.C. Chuang, High-performance and highly durable inverted organic photovoltaics embedding solution-processable vanadium oxides as an interfacial hole-transporting layer, Adv. Mater. 23 (2011) 3859–3863. https://doi.org/10.1002/adma.201102142.

[34] D. Wang, N.K. Elumalai, M.A. Mahmud, M. Wright, M.B. Upama, K.H. Chan, C. Xu, F. Haque, G. Conibeer, A. Uddin, V2O5 -PEDOT: PSS bilayer as hole transport layer for highly efficient and stable perovskite solar cells, Org. Electron. 53 (2018) 66–73. https://doi.org/10.1016/j.orgel.2017.10.034.

Chapter 5. The effect of VO_x as a hole-injection layer on the current transport and photovoltaic performance of a Schottky junction based on Si nanopencils

5.1 Pencil-shaped silicon nanowires (SiNPs)

It could be inferred from the V_{OC} values of Ag/VO_{2-x}/n-SiNWs device that the deposited VO_{2-x} film on SiNWs is not conformal, as the value of V_{OC} in case of Ag/VO_x/planar n-Si device was considerably higher as shown in Figure 5.1. To maintain the light trapping feature of NWs along with the high V_{OC} value achieved with the planar Si, pencil-shaped silicon nanowires (SiNPs) were proposed as an alternative surface structure. The innovative synthesis approach of colloidal lithography followed by inductively coupled plasma reactive ion etching (ICP-RIE) yields high-quality pencil-shaped SiNWs that are homogeneous, asymmetrical, dense, and precisely positioned. Large-area and low-cost fabrication are challenging to perform with traditional photolithography, hence colloidal lithography has advantages for industrial mass production.

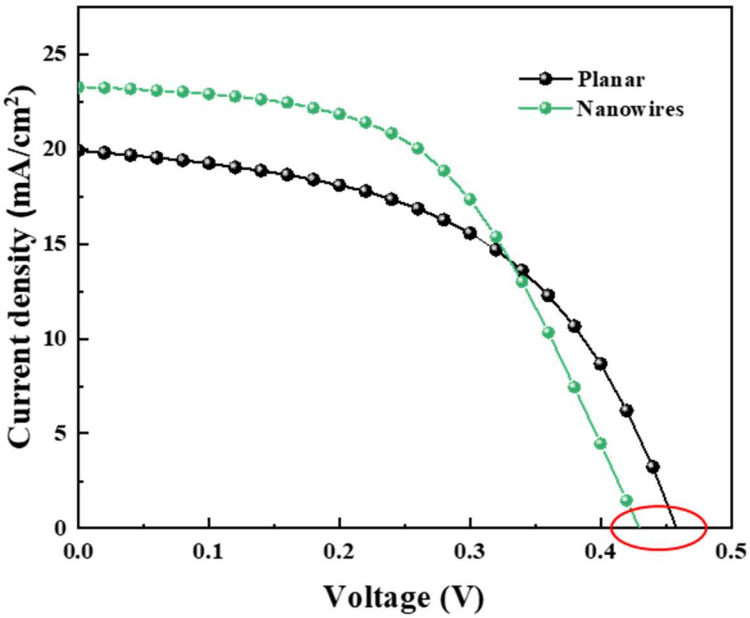

Figure 5.1 *J-V* characteristics for Ag/VO_{2-x}/n-SiNWs and Ag/VO_{2-x}/planar n-Si solar cells.

Experimenters have paid close attention to metal-semiconductor Schottky diodes because the electrical properties of their structures can be altered by adding an interlayer between metal and semiconductor. In this situation, interface layer thickness has a significant impact on device performance, in addition to the formation and properties of the interface states. There is a lack of adequate in-depth knowledge on the transport processes and junction parameters associated with VO_x at Schottky junction. The most important parameter of the junction is the barrier height which is a crucial characteristic that controls the behavior of electrical transport over VO_x-embedded Schottky

junction and the overall behavior of any device. The development of electrical switches and sensor devices often relies on engineering the barrier height.

In the present chapter, VO_{2-x} thin films were deposited using solution processing technique followed by vacuum annealing on a pencil-shaped silicon nanowires synthesized using colloidal lithography to investigate its photovoltaic performance. The functionality of Ag/n-Si Schottky diode affected by the presence of a VO_{2-x} film will be discussed. DC electrical measurements were taken as a function of both temperature and applied voltage to investigate its electronic characteristics and pinpoint its functioning conduction mechanisms.

5.2 Experimental

5.2.1 Silicon nanopencils fabrication technique

Utilizing a wafer of n-type CZ c-Si (100) (1.0-10.0 Ω cm, 280-μm thickness), SiNP structures were produced using a colloidal lithography and ICP-RIE technique. Colloidal silica particles, in the shape of spheres and measuring 300 nm in diameter, were purchased from a supplier. Aminopropyltriethoxysilane or allyltrimethoxysilane was used to make the silica surface hydrophobic before the particles were submerged in the solution. After positioning the silicon substrates in a Langmuir-Blodgett trough, the silica particles were disseminated in a combination of 80% chloroform and 20% ethanol on the trough's surface. There was self-assembly of silica particles at the air-water contact, forming a monolayer. Once the silicon substrate was lifted out of the sub-phase water at a rate of 5 mm/min, the mono-layer of silica particles could be transferred to the wafer's surface. Finally, plasma etching with RF power of 1500 W was carried out utilizing an ICP dry etcher (Tokyo Electron ME-510 I) and CHF_3/Cl_2 gases at a pressure of 1.0 Pa. Over the course of the dry etching process, the silica was gradually eliminated, leaving behind sharp pencil tips.

5.2.2 Fabrication of Ag/VO_{2-x}/n-Si Schottky junction

A precursor solution was made up of 0.02 milliliters of Vanadium(V) oxytriisopropoxide (VOTIP) diluted in 3 milliliters of isopropanol (IPA) (99.9%). This solution was spun at 3000 rpm onto the substrate for 60 seconds. During the spin-coating process, the precursor solution converted into non-stoichiometric V_2O_5 by interacting with ambient water vapor.[21] The samples were then annealed under vacuum in a tube furnace at 400 °C and pressure of 0.15 Torr to get a non-stoichiometric vanadium dioxide film (VO_{2-x}) with a thickness of 15nm. Afterwards, sputtering was used to deposit Ti/Ag (50 nm/250 nm) and Ag grid (250 nm) electrodes on the back and front of the samples.

5.3 Results and discussion

5.3.1 Ag/VO_{2-x}/n-SiNP/Ti/Ag Schottky solar cell

SiNPs structure is successfully fabricated as shown in Figure 5.2 which displays scanning electron microscopy (SEM) images of the SiNPs from a variety of angles. SiNPs have a height of 500 nm and a pitch of 300 nm, as seen in the cross-sectional view in Figure 5.2 (b). The reflectance data of both planar Si and SiNPs after removing their superficial oxide layer are shown in Figure 5.3 (a). The planar surface displays the typical flat shape of Si. In comparison to the planar silicon substrate, whose reflectance fluctuates from 75% to 30% throughout the wavelength range of 300-1100 nm, the SiNPs sample had significant lower reflectance which remained steady between zero and five percent in the visible region, because of its superior light-trapping properties.

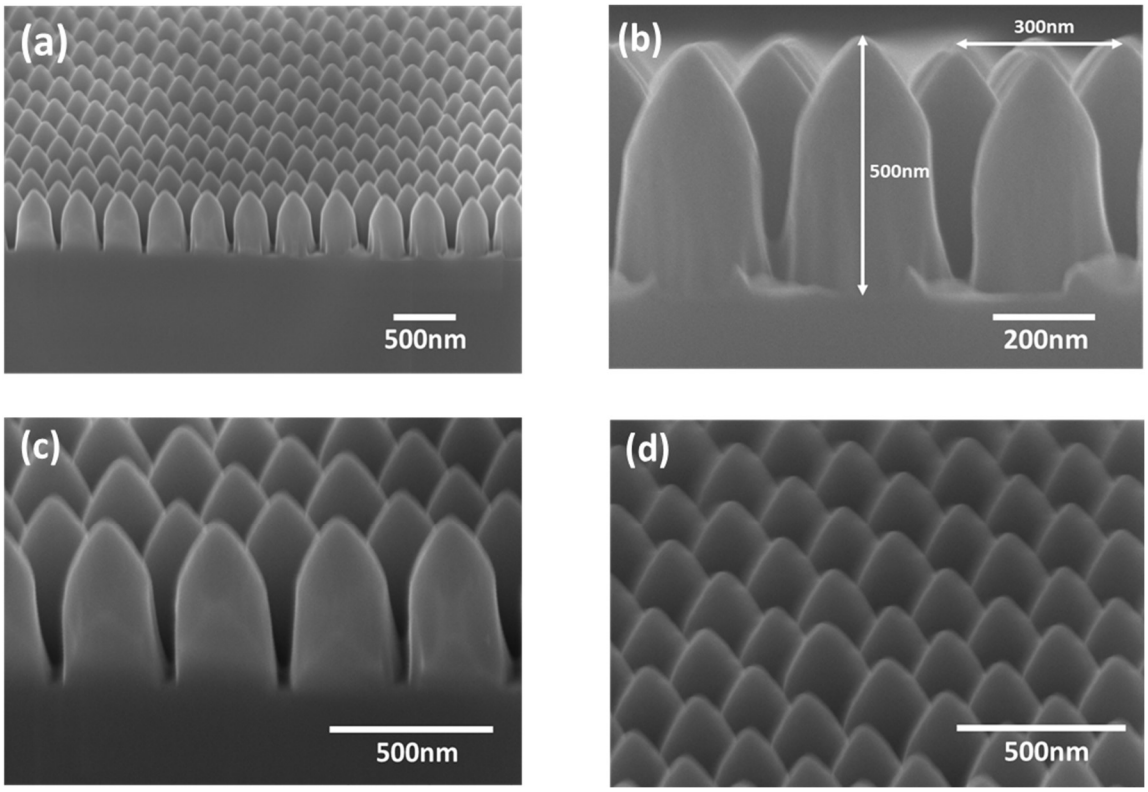

Figure 5.2 (a) 30°-tilted SEM image view of SiNPs. (b) Nanopencils dimensions in a cross-sectional SEM image. (c), and (d) SiNPs at a 20° tilt.

A combination of increased surface area, numerous total internal reflections inside a single nanopencil and robust light scattering within the nanopencil arrays contribute to the high anti-reflectivity of SiNP arrays.

Planar n-Si and n-SiNPs were deposited with 15 nm of substoichiometric vanadium dioxide (VO_{2-x}) thin film to create Ag/VO_{2-x}/n-Si/Ti/Ag Schottky junction solar cells.

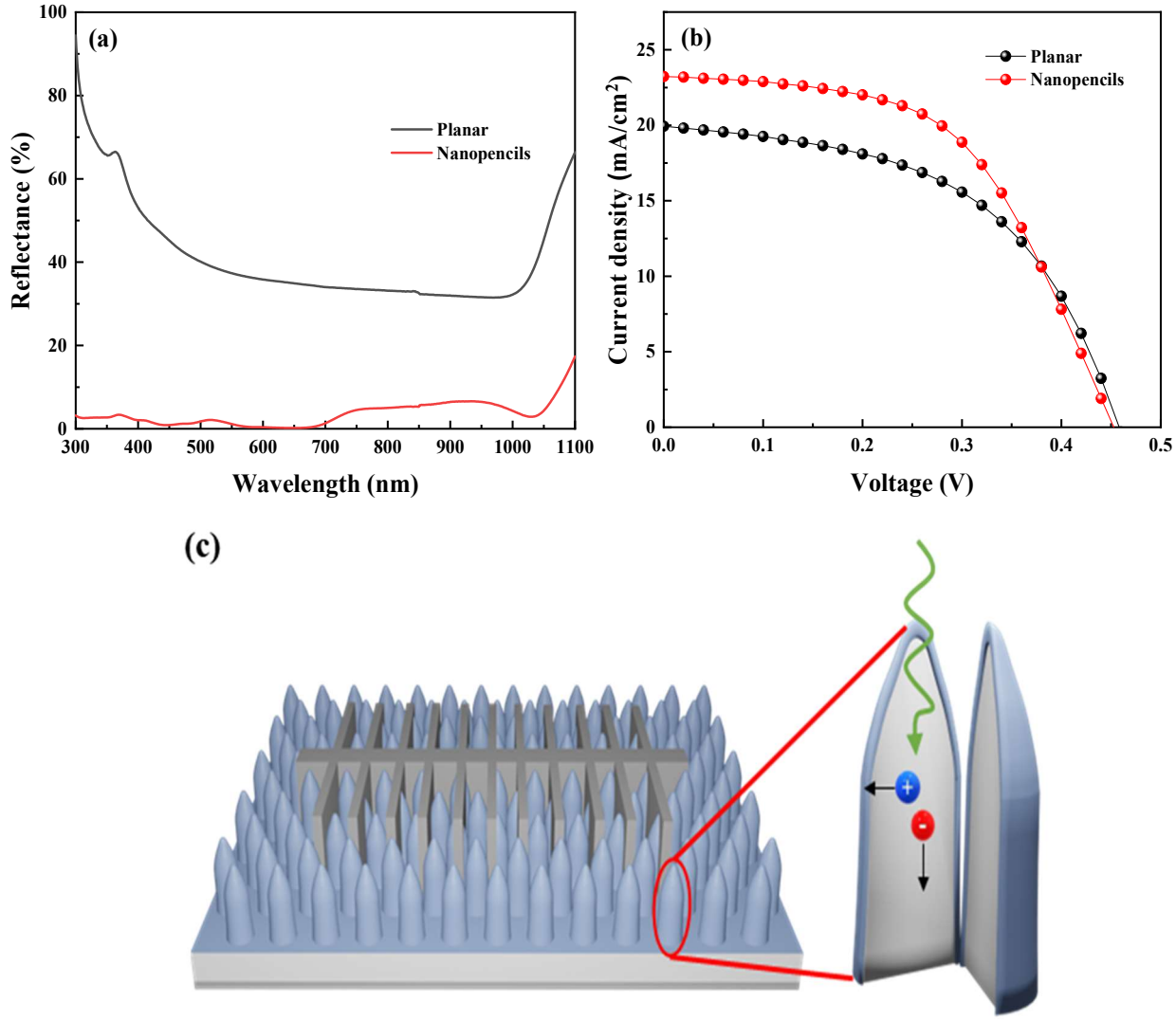

Figure 5.3 (a) Reflectance spectroscopy in the UV-Vis-NIR range for planar Si and Si nanopencil samples. (b) *J-V* characteristics for Ag/VO_{2-x}/n-SiNPs and Ag/VO_{2-x}/planar n-Si solar cells. (c) Schematic view of anode/VO_{2-x}/n-SiNPs/cathode solar cell and a cross-section of VO_{2-x}/n-SiNP junction.

Lowering the barrier for hole injection at the anode/Si interface is a side effect of the incorporation of additional states at the Fermi level in the band gap of the VO_{2-x} film. This means that the shallow defect states introduced into the band gap by oxygen deficiencies play a crucial role in the transit of holes via the VO_{2-x} layer.[1] The *J-V* characteristic curve of Ag/VO_{2-x}/n-Si/Ti/Ag solar cells under 100 mW cm^{-2} illumination is shown in Figure 5.3 (b). With a short circuit current density (J_{SC}) of 23.22 mA cm^{-2}, open circuit voltage (V_{OC}) of 0.45 V, and fill factor (FF) of 0.54, the SiNPs-based device achieved a conversion efficiency of 5.6%, which is outperforming the planar Si-derived device which only exhibited 4.7%. V_{OC} value was found to be slightly lower with the SiNPs device compared to those obtained with planar device which indicates that the surface recombination in SiNPs-derived device still comparable to the planar one. On the other hand, the solar cells with SiNPs had a much higher J_{SC} than planar devices because the high surface-to-volume ratio of the SiNPs allows for greater light trapping and junction area,

which in turn generates more photocurrent. This suggests the metal oxide layer deposited on SiNPs has superior coverage and passivation properties compared to those placed on SiNWs.

5.3.2 Conduction mechanisms through Ag/VO_{2-x}/n-SiNPs Schottky diode

To understand the cell properties, we investigated the diode properties. The temperature-dependent current-voltage characteristics of the Ag/VO_{2-x}/n-SiNPs/Ti/Ag Schottky junction diode are shown in Fig 5.4 where a substantial quantity of information pertaining to junction attributes, including the saturation current (I_0), ideality factor (n), and classification of the transport conduction mechanism can be obtained. The electrical response displays characteristics of rectification and the current increases as the temperature rises. This result indicates that Ag/VO_{2-x} /n-SiNPs Schottky junction can be used as efficient solar cell materials because they display both p-type and n-type characteristics under the action of an external electric field. At a fixed bias, the rectification ratio (RR) is calculated as RR=$(I_f/I_r)_v$, where I_f and I_r are the forward and reverse currents, respectively. At a constant biasing potential of ±1 V, the RR of the current junction increases from 314.5 to 730.9 while the temperature is varied from 298 to 358 K.

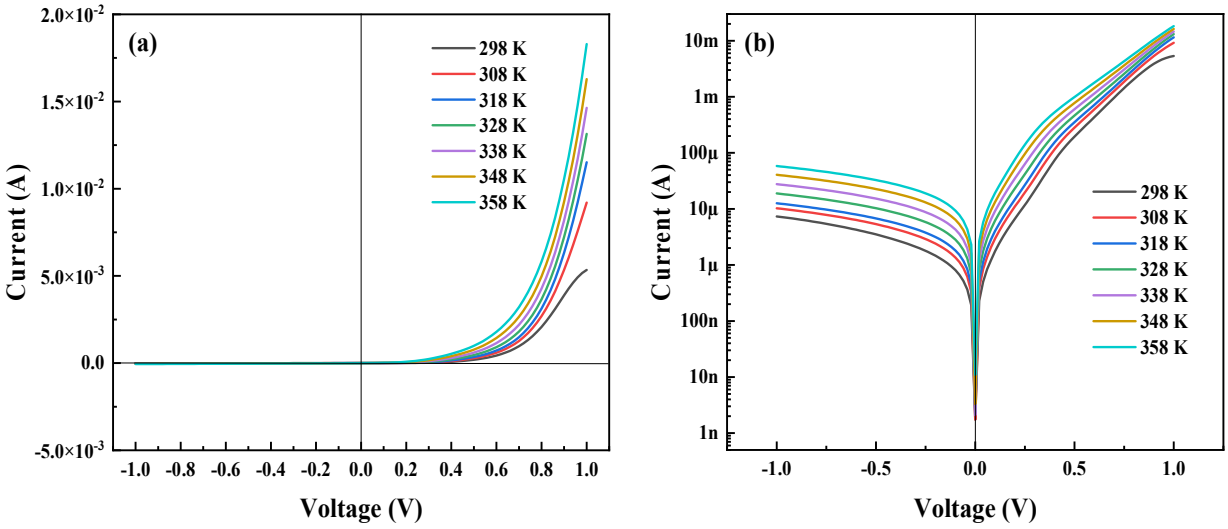

Figure 5.4 (a) Ag/VO_{2-x}/n-SiNPs/Ti/Ag Schottky junction dark current-voltage characteristics at various temperatures. (b) Forward and reverse bias semi-logarithmic current–voltage (I–V) characteristics of the same device.

The fluctuation of the forward current's natural logarithm with applied voltage for the Ag/VO_{2-x} /n-SiNPs/Ti/Ag Schottky junction at temperature range (298-358 K) is shown in Figure 5.5. The current fluctuates exponentially at relatively low applied voltages, but at high voltages, a downward curve becomes visible owing to the presence of different conduction mechanisms through the junction. The data can be divided into three zones, with zone **I** occurring at $V \leq 0.12$ V, zone **II** occurring between 0.12 V and 0.3 V, and zone **III** occurring at $V \geq 0.3$ V.

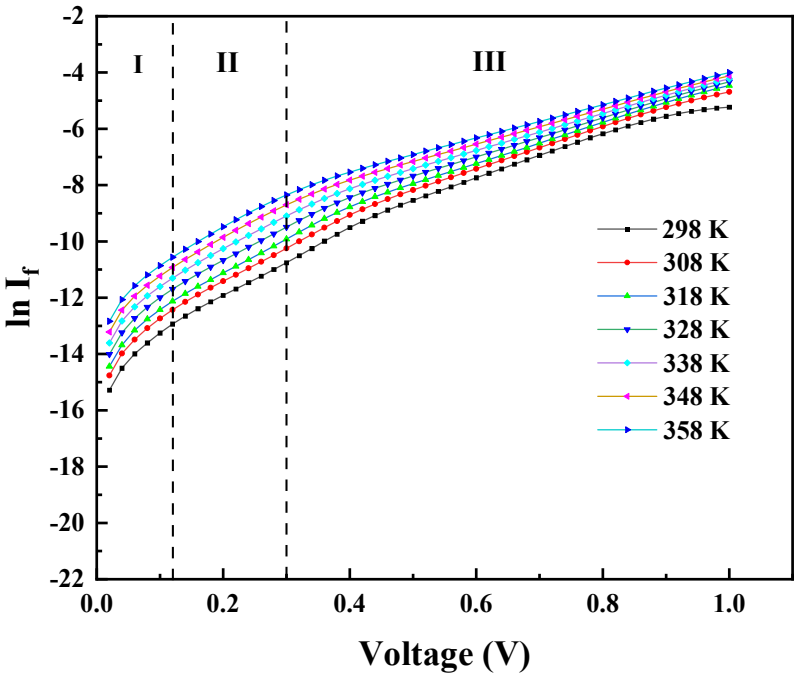

Figure 5.5 Variation of (ln I_f) with forward bias voltage for VO_{2-x}/n-SiNPs Schottky junction at different temperatures.

The barrier height and ideality factor were determined using a linear fit to the straight-line segment of the ln(I)-V plot throughout the voltage range of 0.01-0.12 V (zone **I**), as predicted from the theory of thermionic emission, which describes the current as:[2,3]

$$I = I_0 \left[\exp\left(\frac{qV}{nk_BT}\right) - 1\right] \qquad (5.1)$$

where q is the electronic charge, V is the voltage that is being applied across the device, n is the diode ideality factor, k_B is the Boltzmann's constant, T is the absolute temperature, and I_0 is the saturation current which is stated using thermionic theory as:

$$I_0 = AA^*T^2 \exp\left(\frac{-q\varphi_b}{k_BT}\right) \qquad (5.2)$$

where A represents the effective area of the device (The top electrode was used to determine that the active area of the device was 0.13 cm^{-2}), A^* represents the Richardson constant with a value 120 A cm^{-2} K^{-2} for n-Si[4], and φ_b represents the effective barrier height when there is no bias that can be calculated using the following formula:

$$\varphi_b = \frac{k_BT}{q} ln\left(\frac{AA^*T^2}{I_0}\right) \qquad (5.3)$$

n may be calculated using Eq. (5.1) as follows:

$$n = \frac{q}{k_B T}\frac{dV}{dln(I)} \qquad (5.4)$$

Estimated values of the ideality factor and the barrier height as a function of temperature are displayed in Figure 5.6 (a). As the temperature rises, the ideality factor declines as the barrier height rises. The lateral heterogeneity of the barrier height is responsible for this phenomenon. Even in the most meticulously constructed diodes, the variations in the barrier height are always present.[5,6] Since electrons can overcome lower barriers at low temperatures, current transport will be mostly controlled by current passing through regions of lower barrier height. More electrons have enough energy to cross the higher barrier as temperature rises. Thus, when temperature and bias voltage rise, the dominating barrier height will rise as well.[7] As a result, the current passes through the lower barrier height and current transport is dominated by a higher ideality factor.

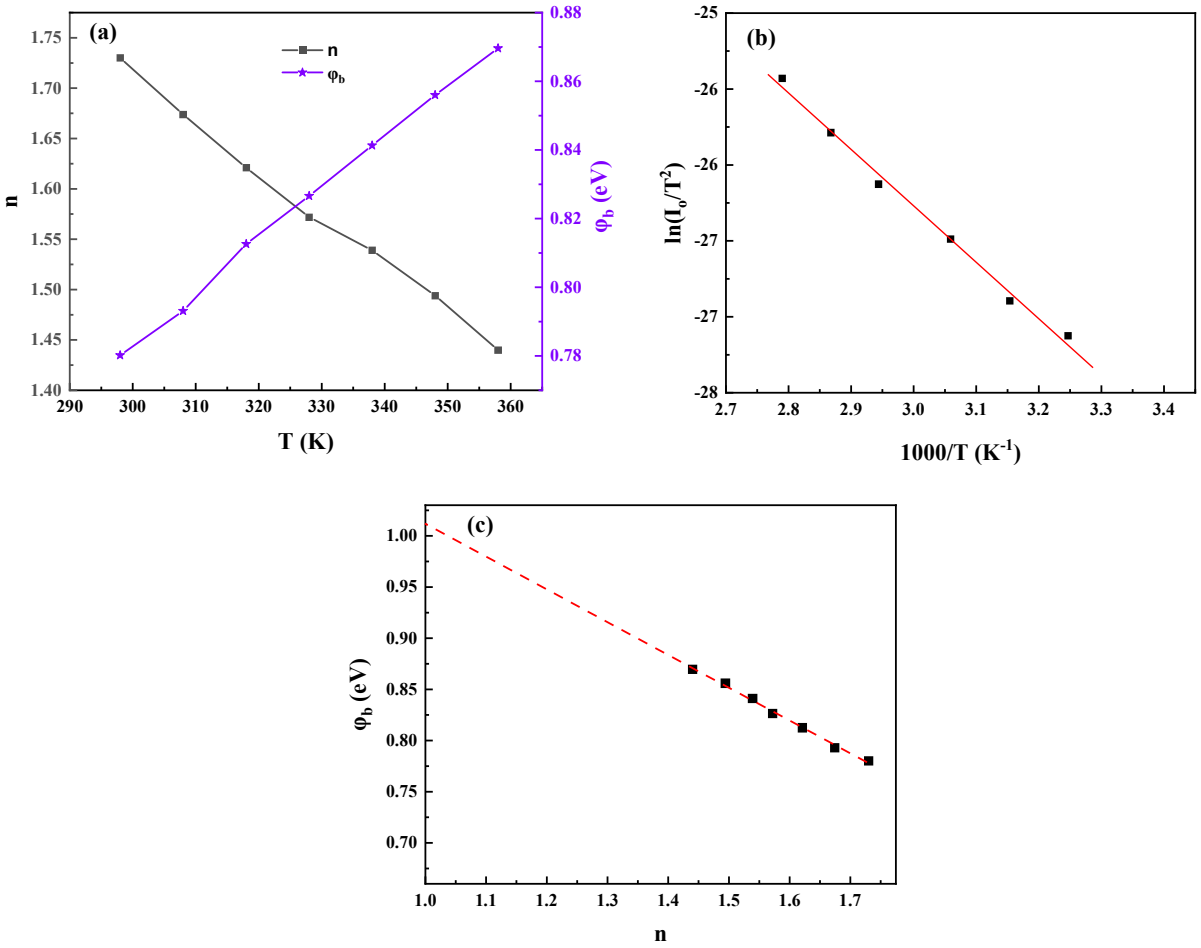

Figure 5.6 (a) Temperature effects on the ideality factor (n) and barrier height (φ_b). (b) Conventional Richardson plot of Ag/VO_{2-x}/n-SiNPs/Ti/Ag diode. (c) Changes in barrier height as a function of the ideality factor.

The ideality factor is more than 1, confirming the device's less-than-perfect performance. The high likelihood of the image-force effect[8], the existence of interface states in SiO_2[9], and the tunneling process[10] may be possible causes for the deviation from ideal behavior. Ideality factor and barrier

height values of 1.73 and 0.78 eV were achieved at ambient temperature, which are better than those obtained by Mahato et al.[11] for an Au/V_2O_5/n-Si device (n = 2.04 and φ_b = 0.83 eV), in which the V_2O_5 layer was produced by thermal evaporation onto Si substrates. The relationship between ln (I_0/T^2) and T^{-1} is shown in Figure 5.6 (b) to verify that the thermionic emission mechanism is the working conduction mechanism in the low voltage area. Since a straight line was produced, it is certain that the thermionic mechanism is the dominating mechanism.

The relationship between the barrier height and the ideality factor for an Ag/VO_{2-x}/n-SiNPs Schottky junction diode is shown in Figure 5.6 (c). Straight lines are fitted to the experimental data. The value of homogeneous barrier height is obtained by extrapolating the straight line to an ideal diode with an ideality factor of 1. The homogeneous barrier height value is calculated to be 1.01 eV.

Nord suggested a means through which the barrier height of Schottky-barrier diodes may be calculated. In the extended forward bias area of the junction's I-V characteristics, the following function has been developed using a modification of Nord's method:[12,13]

$$F(V) = \frac{V}{2} - \frac{k_B T}{q} ln\left(\frac{I(V)}{AA^* T^2}\right) \qquad (5.5)$$

With this approach, the barrier height may be calculated using the following formula:

$$\varphi_b = F(V_{min}) + \frac{V_{min}}{2} - \frac{k_B T}{q} \qquad (5.6)$$

where $F(V_{min})$ is the lowest value of the Norde's function $F(V)$ and V_{min} is the voltage corresponds to the lowest value of Norde's function.

The Norde's function $F(V)$ of the Ag/VO_{2-x}/n-SiNPs Schottky diode is shown plotted against the voltage (V) in Figure 5.7. The values of the barrier height calculated using Norde's function at different temperatures are compared to that measured from the thermionic emission and inserted in Table 5.1. The barrier height calculated using Nord's formula is clearly comparable to that calculated using I-V characteristics.

Figure 5.8 (a) shows the double logarithmic relationship between forward current and voltage in zone II. The results showed a series of straight lines with slope ~ 2, indicating that space charge limited current (SCLC) governed by a single trap state is the dominating conduction mechanism. During the high forward biasing region, space charges are injected from n-SiNPs into the VO_{2-x} thin film, where the poor mobility of the film inhibits the charge's dynamics. The Mott-Gurney equation may be used to define the space charge limited current:[14,15]

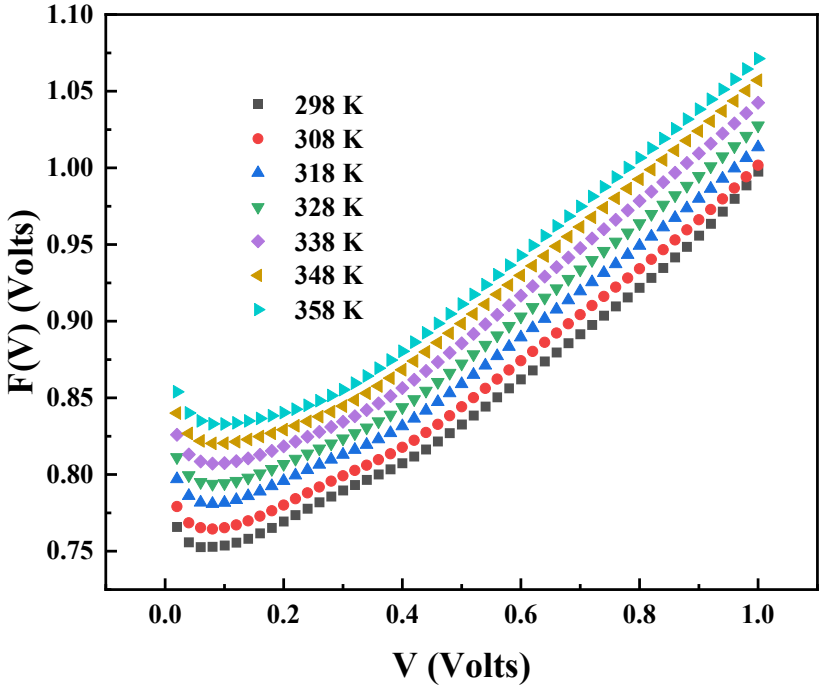

Figure 5.7 Voltage dependency of $F(V)$ for Ag/VO_{2-x}/n-SiNPs/Ti/Ag diode at various temperatures.

Table 5.1 Electrical performance analysis of a manufactured Ag/VO_{2-x}/n-SiNPs Schottky diode.

T (K)	*I-V*		Nord's
	$\varphi_{b\ (eV)}$	n	$\varphi_{b\ (eV)}$
298	0.78	1.73	0.77
308	0.79	1.67	0.78
318	0.81	1.62	0.80
328	0.83	1.57	0.81
338	0.84	1.54	0.83
348	0.86	1.49	0.84
358	0.87	1.44	0.85

$$I = \frac{9}{8}\varepsilon_r\varepsilon_0\mu A\frac{V^2}{d^3}\frac{N_c}{N_t}\exp\left(\frac{-E_t}{k_BT}\right) \qquad (5.7)$$

where N_c is the effective density of states at the edge of the conduction band, ε_0 is the permittivity of free space, ε_r is the relative permittivity of the used semiconductor, d is the semiconductor thickness, μ is the

charge carrier mobility, and N_t is the total trap density at single energy level E_t, which is positioned below the conduction band edge. The slope of the ln(I) vs 1/T plot at various forward voltages is shown in Figure 5.8 (b), and was used to calculate E_t. An average value of 0.36 eV was found for E_t in the calculations. Herein, E_t's position is lower than that determined for Al/MoO_x/n-Si/Al device.[15]

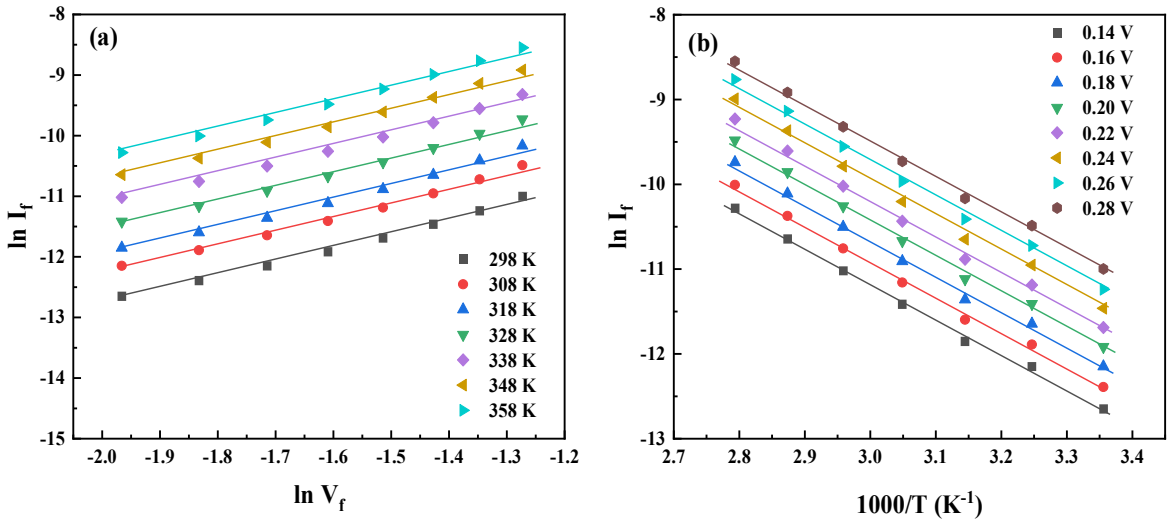

Figure 5.8 (a) The Ag/VO_{2-x}/n-SiNPs/Ti/Ag diode's ln(I_f) vs ln(V_f) change with temperature in zone **II**, and (b) the temperature dependency of ln(I_f) at various voltages.

To interpret the conduction mechanism at forward voltages ≥ 0.3 V (zone **III**), linear relation between ln(I_f) and ln(V) of the fabricated Ag/VO_{2-x}/n-SiNPs Schottky junction diode is plotted as depicted in Figure 5.9, exhibiting a slope value greater than 2. It was found that the current has the dependency on the voltage in the form I α $V^{2.6}$, which indicates that the SCLC, which is regulated by the distribution of trap levels, is the working mechanism in this region. Injected charge carriers can get immobilized when they fill the voids of the generated trap levels, which may be impacted by the interfacial imperfections. As so, the current may be expressed as follows:[16]

$$I = \frac{q^{1-l} A \mu N_c}{d^{2l+1}} \left(\frac{\varepsilon_r \varepsilon_0 l}{N_t (l+1)}\right)^l \left(\frac{2l+1}{l+1}\right)^l V^{l+1} \qquad (5.8)$$

where N_t denotes the density of trapping states.

The concentration of traps per unit energy at an energy E below the edge of the conduction band P(E) is given by:[17]

$$P(E) = P_0 exp\left(\frac{-E}{k_B T l}\right) \qquad (5.9)$$

where P_0 denotes the trap density per unit energy range below the conduction band edge. Integrating Eq. (5.9) yields a rough estimate of the overall trap density, N_t, which is then given by:[18]

$$N_t = P_0 k_B T l \qquad (5.10)$$

At room temperature, the N_t values are calculated from Eq. 5.8 in average as 2.04 × 10^{20} m^{-3}. By substituting in Eq. (5.10) the average value of P_0 is approximately 4.96 × 10^{21} $eV^{-1}m^{-3}$.

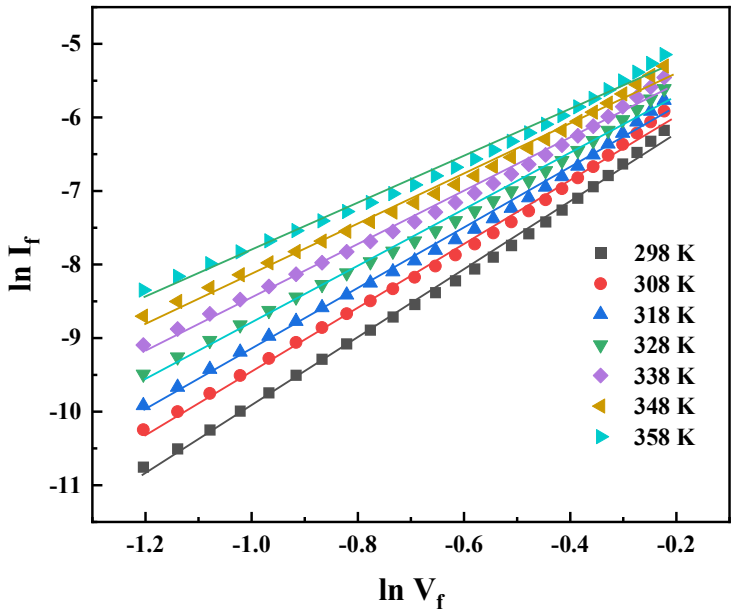

Figure 5.9 The Ag/VO_{2-x}/n-SiNPs/Ti/Ag diode's ln(I_f) vs. ln(V_f) change with temperature in zone **III**.

5.3.3 Dark C-V characteristics

Figure 5.10 displays the Mott-Schottky ($1/C^2$-V) plot for the Ag/VO_{2-x}/n-SiNPs Schottky diode at frequency 100 kHz in room temperature. It is assumed that the capacitance is related to voltage as:[19]

$$\frac{1}{C^2} = \frac{2(V_{bi} - V)}{qN_D\varepsilon_r\varepsilon_0} \qquad (5.11)$$

where N_D is the doping density (around 10^{15} cm^{-3} for 1.0 - 10.0 Ω cm n-Si[20]).

Using the x-intercept of the $1/C^2$-V plot, the built-in potential (V_{bi}) of the fabricated diode was determined to be 0.62 eV. The depletion region width (W_D) is determined by the following equation:[21]

$$W_D = \sqrt{\frac{2\varepsilon_r\varepsilon_0 V_{bi}}{qN_D}} \qquad (5.12)$$

The depletion width is estimated to be close to 896 nm, which is wider than the SiNP length (500 nm). All majority carriers are depleted from the nanopencil structure, and as a result, the nanopencil structure facilitates a more effective collection of light-generated minority carriers over a limited collection length than is possible with a planar structure that is thick enough to produce full light absorption across the solar spectrum.

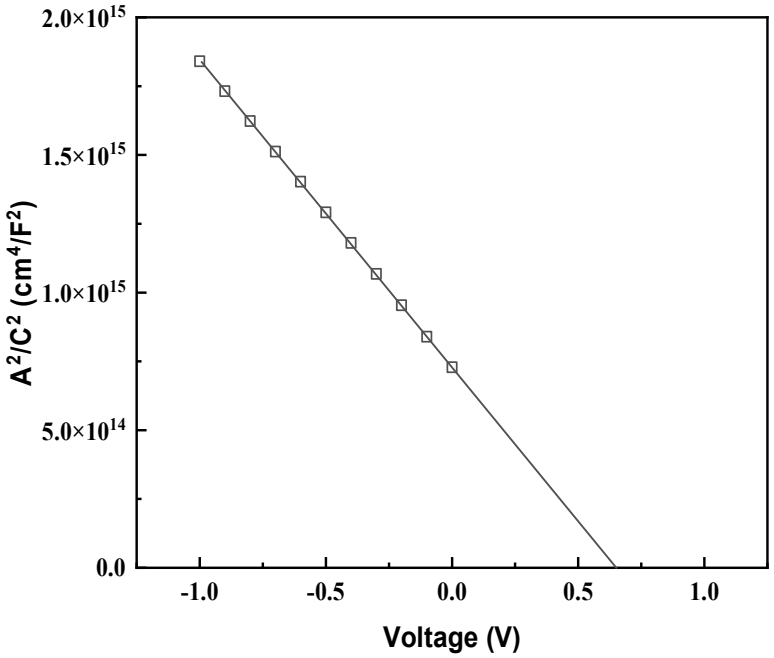

Figure 5.10 Mott-Schottky capacitance-voltage characteristics for Ag/VO_{2-x}/n-SiNPs device.

5.3.4 Stability comparison between VO_{2-x} and PEDOT:PSS utilized in SiNPs-based devices

The stability of the Ag/VO_{2-x}/n-SiNPs device was investigated and compared with that of the Ag/PEDOT:PSS/n-SiNPs hybrid solar cell. A PCE reading was taken daily for a month at 60% humidity and room temperature. The normalized PCEs over time for the two devices are shown in Figure 5.11.

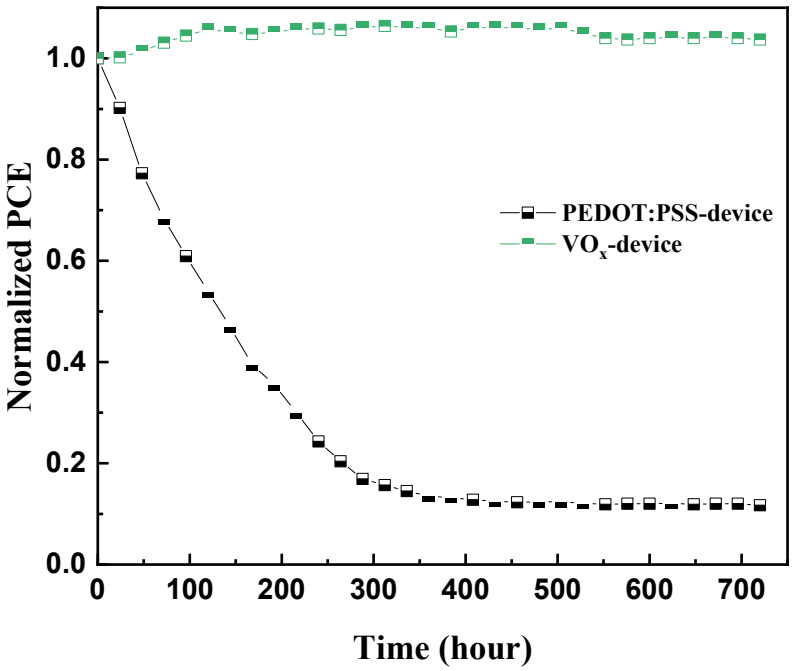

Figure 5.11 Normalized power-conversion efficiency (PCE) degradation for VO_{x-2}/n-SiNPs and PEDOT:PSS/n-SiNPs solar cells

Due to increases in V_{OC} and FF as well as decreases in R_S, the VO_{2-x} device's normalized PCE demonstrated more consistent performance than PEDOT:PSS, with its normalized PCE improved by around 6%. The work function of silver electrode increased from 4.3 eV to 5.0 eV when the silver layer was oxidized, which improves FF and the performance of the solar cell.[22,23]

After 72 hours, a slight increase of about 5 mV has been seen in V_{OC}, possibly attributable to the decrease in saturation current that accompanies the oxidation of silver electrodes in air. While the PEDOT:PSS device should have demonstrated a similar rise, the quick degradation in the fabricated hybrid cell was greater than the improvement attained by the electrode. Four days after manufacturing, the PEDOT:PSS-based device had lost more than 65% of its PCE where a 73% drop in FF was noticed, indicating that this rapid loss in PCE was mainly attributable to this drop in FF. Ultimately, a loss of 85% in PCE was observed in the PEDOT:PSS device after 30 days, making it abundantly clear that the VO_x device was superior to the hybrid device.

5.3.5 Downconverting effect by SiQDs

Figure 5.12 shows the current-voltage characteristic curves of Ag/VO_{2-x}/n-SiNPs Schottky solar cells with and without the SiQDs. Compared to the Si layers that may be benefit from the NRET process, the luminescent QDs have the benefit of absorbing a greater range of the solar spectrum in the ultraviolet area. However, the SiQDs' massive high-light-package emission may be effectively transferred from the nanocrystals via the RET process and reabsorbed by the neighboring Si layer. More carriers can be generated in the active layer via the two ways. Carrier separation and extraction through Ag/VO_{2-x}/n-SiNPs Schottky solar cells was much improved by employing this process, which indicated the significant contributive influence of adopting highly luminous QDs, which create more surplus carriers and mobility channels.

Table 5.2 summarizes the photovoltaic characteristics and shows that by using SiQDs, the current density is significantly increased. Using 1-octene-passivated SiQDs enhanced the current density from 23.22 mA cm^{-2} to 26.76 mA cm^{-2}. This improvement can be explained by the transmission of energy from SiQDs to the underlying Si nanostructures by RET and NRET.

Table 5.2 Solar cell properties of Ag/VO_{2-x}/n-SiNPs solar cell with and without the SiQD

	J_{sc} (mA cm^{-2})	V_{OC} (V)	FF	η (%)
w/o SiQDs	23.22	0.45	0.53	5.6
With SiQDs	26.76	0.45	0.50	6.0

It is not possible to take full advantage of the NRET phenomenon, as the SiQDs are placed on top of the VO_{2-x} layer, so there is a distance between the QDs and the Si surface which is the thickness of the VO_{2-x} layer. This structure is similar to what has been explained for the homojunction devise in Figure 3.11.

Since a thick coating of SiQDs might block sunlight from reaching the underlying device, which reduces the output current density, the ideal concentration was changed to provide the greatest PCE. To avoid interference with the underlying Si layer, which can be stimulated across a wide range of wavelengths from 400 to 1100 nm, SiQDs can only be excited by UV light up to 400 nm in wavelength. Therefore, QDs play a crucial function by converting this high-energy excitation into photons with a lower energy level, so reducing the energy loss due to thermalization. Reabsorption of the emitted light is reduced, and energy transfer is achieved for the vast majority of photons due to the large Stokes shift between the excitation and emission spectra.

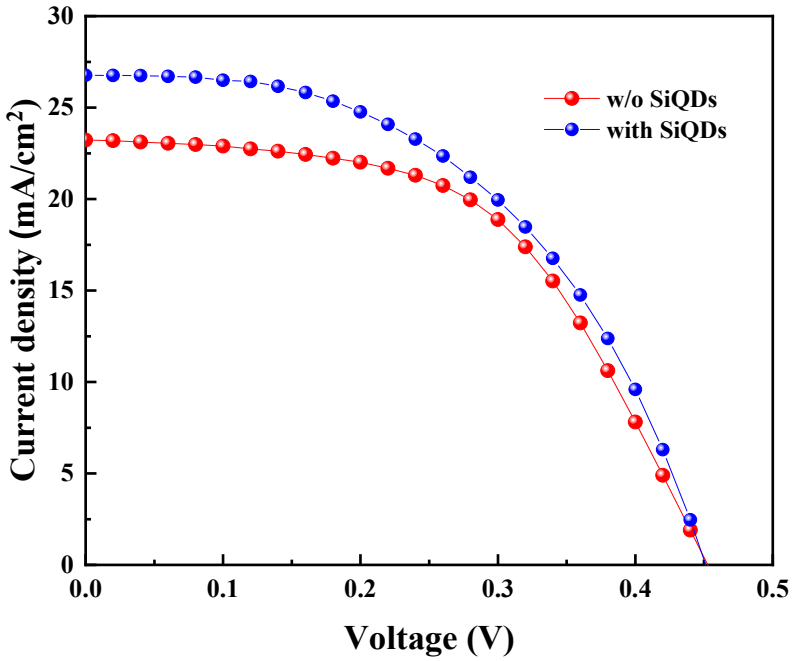

Figure 5.12 *J*-V curve under illumination of Ag/VO_{2-x}/n-SiNPs solar cell with and without SiQDs coating.

5.4 Summary

In summary, Ag/VO_{2-x}/n-SiNPs Schottky solar cell was made by depositing VO_{2-x} thin layer with thickness of 15 nm on n-SiNPs substrate which exhibited PCE of 5.6%. The SiNPs-based device outperformed its planar equivalent in solar cell performance due to its strong light-trapping feature. For temperatures between 298 and 358 K, the *I-V-T* curve demonstrated excellent Ag/VO_{2-x}/n-SiNPs diode performance, with substantial RR values of 314.5-730.9. Thermionic emission, space charge limited

current controlled by a single trap state, and space charge limited current regulated by a distribution of trap levels are the three primary transport mechanisms discovered in the forward bias regime based on the *I-V-T* measurements. Capacitance-voltage measurements at 100 kHz provide details on the depletion layer extending in the silicon side, with V_{bi} determined to be 0.62 V and the depletion width predicted to be roughly 900 nm.

5.5 References

[1] M. Abdelhameed, M.F. Abdelbar, M. Esmat, Nano Energy Hole-injection role of solution-processed thermally treated VOx thin films in Si nanowire-based solar cells, Nano Energy. 99 (2022) 107373. https://doi.org/10.1016/j.nanoen.2022.107373.

[2] S.M. Sze, K.K. Ng, Physics of Semiconductor Devices, John Wiley & Sons, Inc., Hoboken, NJ, USA, 2006. https://doi.org/10.1002/0470068329.

[3] R.T. Tung, Recent advances in Schottky barrier concepts, Mater. Sci. Eng. R Reports. 35 (2001) 1–138. https://doi.org/10.1016/S0927-796X(01)00037-7.

[4] T. Tunç, Ş. Altindal, İ. Uslu, İ. Dökme, H. Uslu, Temperature dependent current–voltage (I–V) characteristics of Au/n-Si (111) Schottky barrier diodes with PVA(Ni,Zn-doped) interfacial layer, Mater. Sci. Semicond. Process. 14 (2011) 139–145. https://doi.org/10.1016/j.mssp.2011.01.018.

[5] W.P. Leroy, K. Opsomer, S. Forment, R.L. Van Meirhaeghe, The barrier height inhomogeneity in identically prepared Au/n-GaAs Schottky barrier diodes, Solid. State. Electron. 49 (2005) 878–883. https://doi.org/10.1016/j.sse.2005.03.005.

[6] R.F. Schmitsdorf, Explanation of the linear correlation between barrier heights and ideality factors of real metal-semiconductor contacts by laterally nonuniform Schottky barriers, J. Vac. Sci. Technol. B Microelectron. Nanom. Struct. 15 (1997) 1221. https://doi.org/10.1116/1.589442.

[7] V. Janardhanam, H.-K. Lee, K.-H. Shim, H.-B. Hong, S.-H. Lee, K.-S. Ahn, C.-J. Choi, Temperature dependency and carrier transport mechanisms of Ti/p-type InP Schottky rectifiers, J. Alloys Compd. 504 (2010) 146–150. https://doi.org/10.1016/j.jallcom.2010.05.074.

[8] S.M. Lee, Y. Jang, J. Jung, J.H. Yum, E.S. Larsen, S.Y. Lee, H. Seo, C.W. Bielawski, H.-D. Lee, J. Oh, Crystalline BeO Grown on 4H-SiC via Atomic Layer Deposition: Band Alignment and Interface Defects, ACS Appl. Electron. Mater. 1 (2019) 617–624. https://doi.org/10.1021/acsaelm.9b00098.

[9] İ.Y. Erdoğan, Ö. Güllü, Silicon MIS diodes with Cr2O3 nanofilm: Optical, morphological/structural and electronic transport properties, Appl. Surf. Sci. 256 (2010) 4185–4191. https://doi.org/10.1016/j.apsusc.2010.01.122.

[10] J. Lee, T. Uhrmann, T. Dimopoulos, H. Bruckl, J. Fidler, TEM Study on Diffusion Process of NiFe Schottky and MgO/NiFe Tunneling Diodes for Spin Injection in Silicon, IEEE Trans. Magn. 46 (2010) 2067–2069. https://doi.org/10.1109/TMAG.2010.2040594.

[11] S. Mahato, D. Biswas, L.G. Gerling, C. Voz, J. Puigdollers, Analysis of temperature dependent current-voltage and capacitance-voltage characteristics of an Au/V 2 O 5 / n -Si Schottky diode, AIP Adv. 7 (2017) 085313. https://doi.org/10.1063/1.4993553.

[12] H. Norde, A modified forward I - V plot for Schottky diodes with high series resistance, J. Appl. Phys. 50 (1979) 5052–5053. https://doi.org/10.1063/1.325607.

[13] I.M. Soliman, M.M. El-Nahass, B.A. Khalifa, Characterization and photovoltaic performance of organic device based on AlPcCl/p-Si heterojunction, Synth. Met. 209 (2015) 55–59. https://doi.org/10.1016/j.synthmet.2015.06.016.

[14] P.A. Leighton, Electronic Processes in Ionic Crystals (Mott, N. F.; Gurney, R. W.), J. Chem. Educ. 18 (1941) 249. https://doi.org/10.1021/ed018p249.1.

[15] M.M. Makhlouf, H. Khallaf, M.M. Shehata, Impedance spectroscopy and transport mechanism of molybdenum oxide thin films for silicon heterojunction solar cell application, Appl. Phys. A. 128 (2022) 98. https://doi.org/10.1007/s00339-021-05215-z.

[16] M.A. Lampert, Volume-controlled current injection in insulators, Reports Prog. Phys. 27 (1964) 307. https://doi.org/10.1088/0034-4885/27/1/307.

[17] Ş. Karataş, C. Temirci, M. Çakar, A. Türüt, Temperature dependence of the current–voltage characteristics of the Al/Rhodamine-101/p-Si(100) contacts, Appl. Surf. Sci. 252 (2006) 2209–2216. https://doi.org/10.1016/j.apsusc.2005.03.222.

[18] E.H. Rhoderick, Metal-semiconductor contacts, IEE Proc. I Solid State Electron Devices. 129 (1982) 1. https://doi.org/10.1049/ip-i-1.1982.0001.

[19] J. Tang, K.W. Kemp, S. Hoogland, K.S. Jeong, H. Liu, L. Levina, M. Furukawa, X. Wang, R. Debnath, D. Cha, K.W. Chou, A. Fischer, A. Amassian, J.B. Asbury, E.H. Sargent, Colloidal-quantum-dot photovoltaics using atomic-ligand passivation, Nat. Mater. 10 (2011) 765–771. https://doi.org/10.1038/nmat3118.

[20] G. Ma, R. Du, Y. Cai, C. Shen, X. Gao, Y. Zhang, F. Liu, W. Shi, Solar Energy Materials and Solar Cells Improved power conversion e ffi ciency of silicon nanowire solar cells based on transition metal oxides, Sol. Energy Mater. Sol. Cells. 193 (2019) 163–168. https://doi.org/10.1016/j.solmat.2019.01.010.

[21] P.R. Brown, R.R. Lunt, N. Zhao, T.P. Osedach, D.D. Wanger, L.-Y. Chang, M.G. Bawendi, V. Bulović, Improved Current Extraction from ZnO/PbS Quantum Dot Heterojunction Photovoltaics Using a MoO 3 Interfacial Layer, Nano Lett. 11 (2011) 2955–2961. https://doi.org/10.1021/nl201472u.

[22] C.P. Chen, Y.D. Chen, S.C. Chuang, High-performance and highly durable inverted organic photovoltaics embedding solution-processable vanadium oxides as an interfacial hole-transporting layer, Adv. Mater. 23 (2011) 3859–3863. https://doi.org/10.1002/adma.201102142.

[23] D. Wang, N.K. Elumalai, M.A. Mahmud, M. Wright, M.B. Upama, K.H. Chan, C. Xu, F. Haque, G. Conibeer, A. Uddin, V2O5 -PEDOT: PSS bilayer as hole transport layer for highly efficient and stable perovskite solar cells, Org. Electron. 53 (2018) 66–73. https://doi.org/10.1016/j.orgel.2017.10.034.

Chapter 6. Conclusion

In summary, hybrid heterojunction solar cells made of Si nanostructures and PEDOT:PSS were created. The light trapping effect caused by Si nanostructures made the antireflection layer dispensable, where the cell manufacturing costs and steps were reduced. The quality of the hybrid device was improved after full coverage of the nanowires with PEDOT:PSS using CPE method.

The NRET effect was investigated using SiQDs that had been terminated with ligands. NRET effect by SiQDs terminated with ligands led to enhanced J_{SC}, providing a practical method to enhance solar cell characteristics. NRET phenomenon is a very distance-dependent phenomena, as demonstrated by the strong relationship between the NRET process and the length of the passivation ligands. Shortening the ligand length improved NRET efficiency and led to greater J_{SC}, which in turn improved energy conversion efficiency.

To address the stability issue of the hybrid device, various vanadium oxide films with various crystal structures and stoichiometries were successfully deposited on silicon substrates using a solution processing procedure followed by annealing in various atmospheres. The production of anode/VO_x/SiNWs/cathode solar cells demonstrated the VO_x layer's hole-injection role, which in turn promotes the separation and collection of photogenerated carriers owing to oxygen deficiencies, with vacuum-annealed films yielding the best results. The deposition of a 15-nm VO_x layer that is annealed under vacuum at 400°C (VO_{2-x}) can produce the best cell performance with PCE of 5.2%. The stability of the SiNWs-based solar cells using VO_x films was superior to that of the cells using PEDOT:PSS films.

To extra enhance the nanostructure's passivation by VO_x films, Ag/VO_{2-x}/n-SiNPs Schottky solar cell was made by depositing VO_{2-x} thin layer on pencil-shaped silicon nanowires substrate which exhibited PCE of 5.6%. For temperatures between 298 and 358 K, the *I-V-T* curve demonstrated excellent Ag/VO_{2-x}/n-SiNPs Schottky diode performance. Thermionic emission, space charge limited current, and space charge limited current regulated by a distribution of trap levels are the three primary transport mechanisms discovered in the forward bias regime based on the *I-V-T* measurements. Capacitance-voltage measurements provide details on the depletion layer extending in the Silicon side, with the depletion width predicted to be roughly 900 nm. By utilizing SiQDs, the efficiency of the Ag/VO_{2-x}/n-SiNPs Schottky solar cell was increased by about 6%.

The utilization of VO_x films as hole-injection layers paves the way for the creation of affordable and robust optoelectronic and electrical devices.

List of publications

1. **Abdelhameed, M.**, Jevasuwan, W., Subramani, T., Chen, J., & Fukata, N. (2021). Efficiency enhancement of Si nanostructure hybrid solar cells by optimizing non-radiative energy transfer from Si quantum dots. *Nano Energy*, *82*, 105728. https://doi.org/10.1016/j.nanoen.2020.105728

2. **Abdelhameed, M.**, Abdelbar, M. F., Esmat, M., Jevasuwan, W., & Fukata, N. (2022). Hole-injection role of solution-processed thermally treated VO_x thin films in Si nanowire-based solar cells. *Nano Energy*, *99*, 107373. https://doi.org/10.1016/j.nanoen.2022.107373

3. **Abdelhameed, M.**, Abdelbar, M. F., El Basaty, A. B., M., Jevasuwan, W., Dai, K., Shinotsuka, K., Hatta, Y. & Fukata, N. (2023). Current transport characterization and Photovoltaic Performance of Si nanopencil-based Schottky junction assisted with VO_x as a hole-injection layer. *Micro and Nanostructures, 176*, 207519. https://doi.org/10.1016/j.micrna.2023.207519

4. Abdelbar, M. F., **Abdelhameed, M.**, Esmat, M., El-Kemary, M., & Fukata, N. (2021). Energy management in hybrid organic-silicon nanostructured solar cells by downshifting using CdZnS/ZnS and CdZnSe/ZnS quantum dots. *Nano Energy*, *89*, 106470. https://doi.org/10.1016/j.nanoen.2021.106470

5. Saini, A., **Abdelhameed, M**., Rani, D., Jevasuwan, W., Fukata, N., Kumari, P., Srivastava, S.K., Pathi, P., Samanta, A. & Dutta, M. (2022). Fabrication of periodic, flexible and porous silicon microwire arrays with controlled diameter and spacing: Effects on optical properties. *Optical Materials*, *134*, p.113181. https://doi.org/10.1016/j.optmat.2022.113181Get

6. Esmat, M., Doustkhah, E., Abdelbar, M., Tahawy, R., El-Hosainy, H., **Abdelhameed, M.**, Ide, Y., & Fukata, N. (2022). Structural Conversion of Cu-Titanate into Photoactive Plasmonic Cu-TiO_2 for H_2 Generation in Visible Light. *ACS Sustainable Chemistry & Engineering* 10, 4143–4151. https://doi.org/10.1021/acssuschemeng.1c07555